7-5-2016

Magnetic Materials for Biomedical Applications

Michael E. Zilm
michael.zilm@uconn.edu

Magnetic Materials for Biomedical Applications

Michael Zilm, PhD

University of Connecticut, 2016

Magnetic materials are of interest for biomedical applications for the ability to remotely control magnetic particles through the use of non-invasive magnetic fields. Specific applications of magnetic materials in biomedical fields include magnetic resonance imaging, drug delivery, or hyperthermia-based cancer treatments. The most commonly used material for these applications are iron oxides, which suffer from acute toxicity and unknown fate in vivo and thereby limit their applications.

An alternative approach is to substitute magnetic ions into a biocompatible and biodegradable material to impart magnetic properties. Hydroxyapatite, the main inorganic component of natural bone, is widely studied as a biomaterial for its excellent biocompatibility and osteoconductivity. The crystal structure of HA is highly flexible allowing for a wide range of substitutions for tailoring material properties. Hydroxyapatite with magnetic properties may be an alternative to iron oxides for the aforementioned applications. Iron, cobalt, and manganese substituted hydroxyapatite powders were synthesized via ion exchange and characterized to verify successful substitution into the lattice. All substitutions were successfully prepared and resulted in ion-substituted hydroxyapatite with magnetic properties. Experimental results were also in good agreement with theoretical calculations which predicted manganese substituted hydroxyapatite to have the largest magnetic moment. The synthesized magnetic hydroxyapatites are shown to be biocompatible making them suitable for magnetic resonance imaging and drug delivery applications while providing a biodegradable and biocompatible alternative to iron oxides for these applications.

Magnetic materials have also been used in tumor therapy applications. For tumor therapy applications the materials blood circulation time is desired to be as long as possible to enhance accumulation at the tumor site. Semi-flexible filomicelles have been shown to have significantly longer circulation times than rigid spheres or rods. Type I collagen, the main organic phase of bone, is a filamentous protein and semiflexible polymer that allows for mineralization within specific zones of the fiber. Through self-assembly and bio-templating we have developed a method to induce mineralization of iron oxide within collagen fibers to form a flexible and magnetic "nanoworm" for tumor therapy applications.

Magnetic Materials for Biomedical Applications

Michael Zilm

B.S., University of Connecticut, 2011

A Dissertation Submitted in Partial Fulfillment of the

Requirements for the Degree of

Doctor of Philosophy

at the

University of Connecticut

2016

APPROVAL PAGE

Doctor of Philosophy Dissertation

Magnetic Materials for Biomedical Applications

Presented by

Michael Zilm, B.S.

Major Advisor _____

Mei Wei

Associate Advisor _____

Xiuling Lu

Associate Advisor _____

Menka Jain

University of Connecticut
2016

ACKNOWLEDGEMENTS

First and foremost, I would like to thank my advisor, Dr. Mei Wei, for her support and encouragement throughout my studies. Dr. Wei provided numerous collaborative and external enrichment activities for me to pursue. With Dr. Wei's support I was able to gain entrepreneurial experience and partake in Science, Technology, Engineering, and Mathematics outreach. I am also thankful to my associate advisors, Dr. Menka Jain and Dr. Xiuling Lu, for their invaluable support and suggestions.

For my experience with entrepreneurship, I would like to thank Dr. Hadi Bozorgmanesh for his invaluable experience, advice, support, teaching, and encouragement. I would alos like to thank Aida Ghiaei for all of her support during my time as a GK-12 fellow and also for providing numerous professional development opportunities.

I would like to thank everyone who has helped me conduct experiments or aid me in the use of equipment in the Institute of Materials Science: Dr. Lichun Zhang, Dr. Jack Gromek, Dr. Heng Zhang, Gary Lavigne, and Laura Pinatti. The staff in the Materials Science and Engineering department along with the Insititute of Material Science including Deborah Perko, Nancy Kellerann, Cathy McCracken, Maria Mejia, Kimberly Post, Lorri Lafontaine, and Shari Masinda for all of the support they provided.

Also, I would like to thank my collaborators for their help and valuable discussion. I would like to thank Dr. Ramamurthy Ramprasad, his postdoctoral researcher Vinit Sharma, and his student Lihua Chen for performing density functional theory calculations and discussion of these results. For magnetization measurements, I would like to thank Dr. Menka Jain and her former students Dr. Margo Staruch and Dr. Austin McDannald for

performing magnetization measurements and data interpretation. I would like to thank Dr. Xiuling Lu and her student Derek Hargrove for their discussion and preliminary *in vivo* work they have performed during my studies. I would also like to thank Dr. William Hines for his support, discussion, performing magnetization measurements, and his enthusiasm for research.

I would like to acknowledge the members of Dr. Wei's lab past and present for their discussion and aid with experiments: Dr. Zengmin Xia, Dr. Erica Kramer, Dr. Max Villa, Stephanie Bendtsen, Drew Clearfield, Jonathan Russo, Changmin Hu, Bryant Heimbach, Seamus Thomson, and Le Yu. I would like to especially thank Changmin Hu for all of my experiments where she performed transmission electron microscopy. It was a great pleasure to work with all of them.

I would like to thank all of my family, my parents, and my siblings for their unconditional love and support. My father, Dr. Kurt Zilm, I would like to thank him for all of his advice. My mother, Velma Zilm, I would like to thank her for all of her unconditional love and support. I would like to thank the members of the Scott family: Susan, Michael, and Sharon for their support.

Lastly, I would like to thank the funding agencies NSF grants (CBET-1133883 and CBET-1347130), NSF GK-12 program (0947869), and the GE fellowship for their support.

Table of Contents

List of Figures

List of Tables

CHAPTER ONE

Introduction

1.1 Magnetic Materials for Biomedical Applications

Magnetic materials have attracted significant interest as a multi-functional material for biomedical applications.[1–7] The ability to "remotely" control magnetic particles using non-invasive magnetic fields allows for targeted delivery applications where a magnetic field manipulates a magnetic particle*in situ*. This property is advantageous for magnetic resonance imaging (MRI) contrast enhancement, targeted drug delivery, cancer hyperthermia, and cell stimulation and magnetic separation applications.[1, 2, 4, 7–10]

The magnetic properties of a material dictate its application. Figure 1.1 depicts different magnetic responses to an applied magnetic field. Diamagnetic materials create an opposing magnetic field that results in a negative slope. In paramagnetic materials, magnetic moments align with an applied magnetic field resulting in a small magnetization that vanishes upon removal of the applied magnetic field. For ferri- and ferro-magnetic materials the response is characterized by a rapid increase in magnetization and eventual saturation of the magnetic moment; upon removal of the magnetic field a permanent, remanent, magnetization remains. The ideal material for biomedical applications would have zero magnetization in the absence of a magnetic field but a large magnetization in the presence of a low magnetic field.This behavior is desired because if there is a remanent magnetization, particles would aggregate due to magnetic dipole interactions. Superparamagnetic materials fit into this description, Figure 1.1 (d). While superparamagnetic materials are ideal for all aforementioned applications, paramagnetic and ferri- or ferro-magnetic materials are also suitable for certain applications. Table 1.1 outlines the suitable magnetic properties for different applications.

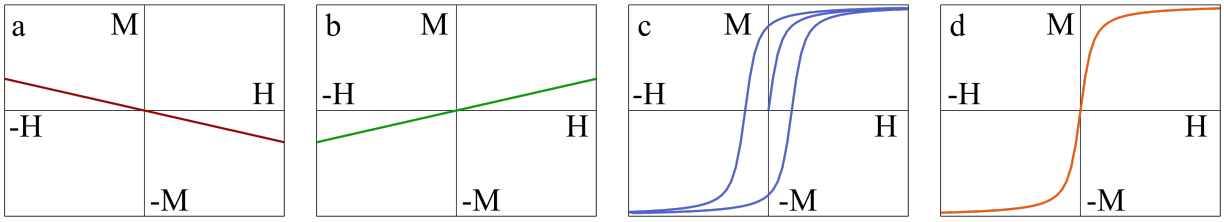

Figure 1.1: Magnetization (M) of different type of magnetic materials under an applied magnetic field (H). Diamagnetic (a), paramagnetic (b), ferromagnetic (c), and superparamagnetic (d).

Table 1.1: Summary of the magnetic properties required for different biomedical applications where magnetic properties are desired/needed.

Application	Required Magnetic Properties	
Magnetic Separation	Superparamagnetic	Ferromagnetic
Cell Stimulation	Superparamagnetic (twisting force)	Ferromagnetic (pulling force)
Targeted Drug Delivery	Superparamagnetic	
MRI Contrast Agent	Paramagnetic (T_1 imaging)	Superparamagnetic (T_2 imaging)
Hyperthermia	Superparamagnetic	

1.1.1 Magnetic Separation

Purification of proteins and cells is typically achieved through expensive liquid chromatography techniques.[11, 12]Magnetic separation provides a simple and efficient technique to isolate valuable cells or proteins in a single vial. The particles are functionalized with a targeting agent to selectively bind to the cell/protein of interest and a strong magnetic field is applied to collect magnetically labeled cells/proteins.[13, 14] This separation technique can be employed numerous times to improve purification. Magnetic particles have been used to isolate hematopoietic stem cells from peripheral blood by labeling magnetic particles with antibody CD34 to isolate CD34-positive mononuclear blood cells.[15] In clinical applications labeled magnetic particles may be added to a patients sample to aid in diagnosis of diseases. For example immuno-magnetic particles are capable of detecting one tumor cell per 10^7 peripheral blood mononuclear cells.[16] Magnetic particles must

have a large magnetization to be effective for this application, but it provides a simple, cost efficient, and highly effective tool to isolate cells/proteins in expressed in low quantities.

1.1.2 Magnetic Stimulation

Tissues are a dynamic material that respond to internal and external stimuli. Mechanical stimuli is an often studied external stimuli that is known to initiate signaling pathways and is required for production of certain proteins in bone, cartilage and muscle cells.[17] Bone for instance requires cyclic loading for proper function.[18] Mechanical stimuli causes a cellular response through the activation of mechanosensitive ion channels or the deformation and activation of the cell membrane and cytoskeleton.[9] The typical forces exerted on cells *in vivo* is on the order of 10^{-12} to 10^{-9} Newtons which is the same order of magnitude that external magnetic fields can exert on magnetic nanoparticles allowing for magnetic stimulation of cells.[18, 19]

The ability to manipulate these channels using magnetic micro- or nanoparticles allows for *in vitro* investigations of cell function and molecular signaling pathways. Magnetic manipulation is achieved by functionalizing magnetic particles to attach to specific membrane receptors and applying magnetic fields to create a translational (pulling) force or torque (twisting) directly to the cell. Through quantification of ion channel kinetics the biochemical pathways associated with these receptors can be elucidated.[18] Ion channel activation using magnetic beads was suggested that endothelial cell stiffening was mediated through Rac- or Cdr42hs-dependent pathways.[20] Magnetic actuation has also been used for cellular conditioning in the field of tissue engineering and regenerative medicine. Magnetic nanoparticles functionalized to target TREK-1 receptors in human bone mesenchymal stem cells (HBMSCs) have been shown *in vitro* to up regulate gene expression of osteopontin and Cbfa1.[21]

1.1.3 Targeted Drug Delivery

In drug delivery "a pharmaceutical compound is administered to achieve a therapeutic effect."[22] Often times, a specific area is of interest for therapy and targeting is achieved via passive or active targeting approaches. Passive delivery relies on diffusion and convection to deliver the therapeutic agent, while targeted approaches utilize targeting ligands to increase retention of the therapeutic agent at the target site.[23] Neither of these approaches provide site-directed targeting to the area of interest. Magnetic delivery systems offer 'remote' control over the delivery vehicle, where an external magnetic field is applied to guide the magnetic delivery vehicle to the site of interest. Figure 1.2 depicts the concept of magnetic delivery.

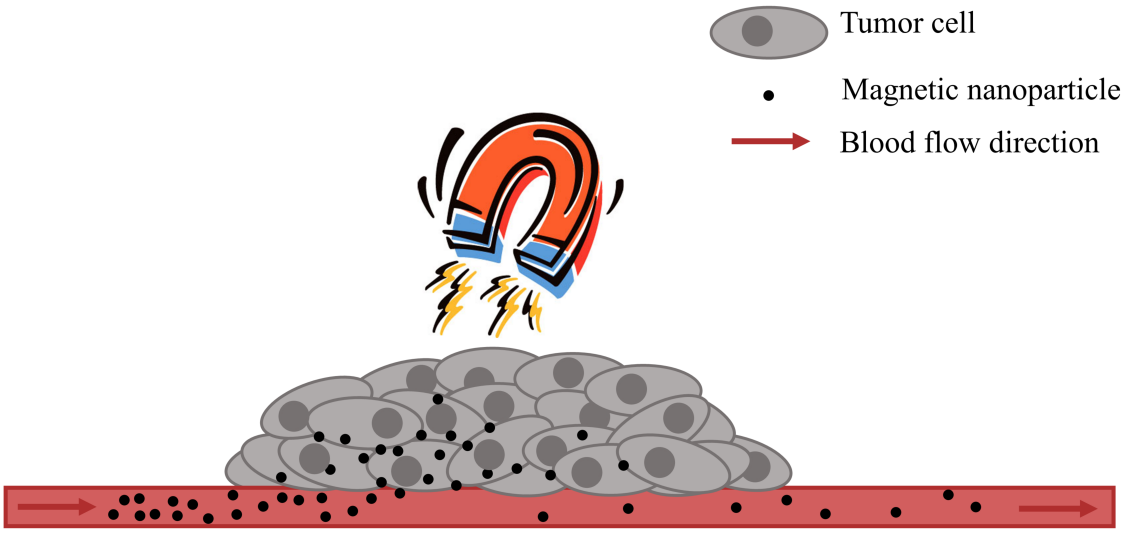

Figure 1.2: The concept of magnetic delivery where an externally applied magnetic field is used to guide magnetic particles to the site of interest.

In magnetic delivery systems, magnetic particles are surface functionalized to impart colloidal stability, allow attachment of therapeutic agents to the magnetic particle, and allow detachment under an applied stimuli. After administration of the magnetic delivery

system external magnetic fields are applied with high gradients to accumulate the magnetic particles at a specific site; subsequently the drug is released.[24, 25] This approach is often applied for tumor therapy where conditions associated with the tumor microenvironment are used induce drug release such as pH and enzymatic degradation.[24] Heat generated through the application of an alternating magnetic field may also be applied for drug release when thermosensitive polymers are employed for surface functionalization.[25]

Magnetic targeting has been shown to be successful in laboratory experiments and preclinical practice.[26–29] Schleich *et al.* compared the passive, active, magnetic, and combination of magnetic and active targeting ability of superparamagnetic iron oxide nanoparticles for tumor therapy.[27] The combination of magnetic and active delivery resulted in the largest accumulation of iron oxide in the tumor followed by magnetic, active, and passive targeting respectively.[27] Magnetic targeting was shown superior to passive targeting, when magnetic targeting was used to accumulate polyethylene glycol modified cross-linked starch coated iron oxide nanoparticles for brain tumors.[28] Magnetic targeting is a promising approach but requires high magnetic field gradients to overcome convective drag forces. Alexiou *et al.* used a 1.7 Tesla magnetic field in the region of a tumor surface to successfully treat squamous cell carcinoma in rabbits.[29] The effectiveness of magnetic targeting is largely dictated by the strength of the magnetic field gradient and the volumetric and magnetic properties of the particles.

1.1.4 MRI Contrast Agents

MRI is a widely used clinical tool for the assesment/diagnosis of soft tissue and tumors. Imaging is achieved by monitoring the relaxation time of nuclear magnetic spins of protons in water, in particular, and contrast is achieved as result of the different relaxation times between different types of tissue. Imaging is performed utilizing T_1 or T_2 relaxation. In T_1 weighted images, differences in longitudinal relaxation (the time for spins to realign with the magnetic field) of tissues are used to provide contrast, and T_2 weighted images

differences in transverse relaxtion (the time for spins to dephase) are utilized for contrast. But, the differences in relaxation times between tissues are often small making diagnosis difficult at times.[30]

Contrast can be enhanced through the use of a contrast agent. Most commonly paramagnetic complexes, such as gadolinuium (3+) or manganese (2+) chelates, are used to enhance T_1 relaxation, and superparamagnetic iron oxide nanoparticles are used to enhance T_2 relaxation.[31] T_1 contrast agents result in an increase in brightness, while T_2 contrast agents decrease brightness.

Current T_1 contrast agents are limited because of the small size of Gd^{3+} and Mn^{2+} chelates to the detection of the breakage of the blood brain barrier, changes in vascularty, flow dynamics, and changes in perfusion.[32] While the resulting dark signal from T_2-weighted images can make diagnosis difficult, because the signal make be confused with artifacts such as bleeding or hard tissue.[32]

The ideal contrast agent would provide both T_1 and T_2 contrast enhancement where both imaging modalities can be used in conjunction for more accurate diagnosis. Current strategies for imparting T_1 and T_2 enhancement involve: synthesis of ultra-small metal oxide nanoparticles or the combination of a T_1 and T_2 contrast agent in a single system.[33–37] Wang *et al.* synthesized a pH responsive nanogel containing manganese oxide and iron oxide nanparticles. Under an acidic condition, the dissolution of manganese oxide results in the release of manganese ions results in positive T_1 contrast enhancement, while the iron oxide nanoparticles provide positiveT_2 contrast enhancement.[33] While Wang *et al.* achieved a dual responsive T_1 and T_2 contrast agent by reducing the size of iron oxide nanoparticles to less than 2 nm.[34] The small size of the nanoparticles resulted in a large surface that increases the number of interactions between water molecules and surface iron ions which decreased T_1.[34] Susceptibility effects from iron oxide result in local magnetic field inhomogeneity which decreases T_2.[34]

1.1.5 Hyperthermia

Hyperthermia is a cancer treatment where elevated temperatures are used to kill malignant cells. In a typical treatment, heat is generated by applying a specific absorption rate (SAR (W/kg)) to the tumor via, microwaves, radiofrequency, ultrasound, or alternating magnetic fields to increase and maintain the temperature in the tissue around 41-42 °C.[38] This temperature range has been successful in killing malignant cells, because malignant cells are more temperature sensitive than normal cells where irreversible damage does not occur until 45 °C.[39] Spatiotemporal temperature control is essential for effective hyperthermia treatment and is difficult to achieve with microwaves, radiofrequency and ultrasound. [38] Magnetic hyperthermia has been promising, since it utilizes dispersed magnetic particles allowing the specific tissue of interested to be targeted and heated.[38]

Superparamagnetic iron oxide nanoparticles are often used for hyperthermia treatments. Heat is generated through either Néel's or Brownian relaxation mechanisms under the application of an alternating magnetic field with a frequency of a few hundred kHz and amplitude of a few kA/m. The rate at which heat is generated (SAR) can be controlled through modulation of the physical and chemical properties of the magnetic material.[40–42] The heat generating characteristics can be used in conjunction with other magnetic biomedical applications such as targeted drug delivery for more effective treatments.[43] For this effect, hyperthermia has been used to increase the effects of chemotherapy treatments. The temperature elevation aids in increasing the permeability of the tissue, which is advantageous for increased extravasation of nanoparticles into the tumor resulting in more efficient delivery of chemotherapeutics.[44, 45]

1.1.6 Current Issues with Magnetic Particles

The most widely used magnetic materials for biomedical applications are γ-Fe_2O_3 and Fe_3O_4. The high magnetization, ease of synthesis, and the high dietary need of iron has made these materials lucrative for biomedical applications. For clinical applications

where long circulation times are needed these materials are surface functionalized with ampiphilic or charged moieties to prevent protein adsorption. After functionalization these materials are considered well tolerated because rapid clearance through extravasation, renal clearance, and mechanical filtration removes the majority of nanoparticles within 24 hours.[46] But poor biodegradation and acute toxicity of iron oxides have raised concerns over the application of iron oxides in medical applications.[47]

Uncoated iron oxide nanoparticles are non-degradable, cytotoxic, and are believed to support the formation of reactive oxygen species (ROS), which have damaging effects on cells.[48] Removal of iron oxide is accomplished by internalization by cells to degrade the particles under acidic conditions to free iron ions.[49] This can lead to an excess of iron in the organs and result in iron overload or the formation of damaging ROS species. *In vitro* studies have shown iron oxide nanoparticles functionalized with negatively and positively charged functional groups are less toxic than uncoated nanoparticles, but still cytotoxic.[50] While moderate levels of Fe_2O_3 nanoparticles have been shown to adversely affect neuron function *in vitro* and displayed a dose dependent reduction on cell viability.[51] In other non-immunogenic cells iron oxides have shown to have dose dependent toxicity that adversely affects mitochondrial function, membrane leakage of lactate dehydrogenase, and result in genotoxicity and chromosome condensation.[48, 52]

There also concerns over short and long term *in vivo* toxicity where nanoparticles distribute into various essential organs. Some clinically available iron oxide nanoparticles coated with dextran are prone to the dextran detaching during circulation.[52] Uncoated particles are prone to aggregation which can block blood flow and result in embolism.[53, 54] The distribution of particles *in vivo* have shown particles to accumulate in other organs such as the brain where the long term effect of these particles are uncertain.[49] The development of an inherently biodegradable and biocompatible magnetic particle may minimize short and long term toxicity concerns with functionalized iron oxide nanoparticles.

1.2 Hydroxyapatite

To circumvent the issue of biodegradation and acute toxicity, biocompatible materials may be doped with magnetic ions to impart magnetic properties. An ideal material is hydroxyapatite (HA) ($Ca_{10}(PO_4)_6(OH)_2$) the mineral phase of bone and a well-documented biomaterial known for its excellent biocompatibility. Synthetic HA is widely used in biomedical applications such as a filler for bone replacement, drug delivery, tissue engineering scaffolds, and as a bioactive coating.[55, 56]

1.2.1 Hydroxyapatite Substitutions

The crystal structure (space group $P6_{3/m}$) of HA is highly flexible accommodating a wide range of ionic substitutions. The materials and biological properties of HA can be altered through substitutions of Sr, Mg, K, Ba, Cu, or Fe for Ca and CO_3^{2-}, Cl, or F for OH.[57–59] Another property, which may be altered, is the magnetic properties. HA is diamagnetic in nature but recently it has been shown that substituting magnetic impurities into HA results in paramagnetism or superparamagnetism.[60–63]

1.2.2 Magnetic Substitutions

The most commonly used metal for imparting HA with magnetic properties is iron.[60, 63–65] The choice of iron as a dopant stems from its high daily dietary need and its large magnetic moment. Many more elements have the potential to yield magnetic HA with varying levels of bioactivity and magnetization. When considering potential magnetic impurities, the magnetic moment of the ion must also be considered. Ideally ions that have the largest moment, are biocompatible, and have a high solubility in the HA lattice should be used for substitution.

The magnetic moment of an element is related to the number of unpaired electrons and orbital contributions to the magnetic moment depending upon the oxidation state. The

magnetic moment of an ion can be calculated by:

$$\mu_{S+L} = \sqrt{4S(S+1) + L(L+1)}\mu_B \tag{1}$$

where S is the spin quantum number, L is the angular quantum number, and μ_B is Bohr magneton. In the case where spin-orbit coupling (Russel-Saunders coupling), which adequately describes lanthanides, is present the moment is calculated by:

$$\mu = g_J\sqrt{J(J+1)}\mu_B, g_J = \frac{3}{2} + \frac{S(S+1) - L(L+1)}{2J(J+1)} \tag{2}$$

where J is the total angular momentum, L $\pm$ S, and g_J is the Landé g-factor.

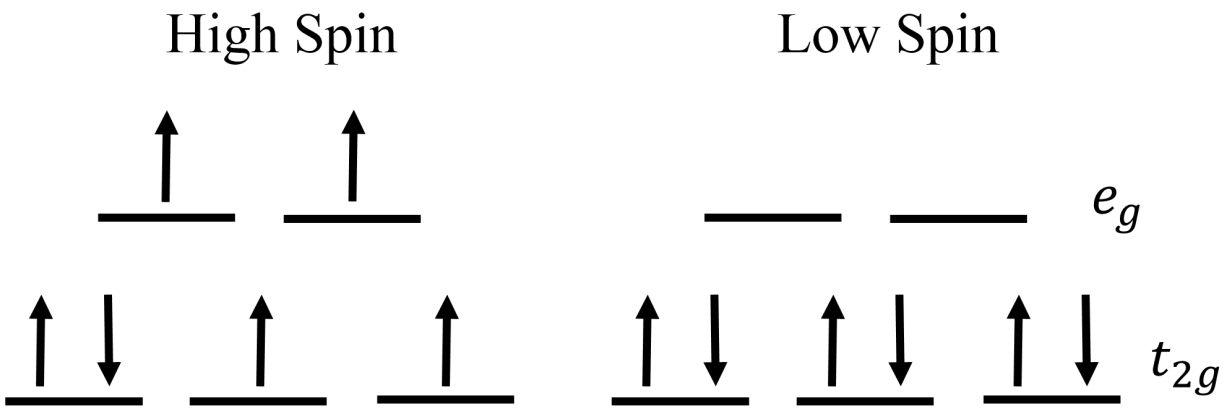

Figure 1.3: High spin (right) and low spin (left) electron configurations for Fe^{2+} or for ions with [Ar]$3d^6$ electron configurations

The local chemical environment can also affect the net moment depending upon how the crystal field splits the d-orbitals, while f-electrons are too far inside to be affected by the crystal field. When the crystal field splitting energy is small or comparable to the spin pairing energy, the electrons fill the orbitals to maximize the number of unpaired spins (high spin), but when the crystal field splitting energy is larger than the spin pairing energy, electrons fill the lowest energy orbitals first (low spin). For example Fe^{2+} in an octahedral crystal field can exhibit high spin or low spin depending upon the energy of the crystal field

Table 1.2: Maximum calculated and observed magnetic moments of transition metal ions in an octahedral environment

Ions			Electron Config.	Calculated Moment (μ_B)	Observed Moment(μ_B)		
Ti^{3+}		V^{4+}	[Ar]$3d^1$	1.73	1.6-1.7		1.7-1.8
V^{3+}		Cr^{4+}	[Ar]$3d^2$	2.83	2.7-2.9		2.8
V^{2+}	Cr^{3+}	Mn^{4+}	[Ar]$3d^3$	3.88	3.8-3.9	3.7-3.9	3.8-4.0
Cr^{2+}		Mn^{3+}	[Ar]$3d^4$	4.90	4.7-4.9		4.6-5.0
Mn^{2+}		Fe^{3+}	[Ar]$3d^5$	5.92	1.6-1.7		1.7-1.8
	Fe^{2+}		[Ar]$3d^6$	4.90		5.1-5.7	
	Co^{2+}		[Ar]$3d^6$	3.87		4.3-5.2	
	Ni^{2+}		[Ar]$3d^6$	2.83		2.9-3.3	
	Cu^{2+}		[Ar]$3d^6$	1.73		1.7-2.2	

splitting, the electron configuration is depicted in Figure 1.3.

Considering the geometry of the calcium sites in HA, which are distorted octahedral [66] any orbital contribution to the magnetic moment is most likely quenched, and the contribution to the magnetic properties can be attributed to spin only moments, which can be calculated by:

$$\mu_S = \sqrt{4S(S+1)}\mu_B \tag{3}$$

Table 1.2 lists the maximum (high spin) calculated magnetic moments of various transition metal ions, and Table 1.3 lists the maximum calculated magnetic moments of trivalent lanthanide ions that are possible substituents.

The ions with the highest magnetic moments are from the lanthanides with electron configurations from [Xe]$4f^7$ to [Xe]$4f^{12}$ whose moments range from 7.56 to 10.65 μ_B. Dy^{3+} has the highest calculated moment at 10.65 μ_B followed by Ho^{3+} with 10.6 μ_B. Despite these promising magnetic moments, many of the lanthanides are toxic in free ion form.[67, 68] Gd^{3+} with a calculated moment of 7.94 μ_B is widely used as a T_1 MRI contrast agent, but is used in a chelated form to prevent toxicity with Gd^{3+} leaching being a concern.[69] Due

Table 1.3: Maximum calculated and observed magnetic moments of trivalent lanthanides

Ion	Electron Config.	Calculated Moment (μ_B)	Observed Moment (μ_B)
La^{3+}	[Xe]$4f^0$	0	0
Ce^{3+}	[Xe]$4f^1$	2.54	2.3-2.5
Pr^{3+}	[Xe]$4f^2$	3.58	3.4-3.6
Nd^{3+}	[Xe]$4f^3$	3.62	3.5-3.6
Pm^{3+}	[Xe]$4f^4$	2.68	–
Sm^{3+}	[Xe]$4f^5$	0.85	1.4-1.7
Eu^{3+}	[Xe]$4f^6$	0	3.3-3.5
Gd^{3+}	[Xe]$4f^7$	7.94	7.9-8.0
Tb^{3+}	[Xe]$4f^8$	9.72	9.5-9.8
Dy^{3+}	[Xe]$4f^9$	10.65	10.4-10.6
Ho^{3+}	[Xe]$4f^{10}$	10.6	10.4-10.7
Er^{3+}	[Xe]$4f^{11}$	9.58	9.4-9.6
Tm^{3+}	[Xe]$4f^{12}$	7.56	7.1-7.6
Yb^{3+}	[Xe]$4f^{13}$	4.54	4.3-4.9
Lu^{3+}	[Xe]$4f^{14}$	0	0

to the toxicity of these elements, the lanthanides were not considered as substituents for magnetic HA.

Since many transition metals are required for normal biological function, the transition metal with electron configurations with [Ar]d^3 through [Ar]d^7 give rise to maximum calculated magnetic moments ranging from 3.88 to 5.92 μ_B. Of these ions, Mn^{2+}, Fe^{3+}, Fe^{2+}, and Co^{2+} were selected as possible substituents for magnetic HA. Magnetic HA is a potential alternative to iron oxide in applications related to MRI contrast enhancement and drug delivery applications as well as a material for bone repair and regeneration applications.

1.3 Requirements for Tumor Therapy

In regards to tumor therapy applications, the particle properties such as size and shape are important factors.[70–73] In both passive and targeted delivery applications the blood circulation time is an important factor in particular accumulation at the tumor site. There

is increasing evidence that non-spherical/anisotropic particles are less readily taken up by macrophages prolonging circulation.[72, 73] Non-spherical shapes also demonstrate improved targeting efficiency, since the oblong shapes can form more binding events compared to spherical particles.[73] While in circulation, non-spherical particles exhibit more lateral drift compared to spherical particles which follow streamlines which results in an increased likely hood of accumulating at the tumor site.[73] Also, particles of discoidal shape have been shown to have less accumulation in the liver than spherical particles.[74]

Mullner *et al.* studied the influence of size, shape, and rigidity on the circulation time and bio-distribution of cylindrical polymer brushes (CPBs).[75] As the length of CPBs increases the CPBs plasma residence time decreased, but $t_{1/2}$ of 20 hrs was still observed for the longest CPBs which were $\sim 1.2\ \mu$m.[75] With an increase in length more CPBs were deposited in mononuclear phagocytic system (MPS).[75] Interestingly, when the stiffness of the CPBs were increased the clearance rate increased and more material was cleared by the liver when compared to flexible CPBs of the same length.[75]

Recently the stiffness of the delivery vehicle was shown to influence blood circulation time. Discher's group showed that long semi-flexible filomicelles displayed excellent tumor targeting ability and blood circulation times as a result of the flexible and fragment-able nature of the filomicelles.[76–78] The *in vivo* performance of peglyated spherical micelles was compared to semi-flexible filomicelles. In a rodent model persistent circulation of semi-flexible filomicelles was observed for more than 7 days compared to spherical micelles which were cleared in 3 days.[76] During this time period greater accumulation of filomicelles was observed in the tumor compared to spherical micelles administered at the same concentration.[76] The enhanced performance was attributed to the semi-flexible nature of the filomicelles where upon penetration into a tumor the filomicelle may fragment as a result of shear forces. The fragmentation process kept hydrolysable filomicelles with a length of 8 μm and width of 60 nm in circulation for up to 8 days.[76] Due to size, shape, and enhanced circulation filomicelles were more efficient at the delivery of an anti-cancer drug, taxol,

allowing for a larger maximum tolerable dose. Compared to spherical micelles, filomicelles were shown to incorporate twice as much anti-cancer drug, taxol. Theoretical calculations were also performed on the interaction between taxol and filomicelles/spherical micelles, suggesting that filomicelles are able to retain more taxol due to their shape.[77] These physiochemical properties of semi-flexible filomicelles also resulted filomicelles having a twice the maximum tolerated dose of taxol that of spherical micelles.[78] Apotosis in non-tumor organs was 13-15 % less when filomicelles were administered compared to micelles.[78] These observed effects were attributed to the large size, long circulation, and fragmentation of filomicelles. Under shear flow the filomicelles may fragment into a size large enough to avoid clearance by the MPS organs but small enough to extravasate into the tumor. This behavior helps reduce apoptosis in vital organs ultimately increasing the maximum tolerated dose.[78] Overall the work conducted by the Dishcer group [76–78] highlights the importance of size, shape, and stiffness on the *in vivo* performance of delivery vehicles for cancer therapy.

Magnetic nanoworms, which are a linear chain of iron oxide spheres, have been synthesized through the precipitation of magnetite in the presence of dextran with a length of $\sim$ 50 nm and width of $\sim$ 5 nm.[79] Park *et al.* hypothesized that the anisotropic structure would result in improved circulation and ability of the nanoworms to target and image tumors.[79] The *in vivo* evaluation demonstrated that these nanoworms had similar blood circulation times to iron oxide nanospheres, $t_{1/2}$ of 17 hours for nanoworms compared to $t_{1/2}$ of 18 hours for nanospheres. Retention of nanoworms within the tumor was observed at 48 hours post administration whereas a high percentage of nanospheres have been cleared from the tumor at 48 hours. The retention behavior was attributed to the larger size of the nanoworms which increases the difficulty to extravasate out of the tumor.[79] The shape of these nanoworms improved tumor targeting ability. Through optimizing a conjugated targeting ligand to the nanoworms improved uptake and increase the targeting efficiency were observed.[80] Nanoworms conjugated with the targeting ligand had twice the tumor

uptake of nanospheres with the targeting ligand.[80] The magnetic property of iron oxide also render the materials suitable for magnetic resonance imaging (MRI) applications. Wang *et al.* synthesized magnetic nanoworms using the method by Park *et al.*[79] with a length of $\sim$ 250 nm and width of $\sim$ 7 nm and assessed the magnetic nanoworms as a MRI contrast agent.[81] Compared to a commercially available spherical iron oxide based MRI contrast agent nanoworms displayed an excellent transverse relaxivity R_2 of 455 $mM^{-1}s^{-1}$ compared to 100 $mM^{-1}s^{-1}$ for feridex.[81]

The main organic component of bone is type I collagen which is a long and flexible filamentous protein. The polymerization of collagen monomers into collagen fibers results in regions of overlap and gaps within the fiber. Within the field of biomineralization it has been demonstrated that HA can be selectively deposited in the gap zone of collagen fibers.[82–84] Inspired by this structure, the deposition of an inorganic magnetic phase within the gap zone of collagen fibers may yield a semi-flexible and magnetic material that can be used for tumor targeting applications. The combination of these materials allows for a potential magnetic material with long blood circulation time that may be used for the detection and treatment of tumors through MRI, targeted drug delivery, and cancer hyperthermia.

1.4 Objectives

The objective of the research here is to (a) predict potential transition metal substituents for magnetic HA that would yield the largest magnetic moment, (b) synthesis and characterization of different magnetic HA in particular manganese-, iron-, and cobalt-substiuted HA, (c) *in vitro* assessment of magnetic HA, and (d) develop a method to mineralize collagen fibers with iron oxide for the synthesis of magnetic nanoworms for tumor therapy applications. For objective (a) HA was chosen for substitution with transition metals to impart magnetic properties due to the well-known biocompatibility of HA along with its ability to accept a wide range of substituents.

Initially, theoretical calculations were performed to aid in the selection of substituents and confirm successful substitution with experimental data. From the theoretical calculations the following divalent transition metals: manganese, iron, and cobalt were selected as substituents. Substituted HA was synthesized by performing an ion-exchange with pure HA. All substitutions resulted in paramagnetic properties with no detection of a second phase. Many transition metals have multiple stable oxidation states, as such trivalent iron and pentavalent manganese. Iron substituted HA was further synthesized using Fe^{3+} and a combination of Fe^{2+} and Fe^{3+}. Fe^{3+}HA displayed paramagnetic properties, while Fe^{2+3+}HA displayed a combination of magnetic responses of Fe^{2+}HA and Fe^{3+}HA. Manganese has been reported to positively influence *in vitro* activity in particular by promoting cell attachment and may be well suited as a bioactive bone substitute material. The sintering behavior and mechanical properties of MnHA were compared to that of pure HA to assess MnHA for other bone tissue engineering applications. Since the synthesized transition metal substituted HA's are intended for biomedical applications, *in vitro* evaluation was performed to assess the biocompatibility of the different substituted HA powders. All substituted apatites were biocompatible with iron and manganese not significantly effecting cell behavior.

The magnetic properties of the synthesized magnetic HA are well suited for MRI contrast and targeted delivery applications, but the rigid nature of the magnetic HA may result in poor circulation times and may not be well suited for tumor therapy applications. A semi-flexible and magnetic materials was developed based on the mineralization of type I collagen with iron oxide. Type I collagen was templated with poly-aspartic acid to promote the deposition of iron oxide into the gap zone of collagen fibers. Transmission electron micrographs showed the deposition of iron oxide in collagen fibers. The composite material is a nanoworm for potential tumor therapy applications.

CHAPTER TWO

Hydroxyapate Substituted by Transition Metals: Experiment and Theory

2.1 Introduction

Hydroxyapatite (HA) is a commonly used bone grafting material and is a well-documented biomaterial known for its osteoconductivity.[55, 85] The main mineral phase of bone is HA, $Ca_{10}(PO_4)_6(OH)_2$, and its bioactivity can be modified through substitutions of other anions, cations, or functional groups. Well studied and commonly found trace elements in bone are Mg^{2+}, Sr^{2+}, CO_3^{2-}, and SiO_4^{4-}; these elements have been shown to render HA more bioactive compared to stoichiometric HA.[86–89] The hexagonal crystal structure of HA allows for a wide variety of substitutions that can alter bioactivity but also physical properties as well.[90] Other possible substituents which are less studied are transition metals of the 3d block which are necessary for normal biological function.[91, 92]

One unique characteristic of some transition metals is their magnetic response, one that can be modified and tuned in HA, which is diamagnetic, via substitutions. Thus, through substituting with magnetic ions HA with magnetic properties can be achieved resulting in a biocompatible and magnetic biomaterial. There is a wide range of biomedical applications for biocompatible and magnetic materials such as drug delivery, cell separation, magnetic resonance imaging, and hyperthermia applications.[31, 93–95] Iron oxide nanoparticles are currently used for these applications but there have been concerns over acute toxicity.[47] Since HA is biocompatible and biodegradable, application of magnetic HA will mitigate these concerns.

The most commonly used metal for imparting HA with magnetic properties is iron.[60, 63–65] The choice of iron as a dopant stems from its high daily dietary need and its large

magnetic moment. Other transition metals possess the potential and have rendered HA magnetic, such as cobalt [96], but concerns over toxicity has limited the research despite the fact that cobalt is required in trace amounts for vitamin B12 function.[97] Another suitable transition metal that has received little attention is manganese, which has been shown to influence bone remodeling and is used as a supplement to retard bone loss.[98, 99] However, initial studies have reported that manganese substitution does not affect the magnetic properties of HA.[62] Many elements have the potential to yield magnetic HA with varying levels of bioactivity and magnetization.

The time to synthesize and characterize all possible magnetic HAs is laborious and time consuming. The use of density functional theory (DFT) calculations to identify promising new materials helps to guide and expedite experimental work. Computational efforts coupled with experimental work has provided information on site preference, structural modifications, and possible mechanisms of substitution in Pb, Cd, Sr, Mg, Zn, Ti, Si, CO_3^{2-}, and F.[66, 100–109] In Si substituted HA, DFT has been used to study defect chemistry with results suggesting two different charge compensation mechanisms (1) the formation of $HSiO_4$ groups under hydrating conditions and (2) under dehydration the formation of OH vacancies, again DFT results coincided well with experimental data.[106, 107] Material property changes have been successfully predicted with DFT in calcium deficient hydroxyapatite where Bhat *et al.* calculated a decrease of 30 % in elastic properties due to calcium vacancies which coincided with observed experimental results.[110] Minor differences in optical properties have also been calculated for the $Ca_{10}(PO_4)_6X_2$ system where X is OH, F, Cl, or Br has been calculated with DFT and only minor differences in optical properties were calculated.[111] Theoretical work on magnetic HA systems have focused on the calculation of magnetic spectroscopic parameters for electron paramagnetic resonance (EPR) and Mössbauer spectras.[112–115] Jiang *et al.* used DFT to analyze electronic structure and compute magnetic spectroscopic parameters for electron paramagnetic resonance (EPR) and Mössbauer spectras of Fe^{2+} and Fe^{3+} substituted HA.[112] The

comparison of experimental spectrums with computed spectroscopic parameters allowed for the assignment of site occupancy of Fe^{2+} and Fe^{3+} in the HA crystal lattice.[112] While EPR studies combined with DFT calculations have also helped understand interactions between nitrate and Mn^{2+}ions and nitrate and carbonate ions in the HA lattice where the nitrate ions are the paramagnetic center of interest.[113–115]

Little theoretical work has been done on the magnetic properties of HA substituted by divalent transition metals (MHA). Using DFT, we determined the most promising transition metals that would yield the highest magnetic moment, followed by synthesis of the substituted HAs. Herein we investigate the substitution of divalent transition metal ions: Mn^{2+}, Fe^{2+}, and Co^{2+} in HA from both theoretical and experimental approaches.

2.2 Materials and Methods

2.2.1 Materials

Ammonium phosphate dibasic (99+%), iron chloride tetrahydrate (99+%), cobalt chloride hexahydrate (analysis grade), sulfuric acid (95-98%), and potassium bromide (IR grade) were purchased from Acros Organics. Calcium nitrate (99+%), manganese chloride tetrahydrate (99+%), lanthanum chloride heptahydrate (99+%), nitric acid (69.2%), and ammonium hydroxide (29.45%) were purchased from Fisher Scientific.

2.2.2 HA and MHA synthesis

HA was synthesized via a wet chemical method. An aqueous solution of ammonium phosphate dibasic (80 mM) was added drop-wise to an aqueous calcium nitrate solution (225 mM) at room temperature with the calcium to phosphate ratio maintained at 1.667. Ammonium hydroxide was used to raise the pH of both solutions above 11 prior to mixing the two solutions. Once the two solutions were completely mixed, the temperature was raised to 95 °C and maintained at the temperature for five hours. Then the solution was

cooled to room temperature and aged for two days under constant stirring. The precipitates were collected via centrifugation and washed 3 times with de-ionized, 2 times with ethanol and vacuum dried.

MHA samples were fabricated through an ion-exchange procedure. A salt solution of the desired transition metal ($MnCl_2$, $FeCl_2$, or $CoCl_2$) was prepared at a concentration of 0.02 M, and the pH of the solution was adjusted to 2.7 with dilute sulfuric acid. Previously synthesized HA was immersed in the ion-exchange solution at 0.5 g/dL and sonicated for one hour at room temperature with intermittent stirring. The ion-exchanged HA was collected by centrifugation, washed 3 times with DIW, and vacuum dried.

2.2.3 Characterization

Chemical analysis of the calcium and transition metal was determined by atomic absorption spectroscopy (Perkin Elmer Atomic Adsorption Spectrometer 3100). In brief, 15 mg of MHA powder was dissolved in 200 μL of concentrated nitric acid (15.9 M). A 2 M nitric acid solution with 5% (w/v) lanthanum chloride was then used to raise the total volume to 1 mL. The total volume was diluted to 20 mL with 0.1 M nitric acid and dilutions of the solution were used for chemical analysis.

FTIR spectra were acquired on a Nicolet Magna 560 FTIR spectrometer. Specimens were prepared using the potassium bromide method. In brief, powder samples were diluted to one part per million in KBr, grinded into a fine powder and then pressed into a transparent pellet. The FTIR spectra were acquired over the range of 4000-400 cm^{-1} with a resolution of 4 cm^{-1} and a total of 32 scans.

Powder x-ray diffraction (XRD) patterns were acquired with a Bruker D2 phaser X-ray diffractometer operating at 30 kV and 10 mA using Cu K_α radiation. Diffraction patterns were collected over 2θ between 10-120° with a step size of 0.01° and a scan rate of 4s per step. Powder patterns were refined using the Rietveld method with the general structural analysis system (GSAS) and the EXPGUI interface.[116, 117]

In order to assess the surface composition and oxidation state of the transition metal dopant, X-ray photoelectron spectroscopy (XPS) was employed using a VG X-ray Photoelectron Spectrometer with an Al K_α radiation source. High resolution XPS spectrums were acquired of the transition metal 2p and O 1s peaks using a pass energy of 50 eV and a step size of 0.1 eV. Spectrums were calibrated by setting the adventitious carbon peak to 284.7 eV, and CasaXPS was used to deconvolute the spectra.

Magnetic measurements were performed using a vibrating sample magnetometer (VSM) attached to the evercool physical property measurement system (from Quantum Design). Magnetization measurements were carried out at room temperature and with applied DC magnetic fields of up to 1 tesla.

2.2.4 Theoretical Calculations

Our DFT calculations were performed with the Vienna ab initio simulation package (VASP), [118] using the Perdew-Burke-Ernzerhof (PBE) [119] generalized gradient approximation (GGA) and a plane wave energy cutoff of 750 eV. Dense Monkhorst-Pack k-point meshes [120] of 2 x 2 x 2 were used for sampling the Brillouin zone of HA. All atoms were allowed to relax to their equilibrium positions until atomic forces are smaller than 0.01 eV / Å.

2.3 Hydroxyapatite Crystal Structure

HA occurs in a hexagonal crystal structure (space group $P6_{3/m}$) with 44 atoms per unit cell and lattice parameters $a = b \neq c$ and $\alpha = \beta = 90^\circ$, $\gamma = 120^\circ$. The unit cell and the local environment of Ca in pure HA is depicted in Figure 2.1. There are two distinct Ca sites where cation exchange may occur. The Ca(1) site is surrounded by nine oxygen ions from the surrounding phosphate tetrahedron and forms a distinct Ca channel parallel to the c-axis. The Ca(2) site is surrounded by six oxygen ions from five phosphate groups and the hydroxyl ion. The Ca(2) ions form triangular bases staggered by 60° above and below the

OH ion. The OH ion similar to Ca(1) forms a distinct channel parallel to the c-axis. Based on the distance and the coordination number of oxygen and calcium, three oxygen atoms are defined as O(1), O(2) and O(3). The oxygen in OH^- is defined as O_H. Thus the formula for HA can also be written as $Ca(I)_4Ca(II)_6(PO(1)O(2)O(3)_2)_6(O_HH)_2$.

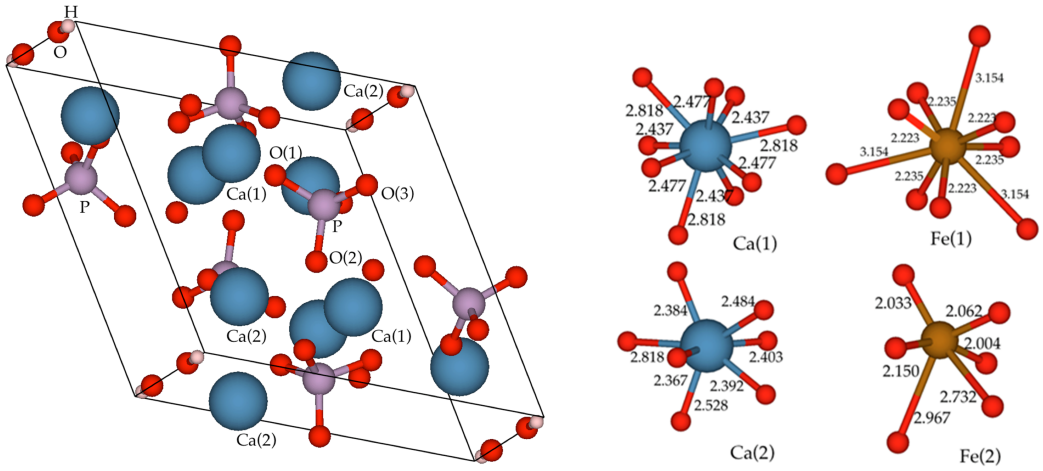

Figure 2.1: On the left is the unit cell of hydroxyapatite from the calculated atomic positions. To the right of the unit cell is distribution of the local environment of Ca in pure HA and Fe in FeHA. Bond distances are in Å.

The theoretical lattice constants from DFT calculation are a = b = 9.55 Å and c = 6.94 Å, which are in good agreement with the previously reported experimental values of HA: a = b = 9.43 Å, and c = 6.88 Å.[121] We also compare atomic positions and relaxed bond lengths in the unit cell with experimental and past DFT results for undoped HA in Table 2.1 and Table 2.2. Our results are very close to the experimental data.[122] Based on Figure 2.1, we note that there are six nearest neighboring oxygen atoms and three second nearest adjacent oxygen atoms for Ca(1), while Ca(2) has six nearest neighboring oxygen atoms and only one second nearest adjacent oxygen atom.

2.4 Results and Discussion

The phase purity of the as-synthesized HA and MHA was evaluated using X-ray diffraction. Powder diffraction patterns of these samples are depicted in Figure 2.2 along with

Table 2.1: Calculated atomic fractional coordinates of HA compared to literature values

Atom	This Work			Other DFT[a]			Exp[b]		
	x	y	z	x	y	z	x	y	z
Ca(1)	0.333	0.667	0.004	0.333	0.667	0.003	0.333	0.667	0.001
Ca(2)	0.251	0.999	0.256	0.251	1	0.25	0.246	0.993	0.25
P	0.399	0.369	0.248	0.400	0.369	0.252	0.400	0.369	0.25
O(1)	0.332	0.486	0.251	0.333	0.487	0.253	0.329	0.484	0.25
O(2)	0.588	0.464	0.245	0.588	0.463	0.247	0.589	0.466	0.25
O(3)	0.34	0.257	0.068	0.338	0.256	0.073	0.348	0.259	0.073
OH	0	0	0.246	0	0	0.285	0	0	0.25

[a]Ref[123], [b]Ref[121]

Table 2.2: Calculated bond lengths (Å) and bond angles (°) for HA compared to literature values

	This Work	Other DFT[a]	Exp[b]
Bond length			
P-O(1)	1.550	1.541	1.533
P-O(2)	1.563	1.554	1.544
P-O(3)	1.551	1.545	1.514
Ca(1)-O(1)	2.437	2.425	2.416
Ca(1)-O(2)	2.477	2.469	2.449
Ca(1)-O(3)	2.817	2.827	2.802
Ca(2)-O(1)	2.818	2.798	2.712
Ca(2)-O(2)	2.366	2.357	2.356
Ca(2)-O(3)	2.391	2.367	2.367
Bond angles			
O(1)-P-O(2)	111		
O(1)-P-O(3)	11.8		
O(3)-P-O(2)	107.9		
O(1)-Ca(2)-O(2)	47.3		
O(1)-Ca(1)-O(2)	28.5		

[a]Ref[123], [b]Ref[121]

Table 2.3: Calculated lattice parameters of HA and MHA for site(1) and site(2) substitutions. Experimental lattice parameters were obtained from Rietveld refinements. Units (Å)

System	Lattice Constant	Site(1)	Site(2)	Exp
HA	a	9.55	-	9.4220(1)
	c	6.94	-	6.8867(8)
MnHA	a	9.32	9.47	9.4205(1)
	c	6.81	6.9	6.8805(9)
FeHA	a	9.52	9.38	9.4212(3)
	c	6.85	6.95	6.8841(2)
CoHA	a	9.50	9.52	9.4197(2)
	c	6.85	6.94	6.8820(1)

the computed XRD patterns from the theoretical model, Figure 2.3. The as-synthesized HA is identified with JCPDF 09-432 and the substituted HA do not exhibit any extraneous peaks, suggesting a single phase in all the powders. Rietveld refinements were performed on the synthesized powders using the refined atomic positions reported by Veselinovic *et al.*[124] The refined lattice parameters of HA and MHA are summarized in Table 2.3, which are in good agreement with the calculated values from DFT assuming a 10 atomic percent substitution. The small differences in peak position between experimental and theoretical diffraction patterns arises from the differences in the calculated and observed lattice parameters. Energy dispersive X-ray spectroscopy was used to assess the stoichiometry of MHA the $(Ca+M^{2+})/P$ ratios were 1.72, 1.71, and 1.69 for MnHA, FeHA, and CoHA respectively which is in good agreement with the theoretical Ca/P ratio of 1.66. From atomic absorption spectroscopy, the M^{2+}/Ca ratios were determined to be 0.07, 0.12, and 0.05 for MnHA, FeHA, and CoHA, respectively. Changes in lattice parameters due to substitution are typically a function of the substituent percentage. Since the transition metal percentage was not controlled, it is difficult to directly compare the effect between transition metals on the lattice parameters.

Chemical analysis indicates that the transition metals successfully replaced calcium in the HA lattice. Between the two distinct calcium sites DFT calculations indicate that the Ca(II)

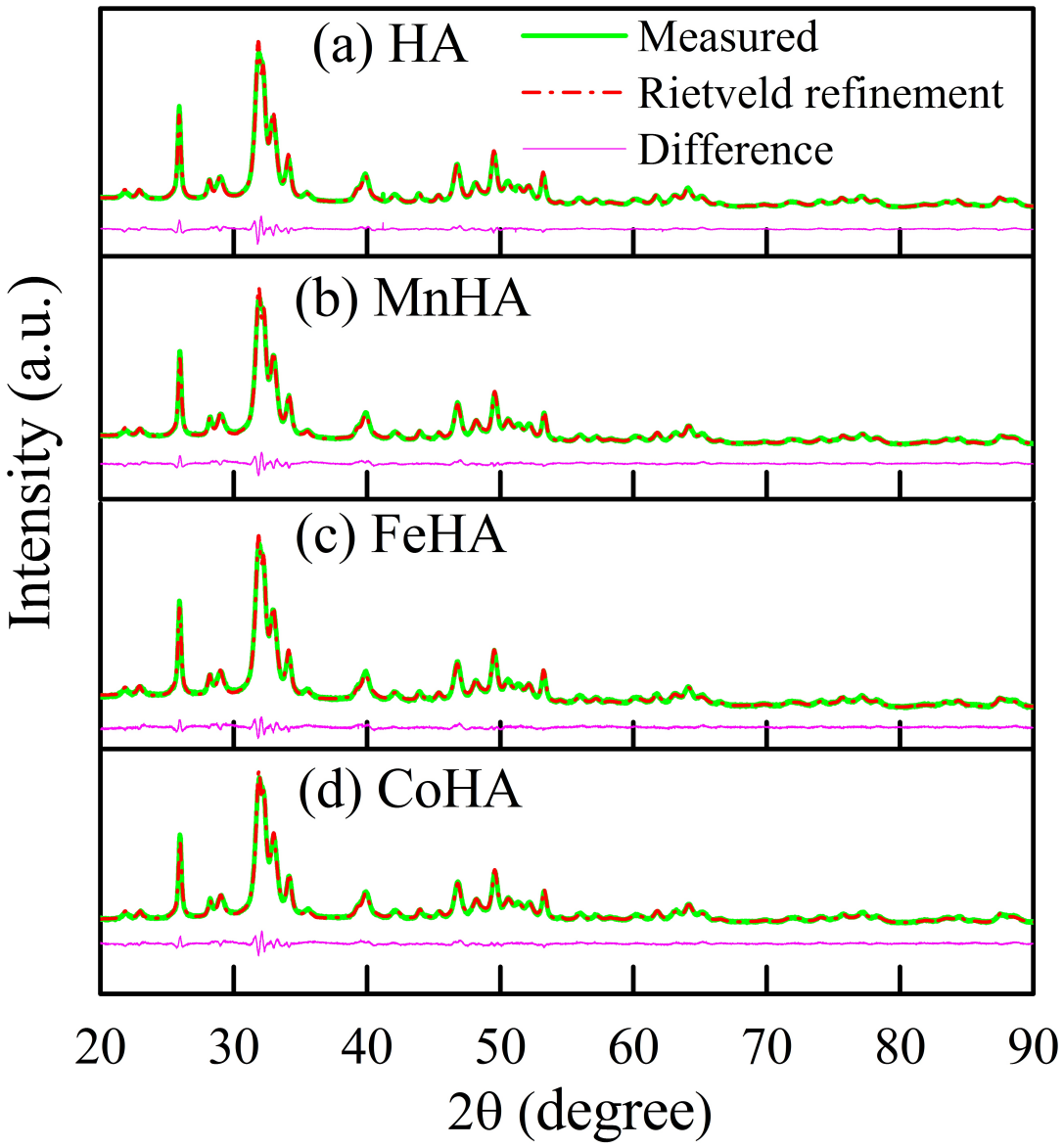

Figure 2.2: Powder XRD patterns of the synthesized HA and M^{2+}HA. HA (a), MnHA (b), FeHA (c), and CoHA (d).

site is the most energetically favorable site for substitution. Experimentally site occupancies cannot reliably be determined since diffraction data was not collected using synchrotron X-rays or with neutron diffraction. Previous experimental and theoretical studies of Sr, Pb, and Cd substituted HA systems utilizing synchrotron radiation have shown that DFT does accurately predict the most energetically favorable site occupancy.[66, 100, 101]

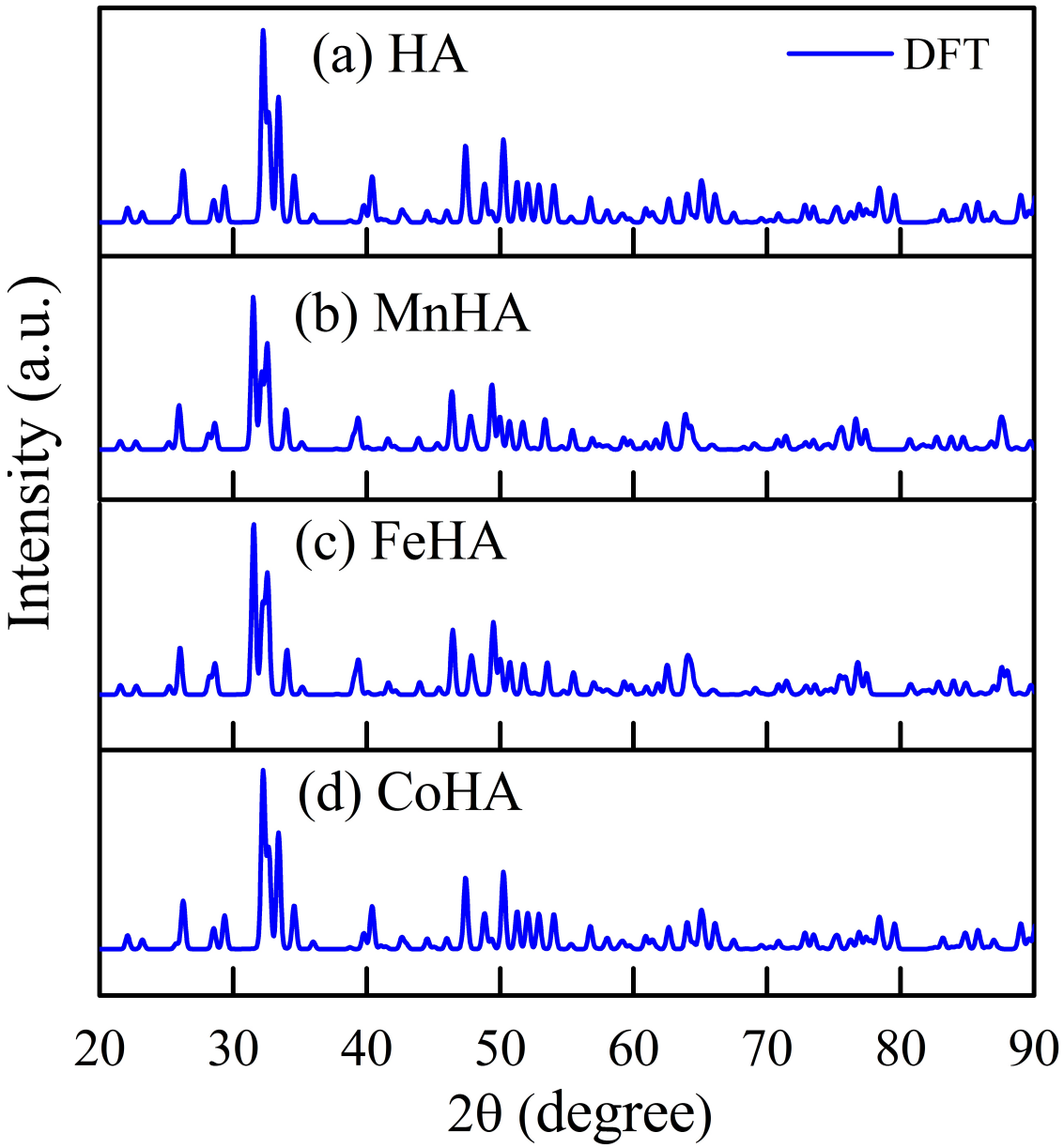

Figure 2.3: Calculated XRD patterns from DFT calculations of HA and M^{2+}HA: HA (a), MnHA (b), FeHA (c) and CoHA (d).

To further understand the effect of transition metals on the structure of hydroxyapatite, DFT calculations were performed on the $Ca_9M(PO_4)_6(OH)_2$ (MHA) systems. Since the valence state of Ca^{2+} and M^{2+} are the same, charge compensation defects were not considered for M^{2+} substitution at the Ca(I) or Ca(II) sites. Table 2.3 displays the calculated lattice parameters of the MHA, which are in good agreement with data obtained from

experiment. The contraction in the lattice parameters of MHA are attributed to the smaller ionic radius and the more electronegative character of Mn^{2+}, Fe^{2+}, and Co^{2+} compared to Ca^{2+}. These differences result in small structural distortions which is seen in the analysis of the interatomic distances of FeHA, shown in Figure 2.1. The observed decrease of the bond length between the Fe and the first neighboring oxygen atoms results from iron being more electronegative than calcium attracting the oxygen atoms closer. The Fe at the Ca(2) results in one broke bond with oxygen, where the O(1) bond is broken.

The FTIR spectra of the pure and substituted HA are displayed in Figure 2.4 along with the corresponding spectra computed using DFT. It can be seen that both results are in good agreement, indicating that the nearest neighbor environments and bond strengths are correctly captured in the DFT computations. There is a difference between the computed and experimental spectra. The error between the experimental and theoretical spectra for HA, MnHA, FeHA, CoHA, are 3.4 %, 3.3 %, 3.8 %, and 4.1 %, respectively. Overall, the theoretical and experimental spectra are in good agreement. Bhat *et al.* observed error ranging from 2 % to 8 % between theoretical and experimental spectra for stoichiometric HA.[110] Also, the theoretical model of a perfect crystal does not take into account defects such as vacancies that are often present in real samples. Bhat *et al.* calculated the IR spectra of calcium deficient HA and observed a shift in the vibrational modes of phosphate to lower wavenumbers.[110] The MHA spectra display typical vibrational modes of HA, indicating successful substitution of M^{2+} into the HA lattice. The vibrational modes of phosphate are observed around 1040 and 1095 cm^{-1} corresponding to the v3 mode, and the v4, v1, and v2 modes are present around 570, 600, and 480 cm^{-1}, respectively. The vibrational and liberation absorption bands for OH^- are observed around 3550 and 640 cm^{-1}, respectively, which are not predicted in the theoretical spectra. Other absorption bands observed in the experimental spectra that are not predicted by theory are the absorption bands observed at 1450, 1410, and 865 cm^{-1}, which correspond to the v3 and out of plane v2 mode for CO_3^{2-}. The presence of the CO_3^{2-} bands is a result of the HA synthesis procedure at ambient

atmosphere. Carbonated HA is formed from the adsorption of CO_2 from the ambient atmosphere. From the position of the CO_3^{2-} bands the substitution of CO_3^{2-} is predominately at the phosphate site.

High resolution XPS spectra of the substituted transition metal in MHA, as shown in Figure 2.5 (a, c, e) and tabulated in Table IV, displays two peaks which are attributed to the $2p_{3/2}$ and $2p_{1/2}$ states from spin-orbit splitting.[125] For MnHA the peaks at 643.4 and 654.6 eV are the $2p_{3/2}$ and $2p_{1/2}$ peak pairs from the spin-orbit splitting, which corresponds with the Mn^{2+} substituted for Ca in the HA lattice.[126] The peaks at 648.0 and 658.8 eV are also 2p peak pairs, but are shakeup satellites of Mn^{2+}. In the case of CoHA the 2p peak pair at 781.1 and 797.1 eV corresponds to Co^{2+} substituted in either Ca site in the HA lattice and the 2p peak pair at 786.5 and 801.9 eV are from shakeup satellites. The strong nature of the shakeup satellite is characteristic of Co^{2+} with paramagnetic properties.[127] The peaks at 711.1 and 720.1 eV in the FeHA spectra are the 2p peak pairs from spin-orbit splitting characteristic of $Fe^{2+}PO_4$ bonding, which corresponds to Fe^{2+}HA in the lattice.[128] The 2p peak pair around 715.4 and 724.5 eV can be attributed to iron residing on surface sites, which requires more energy to create a photoelectron.[128] The last peak pair around 720.1 and 731.9 eV is a shakeup satellite of iron. The O 1s spectra were also acquired and all MHA displayed peaks around 528, 530, 531, and 533 eV. It should be noted that the peak at 531 eV is characteristic of O in HA (NIST database) and the peak around 530 eV is characteristic of surface carbonate (NIST database). The peak at 533 eV is typical of bridging oxygen's. The peak at 528 eV can be attributed to C-O bonding from the carbon tape used for mounting powders. No recognizable metal oxide bonding was identified in the transition metal 2p or O 1s spectra. All the paramagnetic transition metals appear to have successfully incorporated into the HA lattice in a divalent state.

XPS is successful at probing the electronic structure through core level electrons but does not provide information about interactions in the valance band. To address this point, we calculated the band structure and density of states, shown in Figure 2.6, using DFT to

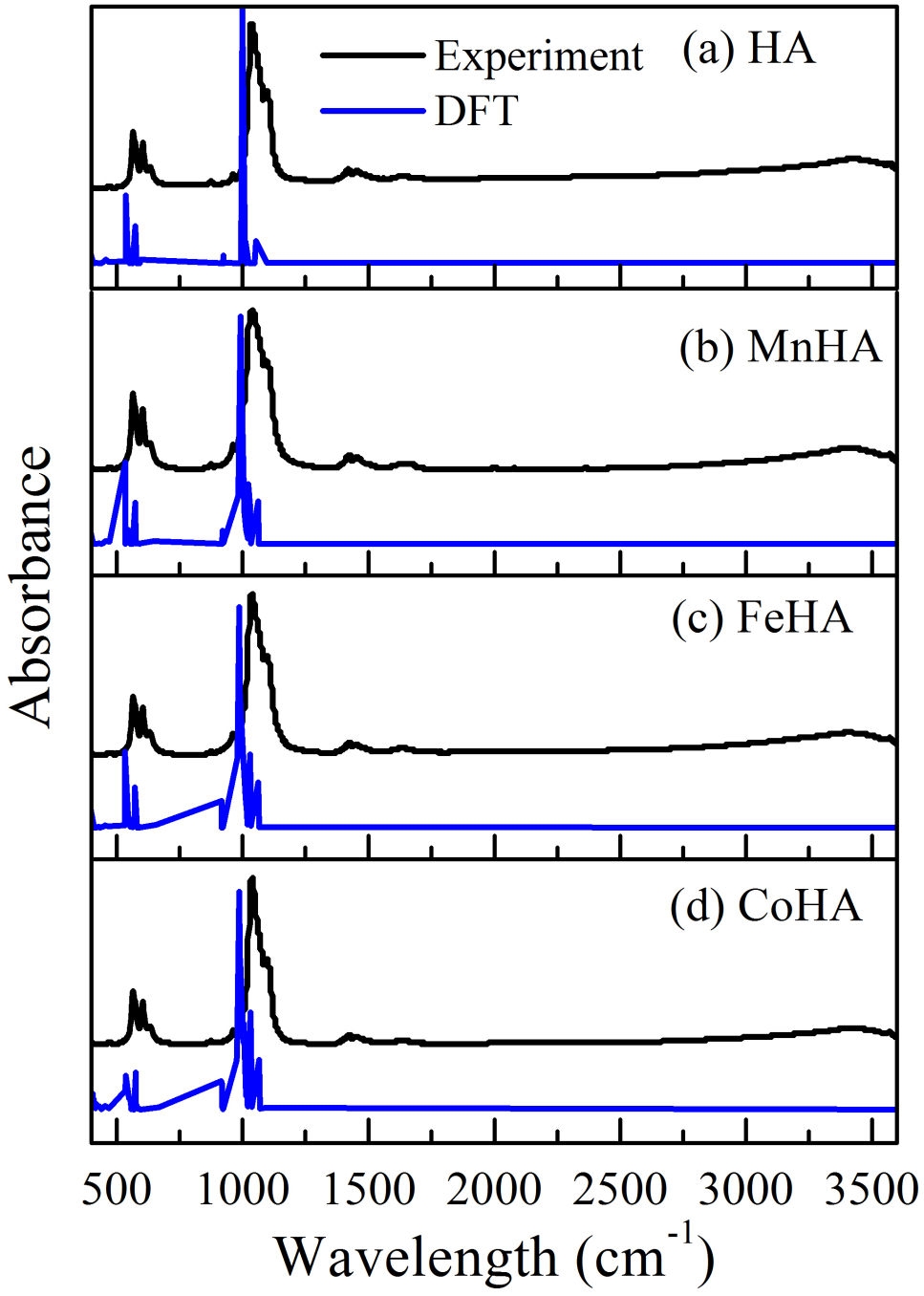

Figure 2.4: FTIR spectra of the synthesized HA and M^{2+}HA. HA (a), MnHA (b), FeHA (c), and CoHA (d).

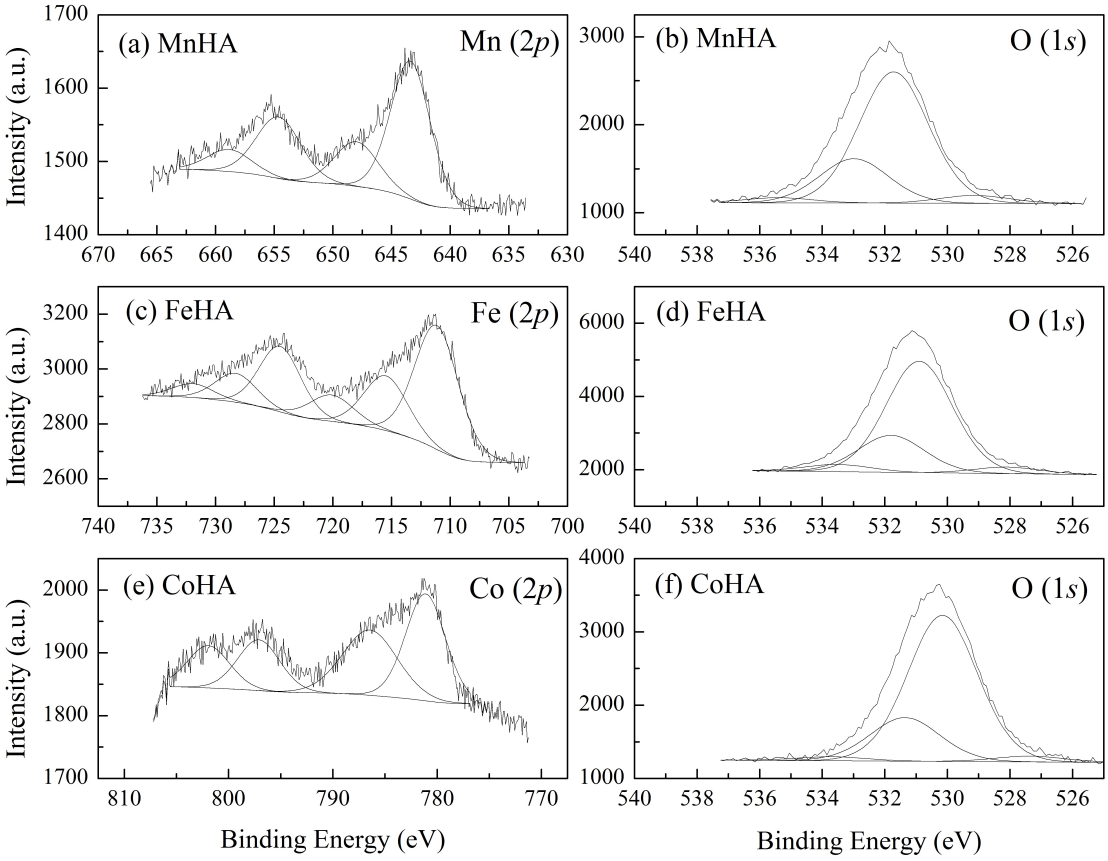

Figure 2.5: XPS spectra of M 2p (left) and O 1s (right) peaks. MnHA (a, b), FeHA (c, d) and CoHA (e, f).

further understand the effect of transition metals on the electronic properties of HA. The valance band maximum of HA is set as 0 eV in all figures, and the calculated PBE band gap of pure HA is 5.09 eV which is consistent with the previously computed result of 5.30 eV from Matsunaga *et al.*[129]

When the transition metals are substituted into HA, the band gap of the MHA decreases compared to pure HA as shown in Figure 2.6 and Table 2.5. In order to describe the influence of specific atoms on the electronic structure of HA, density of states (DOS) and projected density of states analysis were performed, as shown in Figure 2.6. Comparing to the partial DOS of pure HA, new energy states of ion-substituted HA are introduced at the top of the valence band owing to the interaction between 2p states of O and the 3d energy states of Fe, Co, and Mn. The interaction between these states results in decreasing the

Table 2.4: Peak positions from deconvoluted MHA transition metal (M) 2p spectra in eV.

	M					
	$2p_{3/2}$			$2p_{1/2}$		
MnHA	643.4	648.0		654.6	658.8	
FeHA	711.1	715.4	720.1	724.5	728.3	731.9
CoHA	781.8	786.5		797.1	801.9	

Table 2.5: Band gap of MHA, given in eV. The data in parenthesis is experimental results from literature

System	Site(1)	Site(2)
HA	5.09	(5.3[a])
MnHA	4.29	3.3
FeHA	4.15	3.8
CoHA	4.29	4.36

[a]Ref[129]

band gap in MHA.

Also, when Fe or Mn is substituted at the Ca(2) site, the band gap is smaller than substitution at the Ca(1) site. The structural distortion from Fe, Mn, and Co at site (1) is less compared to site (2) substitution. The coordination number of Fe, Mn, and Co at site (1) is the same as that of Ca(1), which is 9. Small variations of structure leads to extension of the band tail. However, the interaction between Fe (or Mn) at site (2) and the OH ion lead to the rotation of the OH ion, which results in the production of discrete states in the band structure of HA.

Magnetization measurements depicted in Figure 2.7 show that all the substituents induced a transition from diamagnetic behavior, which is characteristic of HA, to a superparamagnetic behavior. A small ferromagnetic signal is observed at low magnetic fields followed by a strong paramagnetic response at high fields. The observed superparamagnetic response may be due to M^{2+} residing in Ca(2) sites or surface effects as previously discussed.[65] In brief, as the surface to volume ratio increases, a larger number of atoms

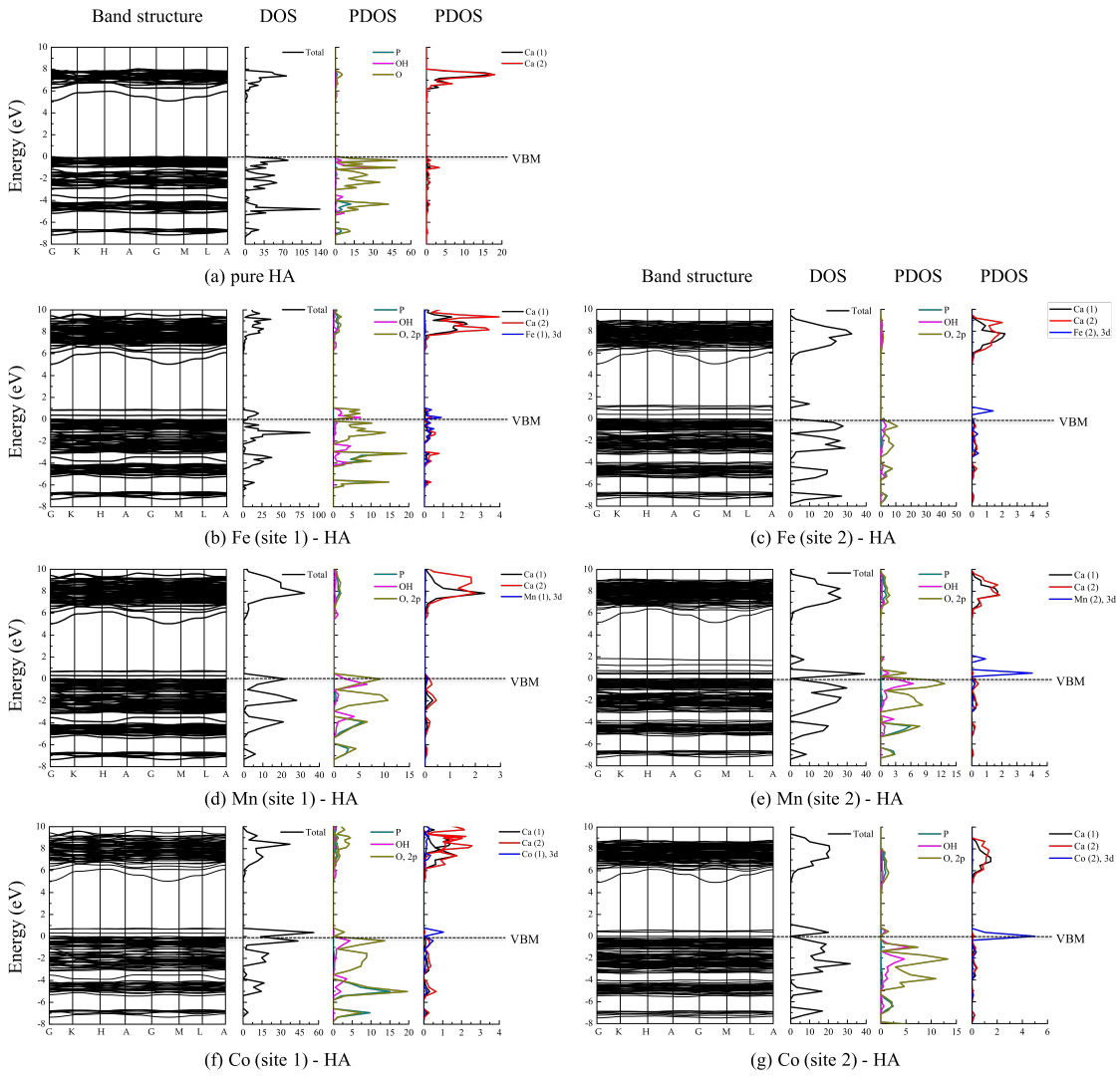

Figure 2.6: Projected density of states for M^{2+}HA.

reside on the surface possibly resulting in dangling bonds, a change in coordination and surface disorder, which can lead to an increase in their magnetization values.[130] The transition from diamagnetic to paramagnetic response is in agreement with the theoretical calculations. For a 10 percent substitution on the Ca-site, our theoretical modelling predicts magnetic moments of 5, 4 and 3 Bohr magnetons for MnHA, FeHA, and CoHA, respectively. Since the MHA fabricated by different approaches have varying levels of M^{2+} substituted into the lattice, magnetization curves were normalized to the molar amount of M^{2+} per MHA. In agreement with the calculations, MnHA displayed the highest magnetization value

of 100 emu/mol M^{2+} at 10 kOe (or 1 tesla) of all the substituents, while FeHA and CoHA had similar magnetization values around 65 emu/mol M^{2+}. Qualitatively, the slope of the high field magnetization data is also indicative of the magnitude of the magnetic moment and the observed slopes are MnHA > FeHA > CoHA, which is in good agreement with the theoretical calculations.

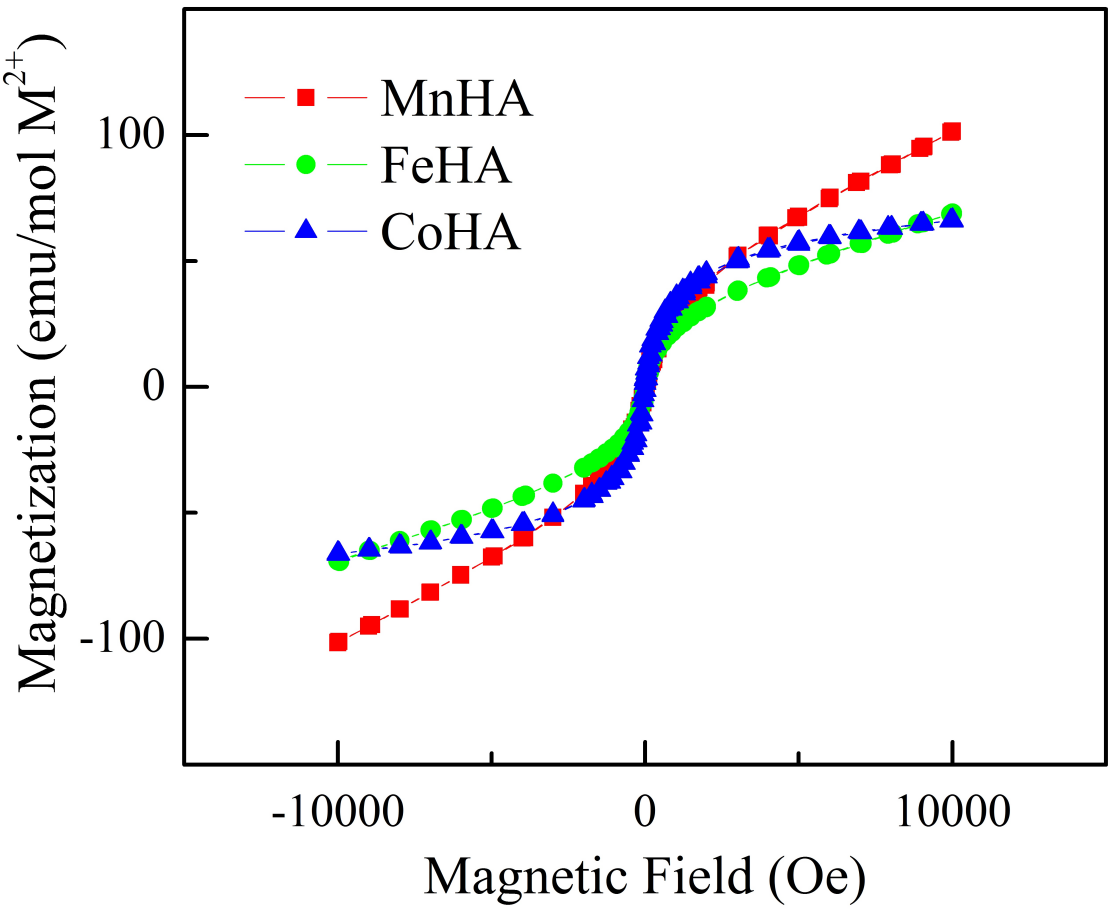

Figure 2.7: Mass magnetization of MnHA, FeHA, and CoHA normalized to the transition metal content.

2.5 Conclusion

Manganese, iron and cobalt were successfully substituted into hydroxyapatite (HA) and the observed crystal structure, FTIR spectra, electronic and magnetic properties were in

good agreement with DFT calculations. The presence of transition metals in a +2 oxidation state was confirmed by XPS; FTIR and XRD identified the MHA without any detectable impurity phases. Incorporation of magnetic ions into the HA lattice was sufficient to induce a transition from the diamagnetic behavior (for pure HA) to a paramagnetic one, with the observed magnetization values in the order of MnHA >FeHA >CoHA.

The results from DFT calculations were in good agreement with experimental data. Thus, the DFT calculation could be a useful tool for predicting physical and magnetic properties of different ion-substituted hydroxyapatite powders, and such a tool can guide future studies on the synthesis of ion-substituted hydroxyapatite with desired properties.

CHAPTER THREE

Synthesis and Characterizaiton of Iron-Substituted Hydroxyapatite

3.1 Introduction

Magnetic nanoparticles (NPs) have enticed significant interest as theranostic agents.[1–7] owing to the ability of an external magnetic field to non-invasively penetrate tissue allowing potential 'remote' control over the particles. Remote applications include: contrast enhancement for magnetic resonance imaging, hyperthermia, cell stimulation, and targeted drug delivery.[1, 2, 4, 7–10] Magnetic particles with superparamagnetic behavior are ideal for the aforementioned applications. Superparamagnetic behavior is characterized by a large magnetic moment in the presence of an applied magnetic field and a zero remanent magnetic moment when the applied magnetic field is reduced to zero. This property allows for 'remote' control over particles, and thus is ideal for *in vivo* applications.[2]

Iron oxides are commonly used for biomedical applications, since nanoparticles of iron oxide synthesized below 30 nm render the particles superparamagnetic due to small size effects.[131–133] Along with lucrative magnetic properties, the small size of these particles can avoid the body's system of macrophages, the reticuloendothelial system (RES), which clears foreign debris prolonging blood circulation time.[134] However, adsorption of proteins from blood plasma will reduce the NPs circulation time. To improve the blood circulation time, surface functionalization with polyethylene glycol is performed to prevent protein adsorption.[135–138] Despite iron being a daily elemental need, the poor biodegradation and acute toxicity[47] have raised concerns over the application of iron oxides to medical applications.

To circumvent the issue of biodegradation and acute toxicity concerns, a few research groups have focused on doping biocompatible materials with magnetic ions to impart

magnetic properties.[60–63, 139] An ideal material for this approach is hydroxyapatite (HA), ($Ca_{10}(PO_4)_6(OH)_2$), the mineral phase of bone, which due to its unique structure allows for a wide array of substitutions. The structure of HA, space group $P6_{3/m}$, allows for substitution of the calcium sites by divalent or trivalent cations and the hydroxyl site by other anions. In the structure of HA, calcium occupies two distinct sites: (i) the Ca(II) site forms triangles staggered by 60° around the hydroxyl channel, while (ii) the Ca(I) site forms a channel surrounded by phosphates. Substitution of the calcium site with metal ions such as strontium have exhibited enhanced bioactivity, while substitution of the hydroxyl site with fluorine leads to improved crystallinity and thermal stability.[140, 141]

In regards to magnetic impurities, iron substitution has been shown to induce an intrinsic paramagnetism in HA along with maintaining biocompatibility.[60–62] Iron substituted HA (FeHA) has been synthesized via multiple approaches: hydrothermal, co-precipitation, and ion exchange.[60, 63] The iron source is typically a salt of Fe^{2+} or Fe^{3+}; different groups have noted paramagnetic or superparamangetic properties of HA from iron substitution depending upon the oxidation state of iron.[60, 63] For example, Panseri *et al.* observed superparamagnetic properties in FeHA prepared by a neutralization wet synthesis method that resulted in FeHA with a minimal amount of iron oxide produced as a second phase.[60]

An alternative approach to co-precipitation is cation exchange, in which immersion of an ionic material into an aqueous solution results in the replacement of a cation within the crystal lattice with a cation from the solution. Cation exchange is easily accomplished at room temperature and within a short time scale. Herein we report a facile approach utilizing cation exchange to manipulate the magnetic properties of FeHA. Its magnetic properties varied from paramagnetic to superparamagnetic and was dependent upon the oxidation state of iron and the particle size of FeHA samples.

3.2 Materials and Methods

3.2.1 Materials

The following materials were purchased from Acros Organics with a purity greater than 99%: iron chloride tetrahydrate, o-phenanthroline, hydroxylamine hydrochloride, ammonium phosphate dibasic, iron chloride hexahydrate (97+%), and potassium bromide (IR grade). Calcium nitrate tetrahydrate (99+%) , ammonium hydroxide (29.45%), sodium acetate (99+%) and glacial acetic acid were purchased from Fisher Scientific.

3.2.2 HA and FeHA synthesis

HA was synthesized via a wet chemical method. In this method, an aqueous solution of ammonium phosphate dibasic was added drop-wise to an aqueous calcium nitrate solution with the calcium to phosphate ratio maintained at 1.667. Then the solution was heated to 95 °C for five hours and cooled to room temperature. After two days of ageing, the precipitates were collected via centrifugation and washed three times with de-ionized water (DIW). FeHA was fabricated via a cation exchange method. For this, previously synthesized HA powder was immersed in an iron salt solution and sonicated for one hour. The iron salt solutions were composed of $FeCl_2$ (Fe^{2+}HA), $FeCl_3$ (Fe^{3+}HA), and $FeCl_2$ with and equal amount of $FeCl_3$ (Fe^{2+3+}HA); all solutions had a total iron concentration of 0.02 M. Substituted hydroxyapatite powders were collected via centrifugation and rinsed three times with DIW.

3.2.3 Characterization

Particle size and morphology were characterized with a JEOL 6330F field emission scanning electron microscope (FESEM) equipped with an energy dispersive X-ray spectroscopy (EDXS) which was used to verify the presence of iron and to determine the (Fe+Ca)/P ratio. EDXS analysis was performed on four randomly selected areas of HA and FeHA powders.

The atomic percentages were quantified through a semi-quantitative method and the results of the four areas were averaged together. The phase purity of HA and iron substituted HA was examined by X-ray diffraction (XRD) with a Bruker D2 Phaser X-ray diffractometer and a copper target. Scans were collected over 2-θ range of 10-70° with a step size of 0.02° and a scan rate of one second per step. Small-range XRD patterns of the (002) and (211) peaks were acquired over a 2-θ range 25-27° and 31-33°.

Fourier transform infrared spectroscopy (FTIR) was used to determine the functional groups present in the samples. FTIR spectra were obtained with a Nicoltet Magna 560 FTIR spectrometer; the potassium bromide method for pellets was used for specimen preparation. Powder samples were diluted to 0.1 weight percent in KBr and grinded into a fine powder. The powder mixture was pressed into a transparent pellet and FTIR spectra were acquired over the range of 4000 to 400 cm^{-1}.

The pH change of the iron salt solution during ion exchange was recorded using a pH meter (Accumet Excel XL15). The pH value of the solution was measured every minute, and the pH profile versus time was plotted for each ion exchange. The start of ion-exchange occurs when HA powder is added to the ion exchange solution, which corresponded to time zero. A HA control was performed, where the pH of DIW was adjusted to 2.2 with 1 N HCl and the HA powder was immersed in the pH adjusted DIW and sonicated for one hour. The pH profiles were recorded during the sonication process.

Iron quantification in fabricated powders was determined via a colorimetric assay.[142] In brief, iron was extracted by dissolution with dilute hydrochloric acid. Then any ferric iron was reduced to ferrous iron with a 10 % (w/v) solution of hydroxylamine hydrochloride. The solution was then buffered to a pH of 4 with a 0.5 M acetate buffer. Any iron in solution was converted to a vibrant red color with the addition of a 0.3 % (w/v) o-phenanthroline solution. The absorbance of the solution was measured at 510 nm. In order to assess the nature of iron bonding, X-ray photoelectron spectroscopy (XPS) was employed using a VG X-ray Photoelectron Spectrometer with Mg Kα radiation source. High resolution XPS

spectrums of the Fe 2p and O 1s peaks were acquired over the range of 705-735 and 525-540 eV. To account for sample charging, spectrums were calibrated by setting the adventitious carbon peak to 284.5 eV. De-convolution of high resolution XPS spectrums was performed with the CasaXPS software.

The magnetization of the FeHA were determined using a vibrating sample magnetometer (VSM) attached to the evercool physical property measurement system (from Quantum Design). Magnetization measurements were carried out at 298 K and with applied DC magnetic fields of up to one tesla.

3.3 Results and Discussion

3.3.1 Results

FESEM images of the as-synthesized HA and ion exchanged FeHA are displayed in Figure 3.1. HA particles displayed a spherical morphology with a particle size of approximately 49 nm, and ion exchanged particles displayed a spherical morphology with a slightly smaller size than HA. Fe^{2+}HA, Fe^{2+3+}HA, and Fe^{3+}HA have average sizes of 41, 46, and 47 nm, respectively. A secondary morphology of small rods and aggregates were observed in all samples. The presence of iron was verified from EDXS spectrums, as shown in Figure 3.2. A significant iron peak is seen in the spectra for all FeHA samples and there is no observable iron peak in the spectra for the as-synthesized HA. In contrast to Fe^{2+}HA and Fe^{2+3+}HA, the Fe^{3+}HA spectra displayed a significant peak from chloride.

X-ray diffraction patterns of all FeHA are shown in Figure 3.3. The as-synthesized HA was identified with JCPDF 09-432, and FeHA powders did not exhibit any extraneous peaks. All peaks are broadened and the intensities are attenuated in all three FeHA powders. The most significant attenuation and broadening occurred in Fe^{3+}HA. A shift to larger Bragg angles was observed for the (002) plane for all FeHA powders. The peak shift for the (211) plane largely depended upon the oxidation state of iron. The peak was shifted to a lower

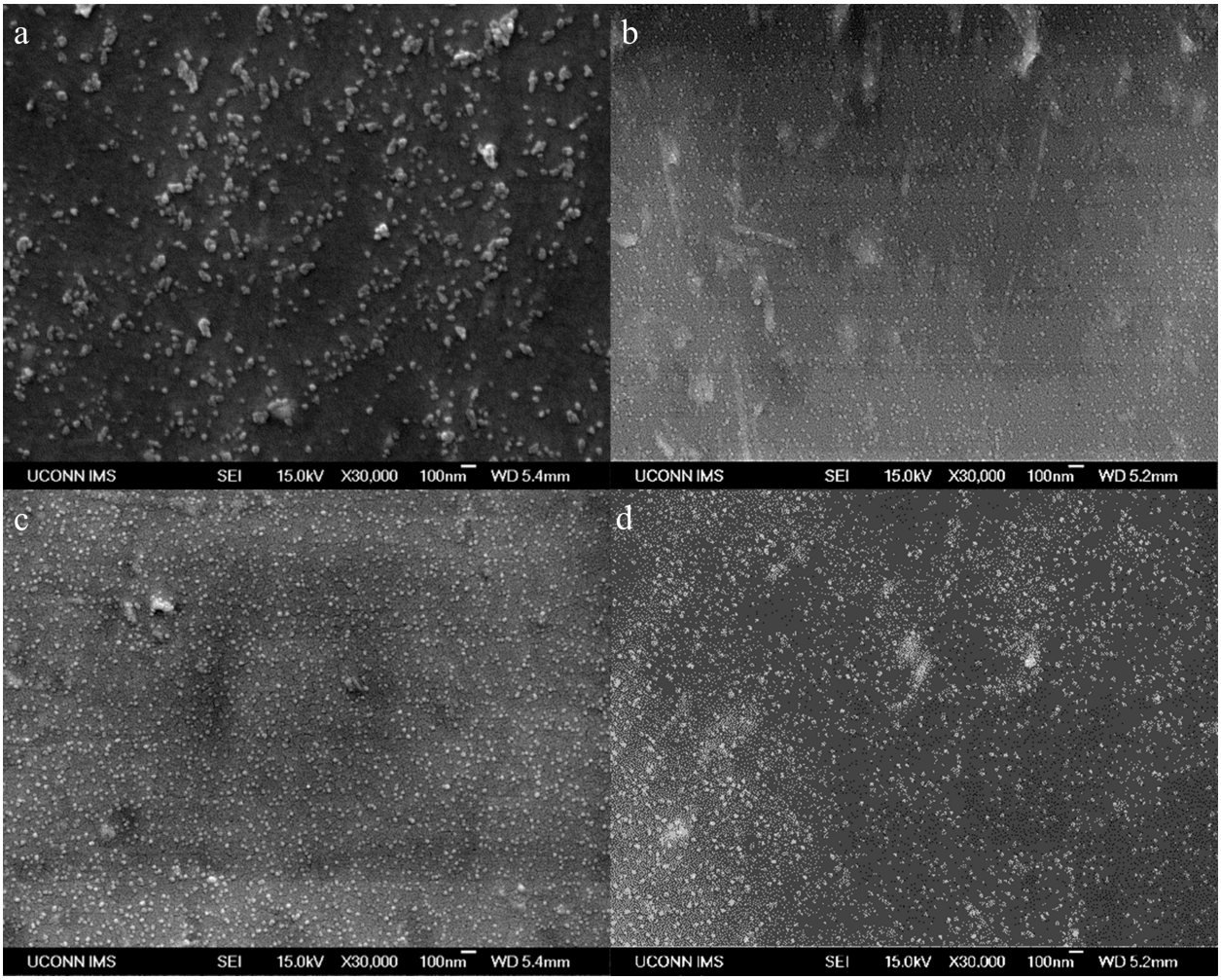

Figure 3.1: FESEM images of particle morphology for HA (a), Fe^{2+}HA (b), Fe^{2+3+}HA (c), Fe^{3+}HA (d).

Bragg angle for Fe^{3+}HA and a higher Bragg angle for Fe^{2+}HA, while Fe^{2+3+}HA exhibited no observable shift.

The FTIR spectrum of the as-synthesized HA and FeHA are displayed in Figure 3.4. The HA spectrum displayed vibrational modes at 1030 and 1095 cm^{-1} corresponding to the v3 mode of phosphate. The v4 and v1 modes of phosphate were present at 563 and 602 cm^{-1}, respectively. The absorption band at 3550 and 625 cm^{-1} arise from the vibrational mode and liberation of the hydroxyl group. The as-synthesized HA was partially carbonated with absorption bands for the v3 mode and out of plane v2 mode for CO_3^{2-} observed at 1450,

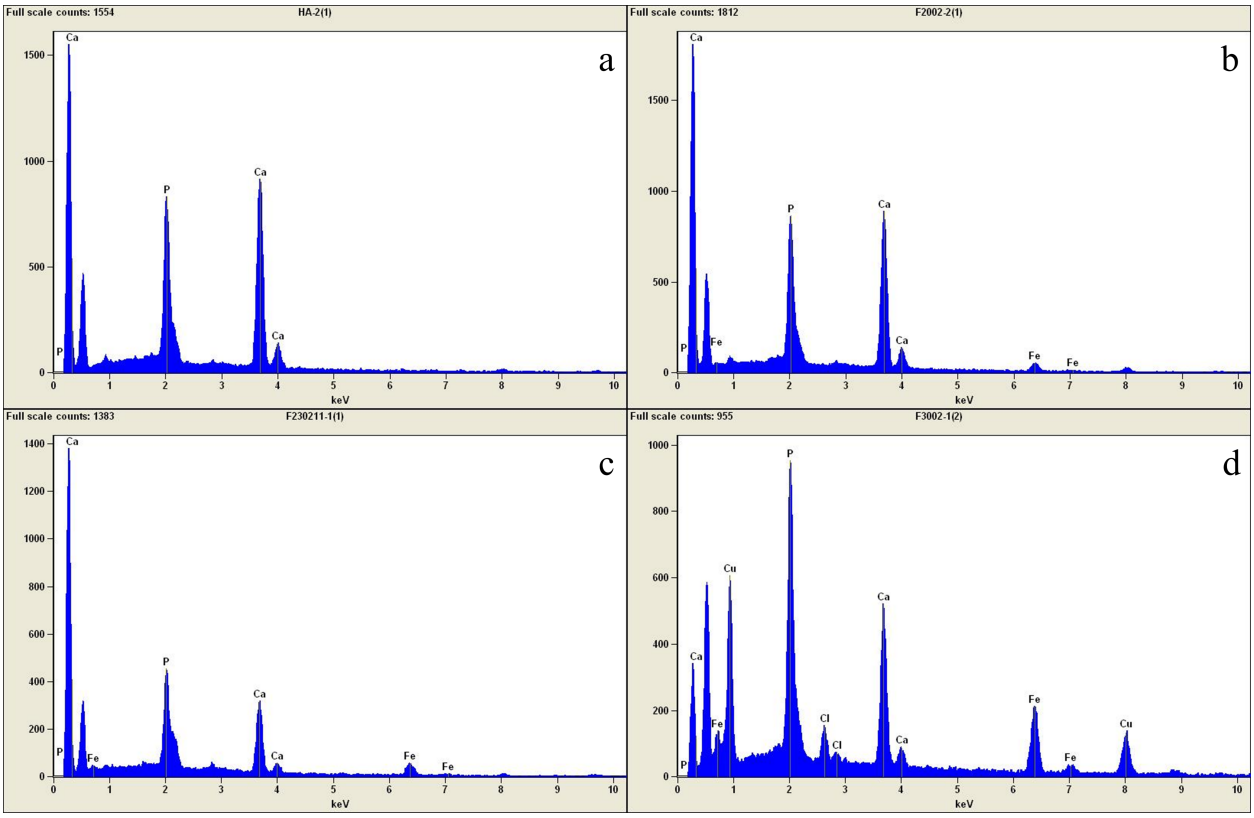

Figure 3.2: Representative EDXS spectra of HA (a), Fe^{2+}HA (b), Fe^{2+3+}HA (c), Fe^{3+}HA (d).

1410 and 865 cm^{-1}, respectively. All FeHA powders displayed the same absorption bands as HA. A noticeable attenuation in the CO_3^{2-} and an increase in the v2 absorption band of water around 1625 cm^{-1} were observed for FeHA fabricated with a Fe^{3+} salt. Also, the hydroxyl band at 3550 cm^{-1} was reduced to a shoulder in the water band for Fe^{3+}HA and was attenuated in other samples fabricated with a Fe^{3+} salt source.

The observed pH profiles of the ion-exchange process are depicted in Figure 3.5. A rapid rise in pH was observed at the time corresponding to the addition of HA powder to the solution. The pH value peaked within five minutes followed by a gradual decline. Fe^{2+3+}HA had the largest change in pH going from 2.3 to 4.3 followed by Fe^{3+}HA (1.8 to 3.7) and Fe^{2+}HA (3.0 to 4.5). These changes in pH are less than the observed pH change in the HA control where the pH changed from 2.2 to 5.0.

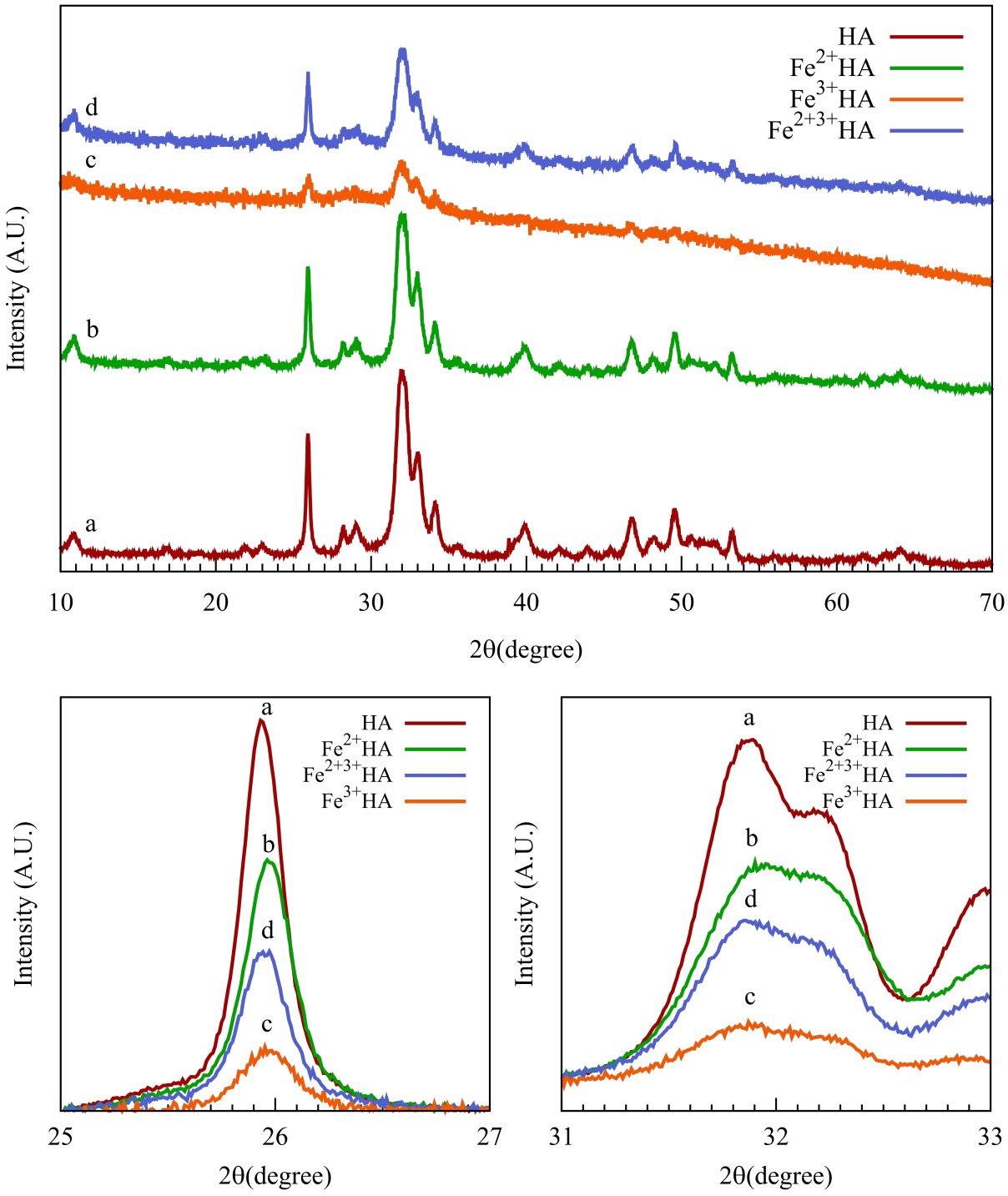

Figure 3.3: Top: powder XRD patterns of HA and FeHA powders. Bottom left: XRD pattern of the (002) peak. Bottom right: XRD pattern of the (211) peak. HA (a), Fe^{2+}HA (b), Fe^{3+}HA (c), and Fe^{2+3+}HA (d).

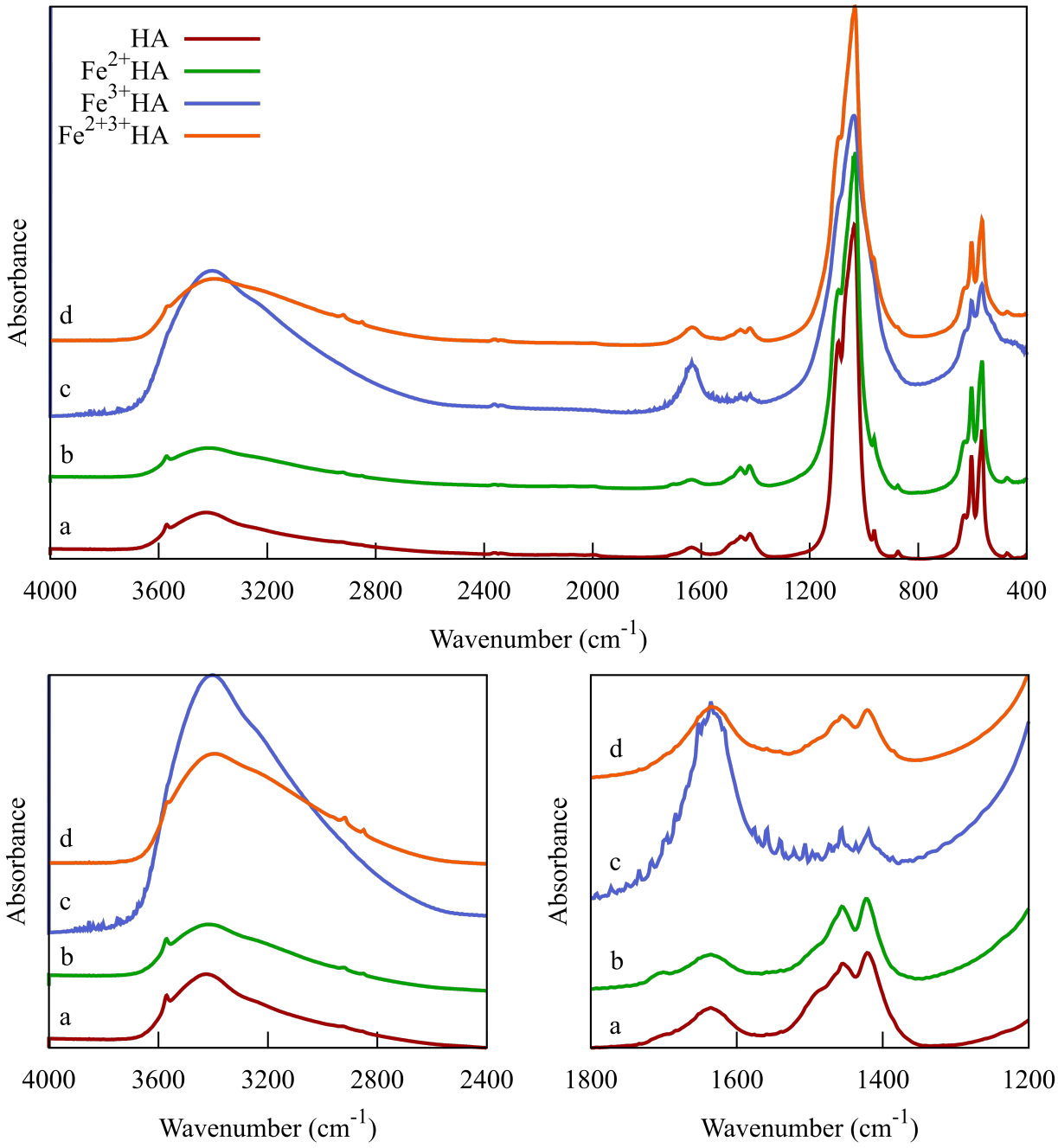

Figure 3.4: Top: FTIR spectrum of HA and FeHA powders. Bottom left: observed attenuation of the hydroxyl band in FeHA specimens with Fe^{3+}. Bottom right: reduction in the carbonate bands and increase in the water band for FeHA specimens with Fe^{3+}. HA (a), Fe^{2+}HA (b), Fe^{3+}HA (c), and Fe^{2+3+}HA (d).

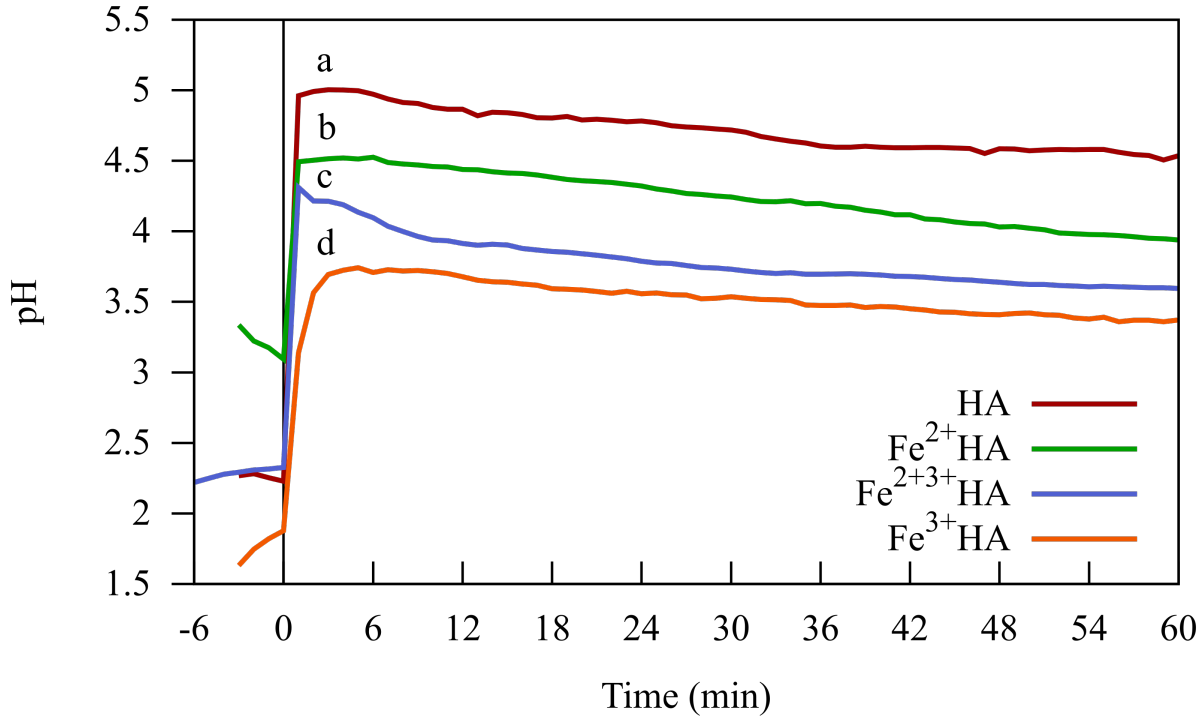

Figure 3.5: pH profile of the ion exchange process. HA (a), Fe^{2+}HA (b), Fe^{2+3+}HA (c), and Fe^{3+}HA (d). Time zero corresponds to the addition of HA to the solution. HA in DIW with a pH of 2.2 was used as a control.

The total iron content in each specimen was first assessed with EDXS and XPS to determine the bulk and surface (Ca+Fe)/P ratios as shown in Table 3.1, followed by analysis with a colorimetric assay. The (Ca+Fe)/P for HA (1.66), Fe^{2+}HA (1.65), and Fe^{2+3+}HA (1.63) are in good agreement with the stoichiometric Ca/P ratio of 1.67, while Fe^{3+}HA displayed a non-stoichiometric ratio of 1.36. In contrast, XPS analysis displayed non-stoichiometric (Ca+Fe)/P ratios: 1.39 (Fe^{2+}HA), 1.25 (Fe^{2+3+}HA), and 1.04 (Fe^{3+}HA) for all three powders studied. Quantification of the total iron content showed that Fe^{3+}HA had the most iron at 11.9 wt% followed by Fe^{2+3+}HA, 9.9 wt%, and Fe^{2+}HA, 4.5 wt%.

High resolution spectra of the iron peak, Figure 3.6 (a,c,e), displayed two peaks around 711-713 eV and 724-726 eV, which are attributed to Fe $2p_{3/2}$ and Fe $2p_{1/2}$, respectively. The Fe 2p peaks were resolved into two peaks. The main peaks for Fe $2p_{3/2}$ were observed around 712 and 717 eV for Fe^{2+}HA, 710.5 and 714 eV for Fe^{2+3+}HA, and 713 and 718 eV

Table 3.1: Fe+Ca/P ratio determined by EDXS and XPS

	Fe+Ca/P		Fe/Ca	
	EDXS	XPS	EDXS	XPS
HA	1.66	–	–	–
Fe^{2+}HA	1.65	1.394	0.115	0.277
Fe^{2+3+}HA	1.63	1.043	0.439	0.473
Fe^{3+}HA	1.36	1.252	0.952	0.762

Table 3.2: Peak positions of deconvoluted Fe 2p and O 1s spectras in eV.

	Fe $2p_{3/2}$		Fe $2p_{1/2}$		O 1s			
Fe^{2+}HA	712.2	717.8	725.2	730.7	528.6	530.7	531.1	532.9
Fe^{2+3+}HA	710.5	714	723.7	725	528.4	530.9	531.7	533.1
Fe^{3+}HA	713.2	718	726.5	730.8	529.5	531.2	532.2	533.8

for Fe^{3+}HA. High resolution spectra of O 1s peak were also aquired, as shown in Figure 3.6 (b,d,f), with one peak observed around 531.6-531.9 eV. The O 1s peak was deconvluted into 4 peaks with the main peak observed around 531 eV for all FeHA. The second major peak was observed around 530 eV in Fe^{2+}HA and Fe^{2+3+}HA, while it was observed around 532 eV in Fe^{3+}HA. All the peak positions determined from the deconvolution of the spectra are listed in Table 3.2.

Magnetic properties were affected by iron oxidation state and particle size, as illustrated in Figure 3.7. Fe^{3+} substitution resulted in paramagnetism as seen in magnetic data of Fe^{3+}HA., while Fe^{2+} resulted in superparamagnetism as observed in magnetic data of Fe^{2+}HA. The combination of Fe^{2+} and Fe^{3+} resulted in superparamagnetic properties as it was observed for Fe^{2+3+}HA. The influences of particle size and shape on magnetic properties of the HA particles were also investigated. The HA synthesis procedure was modified to produce HA with needle shape morphology and a particle size of 300 nm. Larger Fe^{2+3+}HA particles resulted in paramagnetism, which is in contrast to the superparamagnetism observed in Fe^{2+3+}HA with a more spherical morphology and particle size around 45 nm.

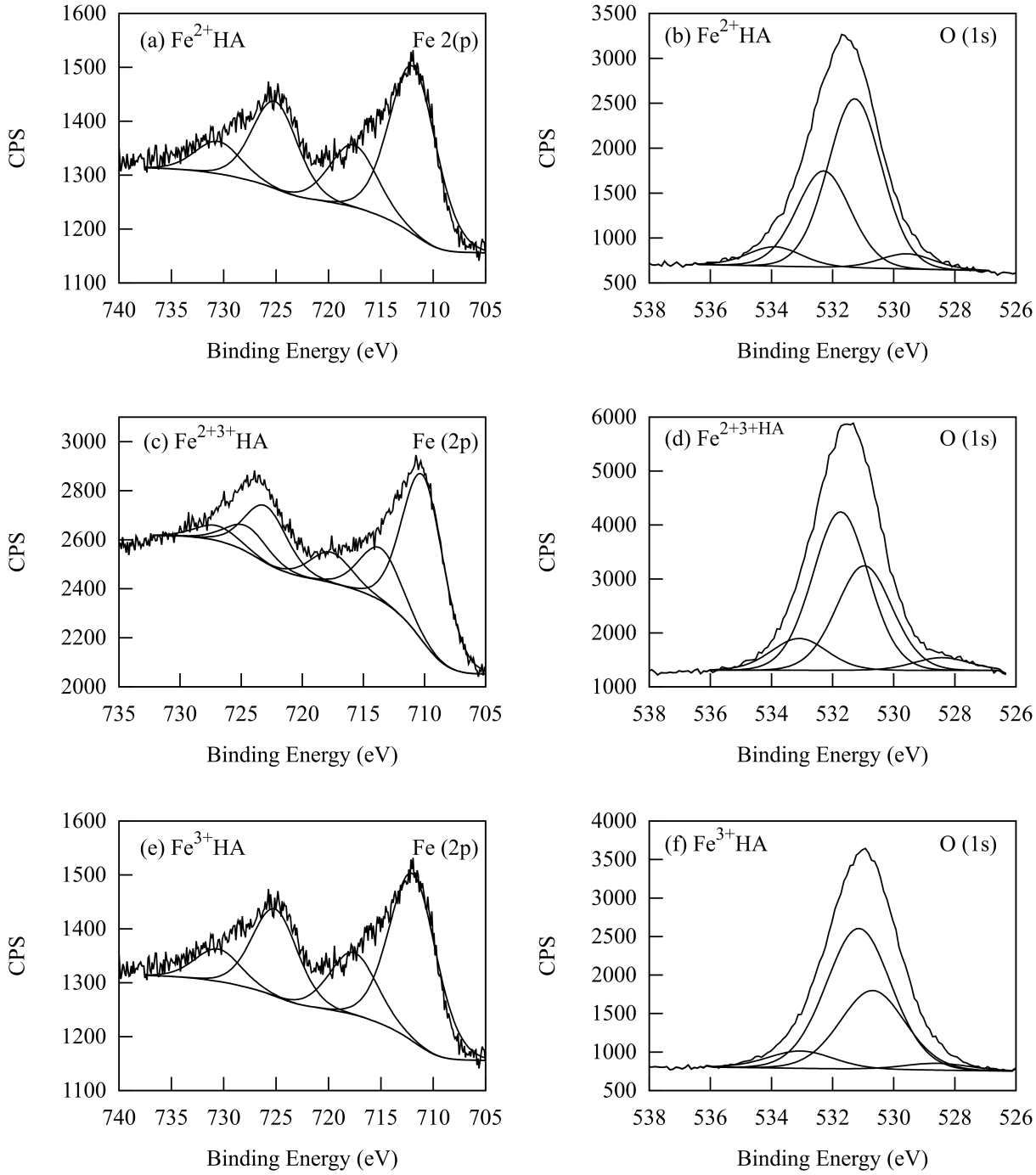

Figure 3.6: High resolution XPS spectrum and deconvolution of Fe 2p (a, c, and e) and O 1s (b, d, and f). Fe^{2+}HA (a dn b), Fe^{2+3+}HA (c and d), Fe^{3+} (e and f).

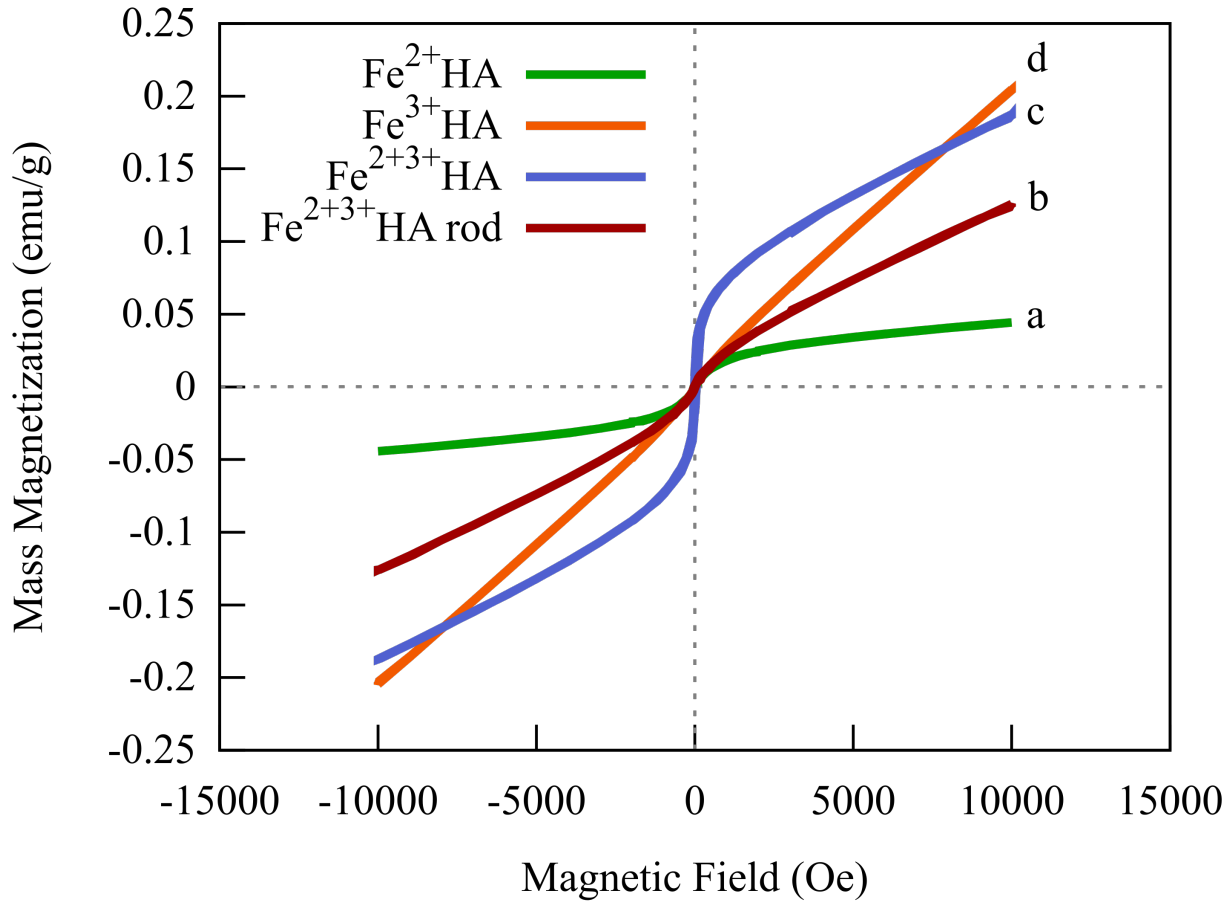

Figure 3.7: Magnetization measurements of Fe^{2+}HA (a), Fe^{2+3+}HA with a needle like morphology (b), Fe^{2+3+}HA (c), and Fe^{3+}HA (d).

3.3.2 Discussion

Utilizing the ion exchange property of HA we investigated the influence of the oxidation state of iron precursors on the magnetic properties of FeHA. The substitution of iron did not affect the particle morphology or size. The phase purity of HA was also maintained post substitution as seen from the absence of extraneous peaks in the XRD patterns (Figure 3.3). The observed peak shifts are indicative of iron substitution into calcium sites due to changes in the lattice parameter resulting from differences in ionic radii and vacancy formation. Substitution of Fe^{2+} and Fe^{3+} resulted in a contraction of the c-axis as observed from peak shifts to larger Bragg angles. The broadening and reduction in intensity is due to

increased lattice strain from iron substitution, since the radii of Ca^{2+} is greater than Fe^{2+} and Fe^{3+}. The formation of calcium vacancies is depicted in Figure 3.8 and discussed later.

FTIR spectra (Figure 3.4) of FeHA specimens displayed the observed vibrational modes from the v1, v3 and v4 modes of phosphate, the OH mode and the v2 mode of carbonate as observed in HA, further indicating successful substitution of iron. The as-synthesized HA is partially carbonated due to CO_2 adsorption from the atmosphere during the synthesis process. Carbonate substitution can occur at either the PO_4^{3-} or OH^- site; these substitutions are distinguished by absorption bands around 1540, 1460 and 878 cm^{-1} for OH^- and 1455, 1420 and 871 cm^{-1} for PO_4^{3-} substitutions. Absence of the absorption band around 1540 cm^{-1} suggests that the carbonate incorporation predominately resided at the PO_4^{3-} sites. The reduction in intensity of the carbonate band in specimens prepared with Fe^{3+} salt source is attributed to the dissolution and precipitation process during ion exchange. During this process Fe^{3+} bonds to the PO_4^{3-}, as indicated by XPS in Figure 3.6 (e), and not carbonate. The precipitation process results in exclusion of carbonate from a lack of reactivity with Fe^{3+}.

The cation exchange process can occur in two manners: (1) formation of a reaction zone[143] with simultaneous dissolution and precipitation occurs and/or (2) cations (e.g. Fe^{3+}) adsorb to the surface and diffuse into the material with concurrent substituted cation (e.g. Ca^{2+}) release. For iron substitution the dominant mechanism is process (1), the acidic condition of the iron solution induces partial dissolution of HA and the phosphate ions react with iron[144] to introduce iron into the lattice. The partial dissolution of HA resulted in a rapid rise in the pH of the solution from the release of OH^- ions, which is observed in the change of the pH profile upon the addition of HA powder. After the rapid rise in pH the re-precipitation process resulted in a gradual decline in the pH as OH^- and iron ions have precipitated into FeHA. The amount of iron incorporated is related to the initial pH of the solution. Lower pH values correspond to higher iron activity and a greater degree of HA dissolution, which results in more iron substitution. The initial pH values were 1.8,

2.3 and 3.0 for Fe^{3+}, Fe^{2+3+}, and Fe^{2+} solutions, respectively. As such, the amount of iron substitution in HA followed the following order: Fe^{3+} is greater than Fe^{2+3+} which is greater than Fe^{2+}.

The incorporation of Fe^{3+} decreases the crystallinity of HA, which can be attributed to the non-stoichiometric substitution of Fe^{3+} for Ca^{2+}. The charge imbalance can be compensated by a number of mechanisms (Figure 3.8): formation of calcium vacancies (reaction (1)), deprotonation of the hydroxyl group (reaction (2)), or a combination of calcium and hydroxyl vacancies (reaction (3)).

$$3Ca^{2+} \longrightarrow 2Fe^{3+} + Ca^{2+}_{vac} \tag{1}$$

$$Ca^{2+} + OH^{-} \longrightarrow Fe^{3+} + O^{2-} \tag{2}$$

$$2Ca^{2+} + OH^{-} \longrightarrow Fe^{3+} + Ca^{2+}_{vac} + OH^{-}_{vac} \tag{3}$$

The non-stoichiometric (Fe+Ca)/P ratio observed from EDXS implies that mechanism (1) and (3) are the most predominate. The reduction in the hydroxyl band intensity from FTIR supports mechanisms (2) and (3). Like Fe^{3+}, Fe^{2+} substitution also occurs through a reaction zone, but Fe^{2+} has an initial pH of 3.0 compared to 1.8 for Fe^{3+}. The less acidic pH of Fe^{2+} reduces the degree of dissolution of HA resulting in a smaller reaction zone for re-precipitation of FeHA. The size of the reaction zone limits the amount of iron incorporated into HA. The smaller reaction zone resulted in less incorporation of Fe^{2+} into HA compared to Fe^{3+}. Compositional analysis from XPS shows a Fe/Ca ratio two times larger than EDXS, which suggests that the substitution of Fe^{2+} adopts a core-shell like structure with more Fe^{2+} near the surface indicating a small reaction zone. Fe^{2+} can easily be oxidized to Fe^{3+} and this can occur in the HA lattice by (4):

$$Fe^{2+} + OH^{-} \longrightarrow Fe^{3+} + O^{2-} \tag{4}$$

This effect would result in the formation a Fe_2O_3 phase, which has not been identified in FeHA within the detection limits of the characterization techniques.

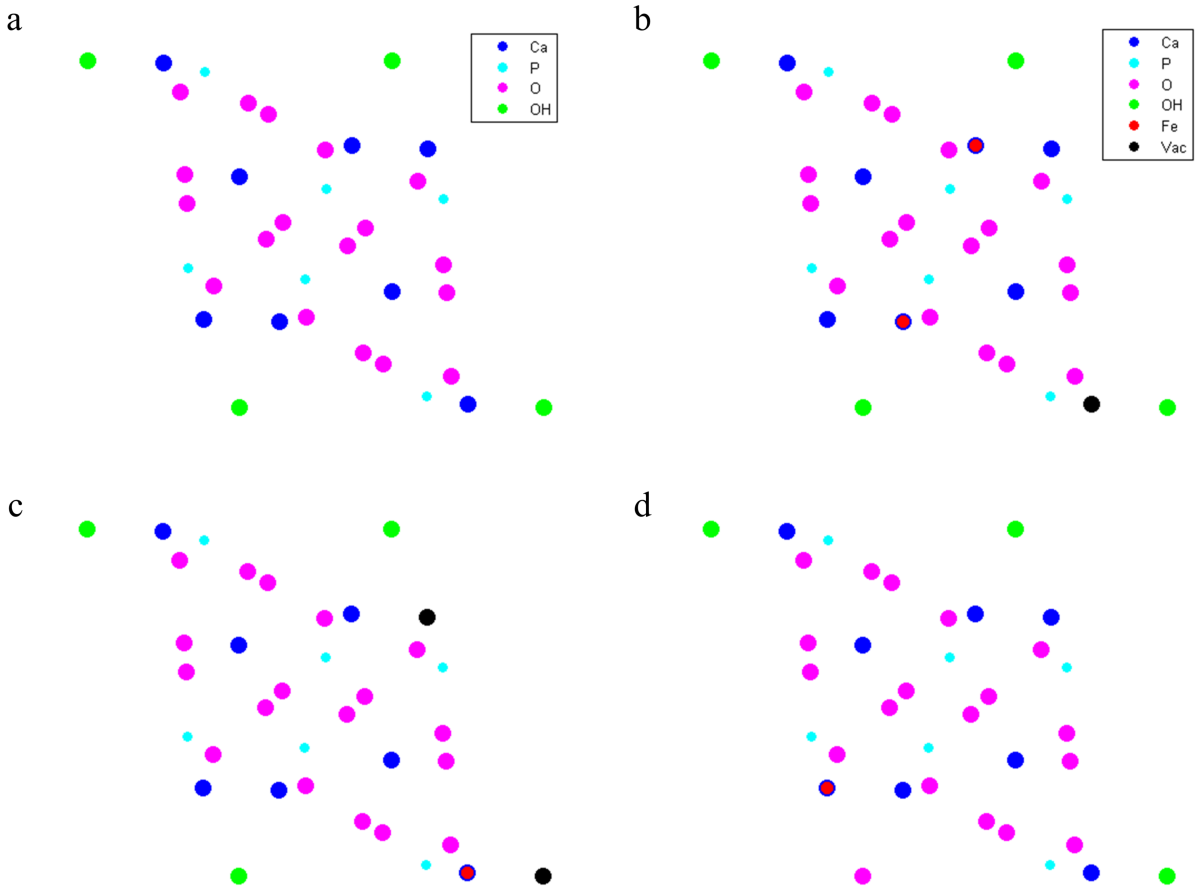

Figure 3.8: The mechanisms of charge compensation are depicted as viewed along the c-axis of the HA unit cell. The HA unit cell is illustrated in (a) and charge compensation mechanisms (1)-(3) in b-d.

The bonding nature of iron and oxygen in FeHA was investigated using XPS. The observed binding energies for Fe^{3+}HA and Fe^{2+}HA are characteristic of $FePO_4$ bonding, which is typically observed between 711-714 eV and depends upon the valence state and coordination environment of iron.[128, 145–147] Comparison of Fe^{2+}HA to Fe^{3+}HA spectrum reveals that the binding energy for Fe^{3+}HA is greater than the binding energy for Fe^{2+}HA; this is to be expected due to the larger positive charge on Fe^{3+} causing it to bind tightly to the phosphate group. Deconvolution of Fe^{2+3+}HA Fe 2p peak reveals binding

energy characteristic of $FePO_4$ bonding. The peak around 710.5 can be attributed to iron in the HA lattice and the peak around 714 e V can be attributed to iron residing on surface site which requires more energy to create a photoelectron.[128] The large value of the full width at half maximum of these peaks does not allow for the distinction from the contribution of Fe^{2+} or Fe^{3+} to the signal.

The main peak in the O 1s spectra around 531.6 eV is attributed to the oxygen in HA where a peak is typically observed between 531.3-531.8 eV (NIST database). The peaks observed around 530.9 and 528.6 eV are attributed to the presence of surface carbonate, which is typically observed around 528.6 or 530.7 eV (NIST database). The observed peak around 533.3 eV is from bridging oxygen of P-O-P bonding.[148] Through the combination of the Fe 2p and O 1s spectra it appears iron has been incorporated into the HA lattice and is bonded to phosphate groups without the presence of iron oxides.

Magnetization measurements revealed that iron substitution modified the magnetic properties of HA (which is diamagnetic) based on the fabrication method.[63] As sown in Figure 3.7, Fe^{3+}HA sample displayed paramagnetism, while Fe^{2+}HA and Fe^{2+3+}HA showed superparamagnetic behavior. As it can be seen in the figure, Fe^{2+3+}HA showed much higher magnetization as compared to Fe^{2+}HA. The superparamagnetism observed in both Fe^{2+}HA and Fe^{2+3+}HA requires the coupling of magnetic spins. Many groups have observed coupling of magnetic spins in iron phosphate materials through observed antiferromagnetic and ferromagnetic transitions.[149, 150] However, the absence of a saturation magnetization in both Fe^{2+}HA and Fe^{2+3+}HA samples implies that the coupling is of short-range order. The magnetic ordering in the present Fe^{2+}HA and Fe^{2+3+}HA is due to super-exchange interactions, the magnetic coupling of two magnetic cations through a non-magnetic anion, from Fe-OH-Fe and Fe-O-P-O-Fe bonding. Panseri *et al.* has also observed superparamagnetism in Fe^{2+3+}HA synthesized through a co-precipitation approach.[60] In their work, the magnetic properties were largely attributed to a secondary iron oxide phase and not the Fe^{2+3+}HA phase. However, it was mentioned that not all of the observed

magnetization could be attributed to the iron oxide phase some magnetization was from Fe^{2+3+}HA. It was also hypothesized that there is some type of magnetic ordering within FeHA.[60] From a structural point of view, an iron ion can occupy either the Ca(I) or Ca(II) site. Theoretical calculations have shown that the Ca(I) site is energetically favorable for Fe^{3+} while occupancy of Ca(II) site is more favorable for Fe^{2+}.[112] The Ca(II)-OH distance is 2.35 Å, which should allow for super-exchange interactions between Fe^{2+} or Fe^{3+} atoms on Ca(II) sites through Fe-OH-Fe bonding. While the Ca(I) site is coordinated with O atoms from the surrounding phosphate groups with Ca(I)-O distances varying from 2.32 to 2.88 Å.[121] Super-exchange interactions for the Ca(I) site could occur through Fe-O-P-O-Fe bonding albeit weaker compared to Ca(II) site. Occupation of Fe^{2+} in the Ca(II) site may explain the superparamagnetic observed for present Fe^{2+}HA and Fe^{2+3+}HA. It should be noted that previous attempts of Fe^{2+}HA fabrication through ion exchange yielded diamagnetic properties.[63]

Changing the particle size and shape of Fe^{2+3+}HA from nanospheres to a needle like morphology with a particle size of 300 nm resulted in a decrease in magnetization at 10 kOe and a transition to paramagnetic behavior. The increase in magnetization with smaller size particles can be attributed to surface effects. As the surface area to volume ratio increases, a larger percent of atoms reside on the surface. In nanomaterials surface effects, such as dangling bonds, change in coordination and surface disorder can cause a change in magnetic behavior when compared to the bulk material, and these effects can increase magnetization to larger value than the bulk magnetization.[130] Similar effects have been observed in iron oxides nanoparticles of varying shapes where spheres have larger magnetization than rods, and the effect of shape on magnetic properties has been related back to surface effects such as missing atoms.[151]

3.4 Conclusion

Iron substituted hydroxyapatite (FeHA) has been fabricated through a facile ion-exchange method without the detection of a secondary impurity phase. The magnetic properties of such samples are found to be dependent upon the oxidation state of iron and particle size. The presence of Fe^{2+} resulted in a superparamagnetic response and an even larger magnetization with a superparamagnetic response was observed when both Fe^{2+} and Fe^{3+} were present. The magnetization of Fe^{3+}HA at 10 kOe is comparable to the magnetization observed in Fe^{2+3+}HA at 10 kOe. We hypothesize that these unique magnetic properties arise from the exchange interactions.

CHAPTER FOUR

A Comparative Study of the Sintering Behavior of Pure and Manganese-Substituted Hydroxyapatite

4.1 Introduction

Hydroxyapatite (HA) is an inorganic constituent of natural bone, which has been extensively studied for its biocompatible and osteo-regenerative properties, serving a scaffold for modern bone graft substitutes.[152–154] As such, HA is widely used for coating orthopedic implants where a strong interface with bone is required and as a bone cement for craniofacial repair.[155, 156] However, HA is brittle in nature and has a slow *in vivo* degradation rate which limits its applications to coatings for orthopedic implants.[153, 157–159] To overcome these issues, HA may be densified through sintering to improve mechanical strength and or through ionic substitutions to enhance bioactivity and mechanical strength.[57–59, 158–163]

The pressing and sintering of HA have been known to improve its ultimate compressive strength and toughness.[57–59, 158–163] Sintering can occur as low as 800 °C with the final sintered density serving as a function of the particle size distribution and agglomeration characteristics of the starting HA powder.[160, 161] For temperatures greater than 700 °C, HA begins to decompose into different phases such as tricalcium phosphate (TCP), calcium oxide (CaO) and water (H_2O).[164] Overall, the presence of TCP in HA scaffolds affects the strength, density, pore size, and degradation rate of HA.[163, 165] TCP degrades faster than HA *in vivo*. Stoichiometric HA has been generally accepted as having a hexagonal $P6_{3/m}$ structure with chemical formula $Ca_{10}(PO_4)_6(OH)_2$ to denote the chemical composition and symmetry composing the crystal unit cell.[164, 166] This apatite structure is flexible, which can be substituted by various elements, such as Na, Mg, K, Sr, Zn, Ba, Cu, Al, Fe,

F, Cl, and carbonate ions.[57, 58, 163] Alteration of the chemical formula of HA through substitutions can alter its bioactivity, which is a similar approach to modify the bioactivity of bioglasses.[159]

In improving the bioactivity of a material it is critical for the material to support cell attachment and the extracellular matrix which contains bioactive factors to induce regeneration.[167] When manganese is substituted into the HA lattice (MnHA) the MnHA has the attractive feature of improving cellular adhesion.[168–172] Manganese (Mn) is an essential trace metal found in all tissues and is required for normal amino acid, lipid, protein, and carbohydrate metabolism.[173, 174] Mn plays a crucial role in cellular signaling, especially in the activation of integrins; receptors that mediate cellular interactions between the extracellular matrix and ligands on cell surfaces.[162, 175] The ligand affinity increases for integrins in the presence of Mn ions, promoting cellular adhesion and possibly having the ability to enhance osteogenesis.[175, 176] The development of new tissue engineered scaffolds that provide mechanical support as well as repair and regeneration of damaged or diseased bone may readily benefit from the introduction of Mn into current HA scaffolds.[153]

MnHA has been previously synthesized through various wet synthesis techniques.[162, 177–186] Many of these studies examine the stability of MnHA through varying the wt% of manganese or the calcination temperature. Mayer *et al.* attempted to incorporate manganese up to 6 wt % via wet synthesis which decomposed at 600 °C into β-TCP.[162, 182, 187] Other attempts to incorporate up to 5 wt % manganese followed by calcination at 800 °C, by Paluszkiewicz *et al.*, resulted in phase purity up to 1 wt % manganese.[183] The phase stability of MnHA at varying manganese wt % is well understood but there are few studies on the effect of manganese substitution and mechanical properties. Ramesh *et al.* produced MnHA through a wet milling technique and observed a decrease in the Vickers hardness of sintered MnHA up to 1 wt % related to density.[188] Herein we report a facile one-step room temperature ion exchange method to synthesize MnHA, as well

as a systematic study of the sintering behavior, microstructural evolution and flexural strength over a series of temperatures to determine the suitability of MnHA for biomedical applications. The relationship between mechanical properties, microstructure and phases helps identify suitable biomedical applications for pure MnHA and its decomposition products.

4.2 Materials and Methods

4.2.1 Materials

The following materials were purchased from Acros Organics: Ammonium phosphate dibasic (99+%), sulfuric acid (95-98%), stearic acid (97%), and potassium bromide (IR grade). Calcium nitrate (99+%), manganese chloride tetrahydrate (99+%), and ammonium hydroxide (29.45%) were purchased from Fisher Scientific.

4.2.2 HA and MnHA synthesis

HA was synthesized via a wet chemical method. An aqueous solution of ammonium phosphate dibasic (80 mM) was added drop-wise to an aqueous calcium nitrate solution (225 mM) at room temperature with the calcium to phosphate ratio maintained at 1.667. Ammonium hydroxide was used to raise the pH of both solutions above 11 prior to mixing the two solutions. Once the two solutions were completely mixed, the temperature of the solution was raised to 95 °C for five hours, and then it was cooled to room temperature and aged for two days under constant stirring. The precipitates were collected via centrifugation and washed 3 times with de-ionized, 2 times with ethanol and vacuumed dried.

MnHA was synthesized through an ion-exchange procedure. A salt solution of $MnCl_2$ was prepared at a concentration of 0.02 M and the pH was adjusted to 2.7 with dilute sulfuric acid. Previously synthesized HA was immersed in the ion-exchange solution at 0.5 g/dL and sonicated for one hour at room temperature with intermittent stirring. The

ion-exchanged HA was collected by centrifugation, washed 3 times with DIW and then vacuumed dried.

The collected precipitates were ground with a mortar and pestle for 30 minutes into a fine powder. The resulting powders were then milled (SPEX 8000 Mixer/Mill) for 10 minutes in a steel canister with alumina mixing balls.

4.2.3 Pellet preparation and sintering

SPEX milled HA and MnHA powders were uniaxially pressed into pellets using a bench top Carver press (Carver Model C). Green bodies were prepared by pressing 0.3 g of milled powder in a 13 mm steel die well lubricated with stearic acid and acetone at a pressure of 150 MPa for 10 s. To improve the final green densities of the green bodies, uniaxially pressed pellets were further compacted through cold isostatic pressing. Uniaxially pressed pellets were vacuumed sealed in latex bags and then cold isostatic pressed at 210 MPa for 30 s.

Pellets were sintered at various temperatures (900 to 1300 °C for HA specimens and 700-1300 °C for MnHA specimens at 100 °C intervals) in air with a soaking time of one hour in a chamber furnace (CM, 1610FL). Specimens were heated at a ramp rate of 15 °C/min to the soaking temperature and then cooled to room temperature at a rate of 15 °C/min. A total of 10 pellets of HA or MnHA were sintered for each temperature point.

4.2.4 Characterization

The milled as-synthesized HA and MnHA powders were examined with a FEI Tecnai T12 S/TEM transmission electron microscope (TEM). Powders were dispersed in ethanol via sonication and deposited onto a copper TEM grid with a carbon film. As-synthesized HA and MnHA, along with sintered HA and MnHA specimens were assessed for phase purity using a Bruker D2 Phaser X-ray diffractometer (XRD) with a copper target. Powder diffraction patterns were acquired over 2-θ ranging from 10-90° with a step size of 0.02°

and a scan rate of 1.25 seconds per step.

Density measurements were performed on the final green bodies and sintered pellets using Ohaus digital balance with an accuracy of 1 mg and a caliper (Mitutoyo) with an accuracy of 0.01 mm. Pellet height and diameter were measured in triplicates for each pellet and the average diameter and height were used to calculate the pellet density.

A Tinius Olsen (150KS model) was used to determine the biaxial flexural strength on sintered 13 mm pellets using a 1000 N load cell at a crosshead speed of 0.01 mm/minute. A pin-on-disc fixture set up was used according to ASTM F 394.[189] The modulus of rupture was calculated by the following equations:

$$S = 0.2387P\frac{X - Y}{d^2} \tag{1}$$

where S is the maximum center tensile stress (MPa) and P is the total load (N) causing fracture,

$$X = (1 + \nu)\ln((\frac{B}{C})^2) + (\frac{1 - \nu}{2})(\frac{B}{C})^2 \tag{2}$$

$$Y = (1 + \nu)[1 + \ln[(\frac{A}{C})^2]] + (1 - \nu)(\frac{A}{C})^2 \tag{3}$$

where ν is Poisson's ration, 0.27, A is the radius of the support circle (mm), B is the radius of the loaded area or pin tip (mm), C is the radius of the specimen and d is the specimen thickness at the point of fracture.

The microstructure of sintered HA and MnHA pellets was examined using a JEOL 6330F field emission scanning electron microscope (FESEM) operating at 5 kV. The fracture surface of sintered HA and MnHA pellets were sputter coated with gold palladium (SEM coating unit E5100, Polaron Instruments Inc.) and used for microstructure analysis.

FESEM was also used to determine the grain size of HA pellets sintered over the temperature range of 1000 to 1300 °C. FESEM was used since the average grain size of certain specimens were less than the resolution limit of optical microscopy. Sintered pellets

were polished to a 1 μm finish and then thermally etched for 30 minutes at 100 °C below the sintering temperature. The average grain size was determined from FESEM images using the line intercept method.

4.3 Results and Discussion

4.3.1 Results

4.3.1.1 Powder Characterization

SPEX milled as-synthesized HA and MnHA powders were characterized with TEM for particle size analysis. Micrographs of HA and MnHA powders are depicted in Figure 4.1. Both powders have morphologies of small rods with an average aspect ratio of 2.6 $\pm$ 0.8 for HA and 2.4 $\pm$ 0.7 for MnHA particles. HA particles (n = 151) have an average length of 35 $\pm$ 11 nm and an average width of 14 $\pm$ 3 nm. Similar to HA, MnHA particles (n = 155) have an average length of 36 $\pm$ 11 nm and a width of 16 $\pm$ 4 nm.

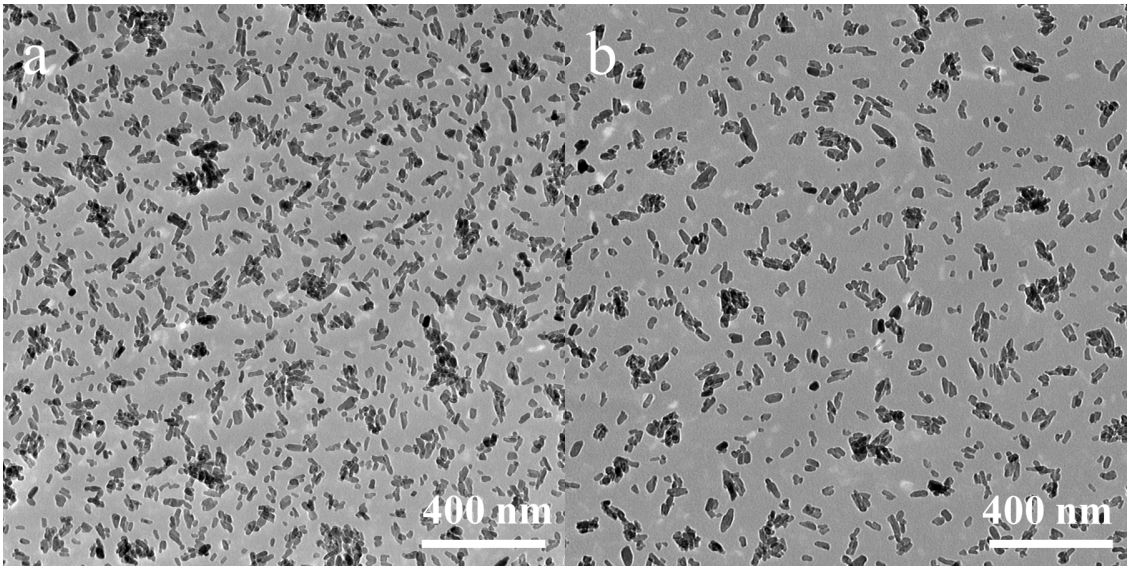

Figure 4.1: TEM micrographs of SPEX milled HA (a) and MnHA powders (b).

4.3.1.2 XRD Characterization

Powder diffraction patterns of the as-synthesized and heat-treated HA are depicted in Figure 4.2. The as-synthesized material displays broad peaks and is identified as HA based on JCPDF 9-432. At 800 °C, the observed peaks become more intense with no extraneous peaks. The indexed peaks for HA continue to increase in intensity up to 1200 °C and decrease at 1300 °C. Decomposition of HA is observed around 900 °C with the emergence of calcium oxide (CaO) and β-tricalcium phosphate (β-TCP) peaks indexed at 27.8° and 29.68° 2θ for β-TCP and 37.4° for CaO. At 1300 °C, HA decomposes further and α-TCP peaks started to emerge.

In comparison to the as-synthesized HA, the as-synthesized MnHA exhibits the same powder diffraction pattern indicative of a pure Mn substituted HA, as shown in Figure 4.3. Unlike HA, MnHA start to decompose to β-TCP and manganese oxide (Mn_3O_4) at a temperature as low as 800 °C, Figure 4.3, with continuous decomposition at higher temperatures. At 1200 °C further decomposition into α-TCP is observed producing a mixture of α-TCP, β-TCP, and Mn_3O_4.

4.3.1.3 Density and Biaxial Flexural Strength

After sintering but prior to density measurements and mechanical testing the physical appearance of the sintered pellets was observed. Sintered HA pellets underwent shrinkage at all temperatures but maintained their white appearance. In contrast, the MnHA pellets not only underwent shrinkage but also resulted in a change in physical appearance which is depicted in Figure 4.4. The initial green pellet is light pink but after sintering at 700 °C turns dark blue. Subsequent sintering temperatures resulted in further color transitions with gray pellets observed at 800 °C, yellow from 900 to 1000 °C, reddish brown at 1100 °C, and black from 1200 to 1300 °C.

The initial green densities, after cold isostatic pressing, and final sintered densities are summarized in Table 1 along with the percent densified. Green bodies of HA have an

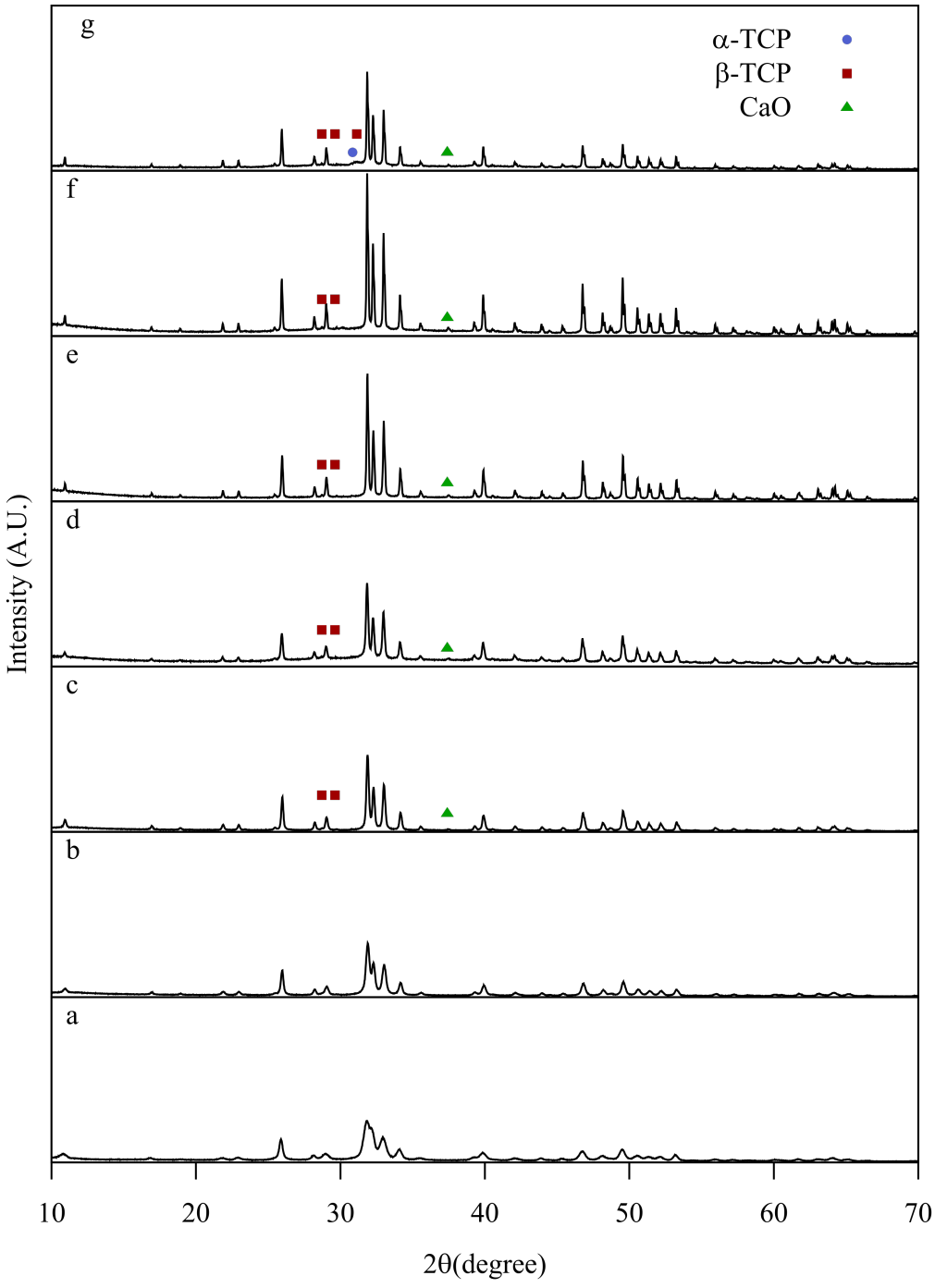

Figure 4.2: Powder XRD pattern of as-synthesized HA (a) and HA heat treated at: 800 °C (b), 900 °C (c), 1000 °C (d), 1100 °C (e), 1200 °C (f), and 1300 °C (g). Non labeled peaks correspond to observed reflections from pure HA.

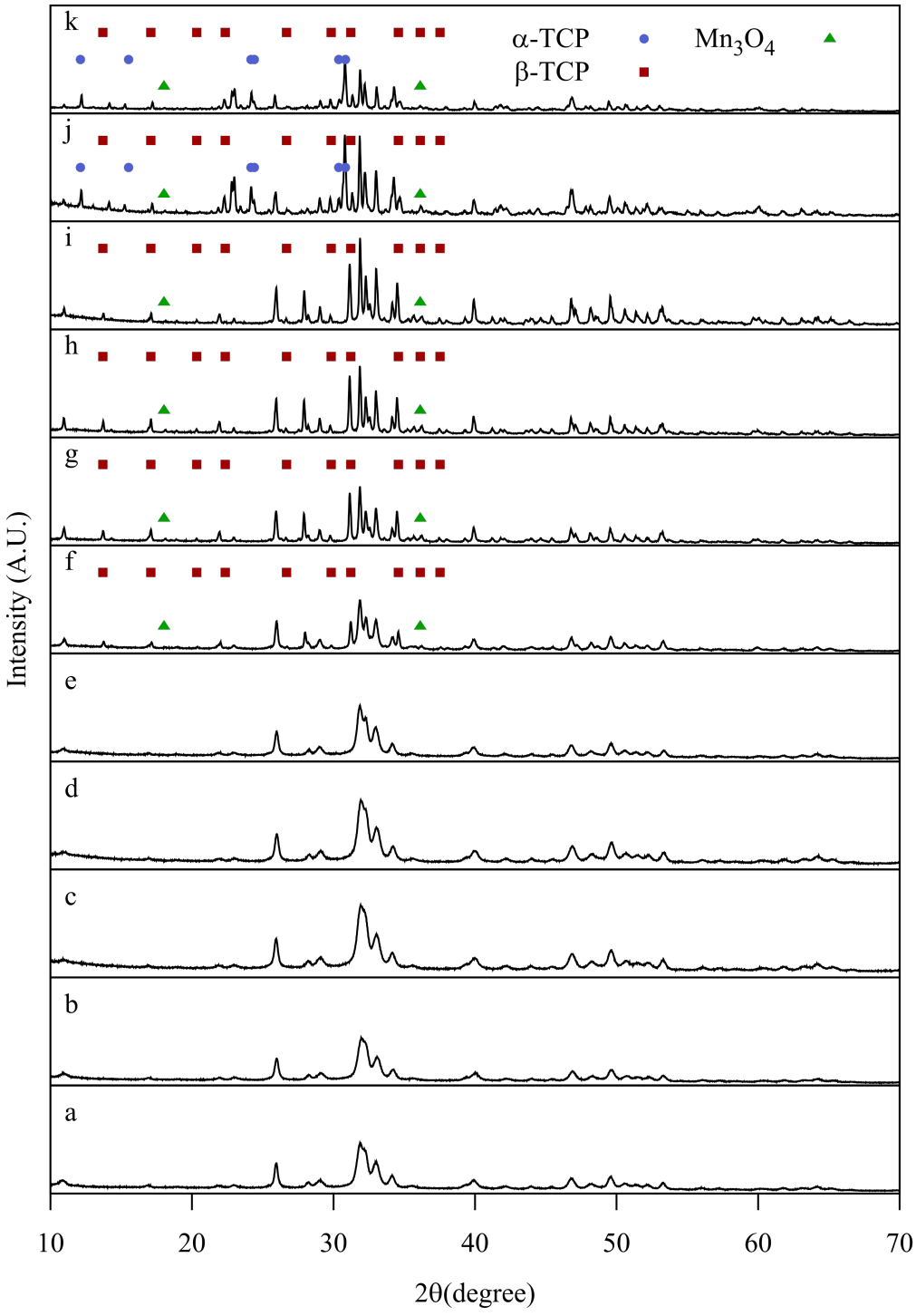

Figure 4.3: Powder XRD pattern of as-synthesized MnHA (a) and MnHA heat-treated at: 400 °C (b), 500 °C (c), 600 °C (d), 700 °C (e), 800 °C (f), 900 °C (g), 1000 °C (h), 1100 °C (i), 1200 °C (j), and 1300 °C (k). Non labeled peaks correspond to observed reflections from pure HA.

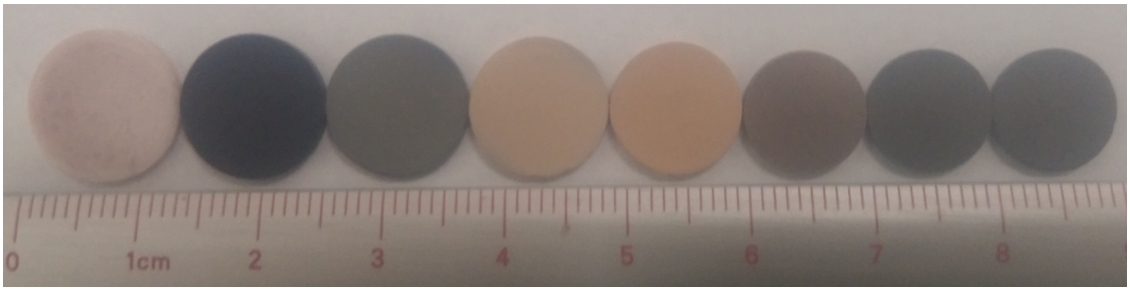

Figure 4.4: Photograph of green and sintered MnHA pellets. From left to right: green MnHA followed by MnHA heat-treated at 700-1300 °C at 100 °C increments. The pellet size also decreases from left to right.

average density around 1.8 g/cm^3, while MnHA have a density around 1.65 g/cm^3. The final densities of HA and MnHA pellets at various soaking temperatures are depicted in Figure 4.5. A one way ANOVA analysis was performed to determine statistically significant differences. There was a statistically significant difference ($p < 0.05$) in HA densities ($p = 5.93e\text{-}16$) and MnHA densities ($p = 5.38e\text{-}35$) over the studied temperature ranges. After sintering at 900°C the HA pellets start to densify followed by increased densification upon sintering at 1000 °C. Within the temperature range of 1000 to 1300 °C, HA pellets continue to densify with increasing temperature until 1300 °C, where a maximum density of 2.99 g/cm^3 is achieved. For MnHA specimens the sintered density continuously increases over the studied temperature range which is reflected in the percent densified. An abrupt increase in density is observed from 900 °C to 1000 °C corresponding to a density of 2.02 and 2.53 g/cm^3, respectively. From 1000 to 1300 °C the density continues to increases and reaches a maximum density of 2.68 g/cm^3 at 1300 °C.

Due to the compressive and bending forces typically exerted on bones, the flexural strength of the sintered pellets were evaluated by a modulus of rupture (M.O.R) test, and the mechanical properties are depicted in Figure 4.6. A one way ANOVA was performed to determine statistically significant differences. There was a statistically significant difference ($p < 0.05$) in M.O.R between HA ($p = 1.33e\text{-}7$) and MnHA ($p = 4.4e\text{-}13$) over the studied temperature ranges. The M.O.R of sintered HA pellets ranges from 23 MPa at 1300 °C to 78

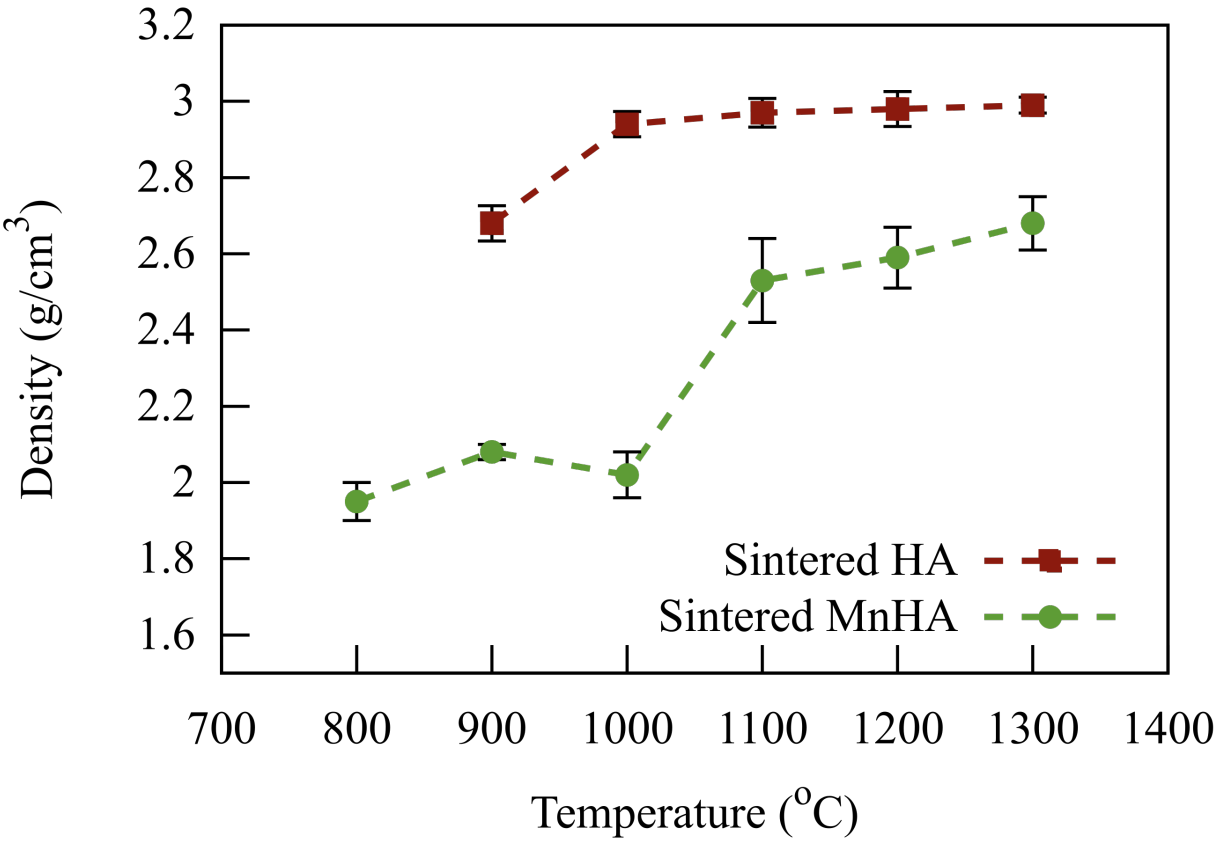

Figure 4.5: Densities of sintered HA and MnHA pellets as a function of temperature. Average densities are plotted ± standard deviation (n ≥ 4).

MPa at 1000 °C. Initially the M.O.R increases from 900 to 1000 °C and then continuously decreases from 1000 to 1300 °C. Unlike HA, the M.O.R. values of the sintered MnHA continuously increase over the temperature range of 800 to 1300 °C ranging from 18 MPa at 800 °C to 64 MPa at 1300 °C. From 800 to 1000 °C there is a small gradual increase in the M.O.R values followed by a rapid increase over the range of 1000 to 1200 °C with a small increase from 1200 to 1300 °C.

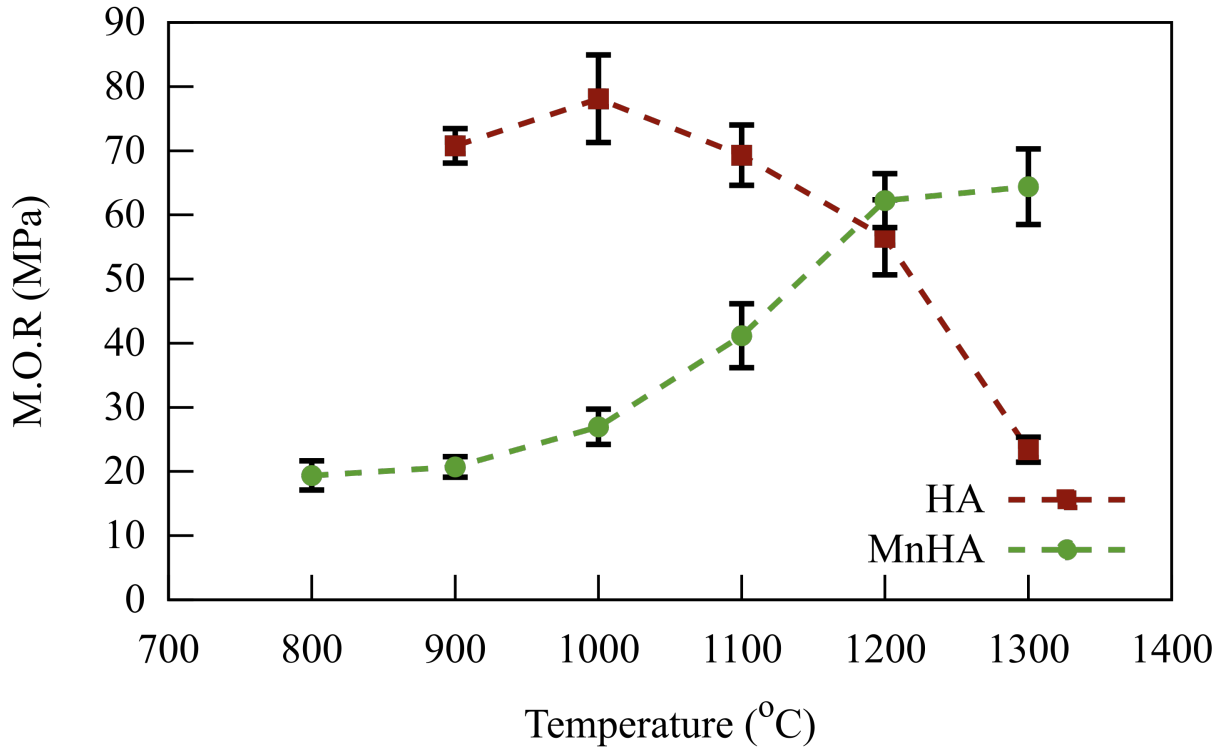

Figure 4.6: Mechanical properties of sintered HA and MnHA pellets as a function of temperature. Average M.O.R values are plotted ± standard error (n ≥ 4).

4.3.1.4 FESEM Characterization

The sintering behavior of heat-treated HA and MnHA specimens was further investigated using FESEM. Fractured surfaces of sintered HA pellets are depicted in Figure 4.7. Specimens heat treated at 900 °C exhibit signs of sintering where the HA particles have fused together and the pores between particles have started to round, but there are still a large number of pores present in specimens. At 1000 °C, the HA specimens have sintered completely with few rounded pores present. At temperatures greater than 1000 °C, grain growth is observed with increasing temperature. Pores remain over the range of 1000 to 1300 °C with a rounded morphology and grow in size with increasing temperature.

Fracture surfaces of heat-treated MnHA pellets are depicted in Figure 4.8. At 700 °C the particles of the green body are identifiable and there is no indication of particles fusing

at this temperature. Unlike HA, MnHA starts to sinter at a temperature as low as 800 °C, where individual particles have started to fuse together, but the overall structure still demonstrates a porous network. The onset of decomposition of MnHA also occurred at 800 °C. The pellets continue to sinter with increasing temperature and the porosity of the sintered body slowly decreases. Significant porosity increase is present at 1200 °C, which is 100 °C lower than that observed in HA sintering.

Since the sintering of HA specimens was complete at 1000 °C, FESEM was used to for grain size analysis over the temperature range from 1000 to 1300 °C. Figure 4.9 shows polished and etched surfaces of HA sintered bodies. The measured grain size was 110 nm, 305 nm, 765 nm, and 1.8 μm from 1000 to 1300 °C. A relationship between the M.O.R and the inverse square root of grain size of sintered HA bodies is depicted in Figure 4.10. The M.O.R increases with decreasing grain size following a linear relationship from 1000 to 1200 °C, which follows the classical Hall-Petch relationship with the following relation

$$M.O.R. = \tau_o + kd^{-1/2} \tag{4}$$

where τ_o and k are material constants and d is the average grain size.

4.3.2 Discussion

The ceramic phase of bone is a poorly crystalline phase of HA with numerous impurities which influence HA's thermal stability, and mechanical and bioactive properties. Pure HA is normally stable until 1350 °C before decomposing into calcium oxide (CaO) and tricalcium phosphate (TCP).[176] In the current study, the decomposition of the as-synthesized HA into CaO and β-TCP started at 900 °C. HA with chemical impurities, such as carbonate, have been shown to degrade at temperatures as low as 800 °C.[190] The synthesis method used in this study was exposed to an ambient atmosphere which resulted in partial carbonation of the precipitated HA, as previously reported.[65] As the temperature increases from 900 to 1200 °C, the HA phase increases in crystallinity with temperature. A transition is observed

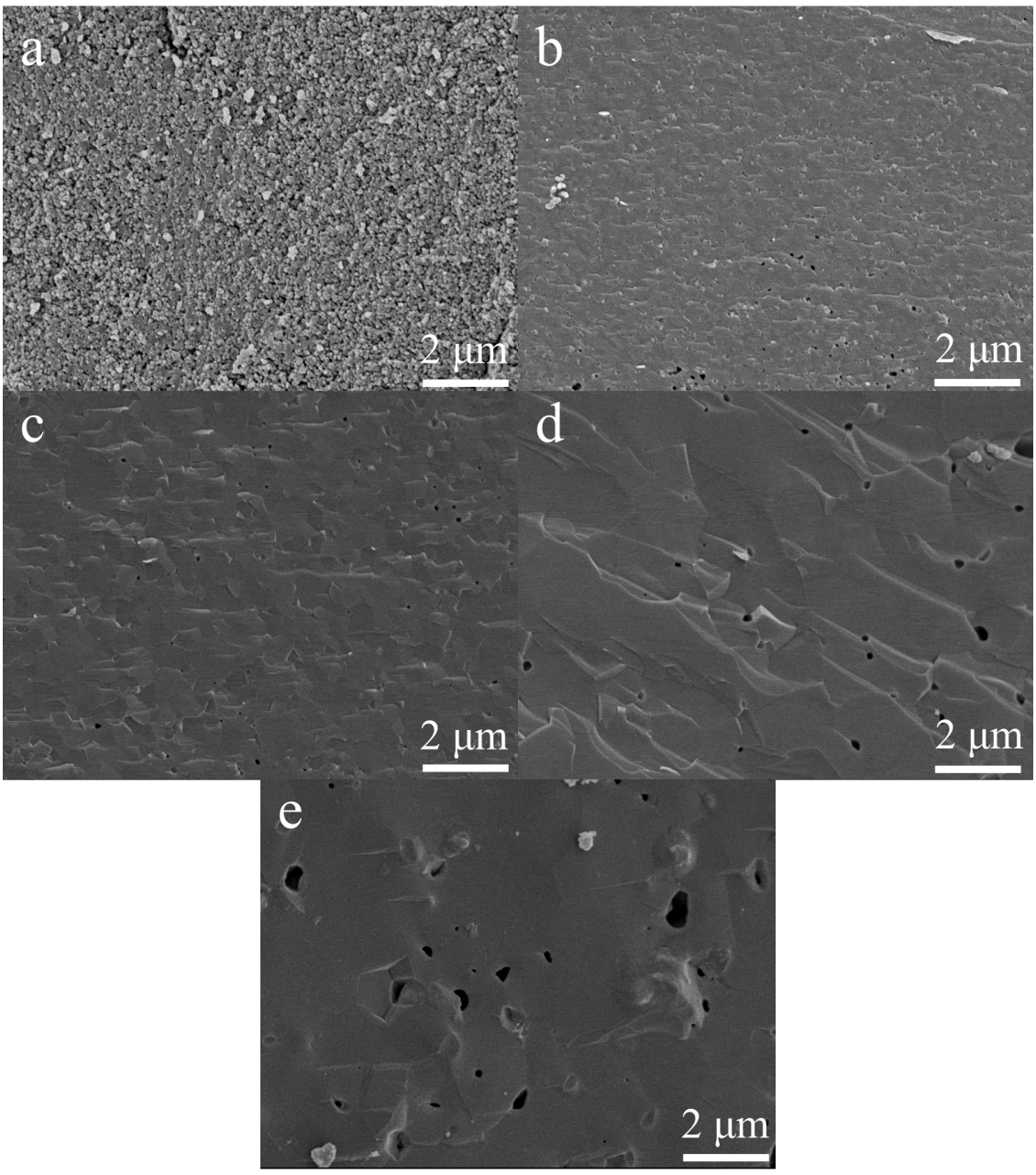

Figure 4.7: Cross sections of sintered HA pellets at 900 °C (a), 1000 °C (b), 1100 °C (c), 1200 °C (d), and 1300 °C (e). Micrographs (a-e) were taken at 10,000X magnification.

at 1300 °C, where the peak intensity of the HA phase decreases in intensity compared to 1200 °C. The relative intensity between the decomposed phases β-TCP and CaO to HA is greater at 1300 °C compared to 1200 °C indicating that the decomposition of the HA phase increases with the sintering temperature.

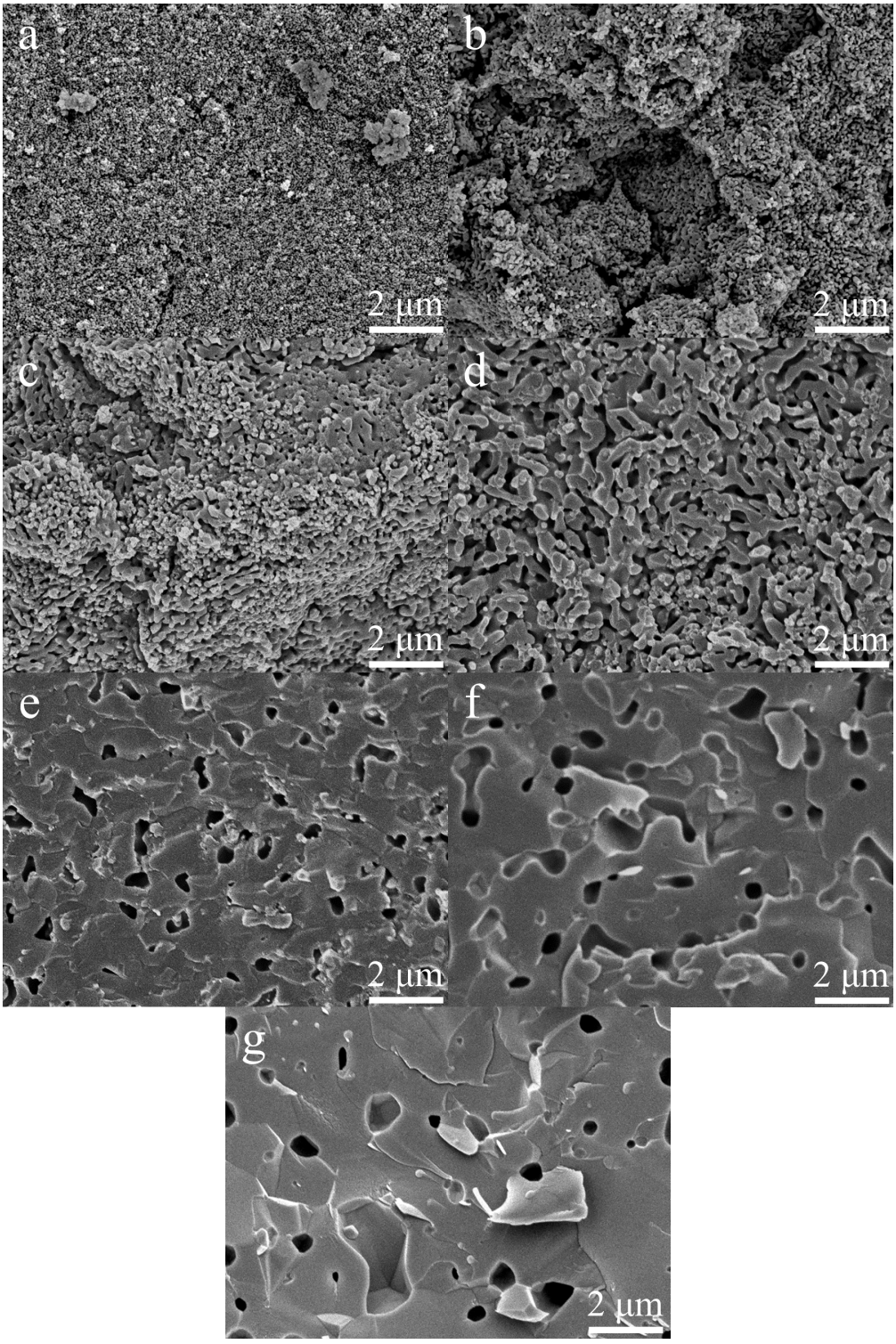

Figure 4.8: Cross sections of sintered MnHA pellets at 700 °C (a), 800 °C (b), 900 °C (c), 1000 °C (d), 1100 °C (e), 1200 °C (f), and 1300 °C (g). Micrographs (a-g) were taken at 10,000X magnification.

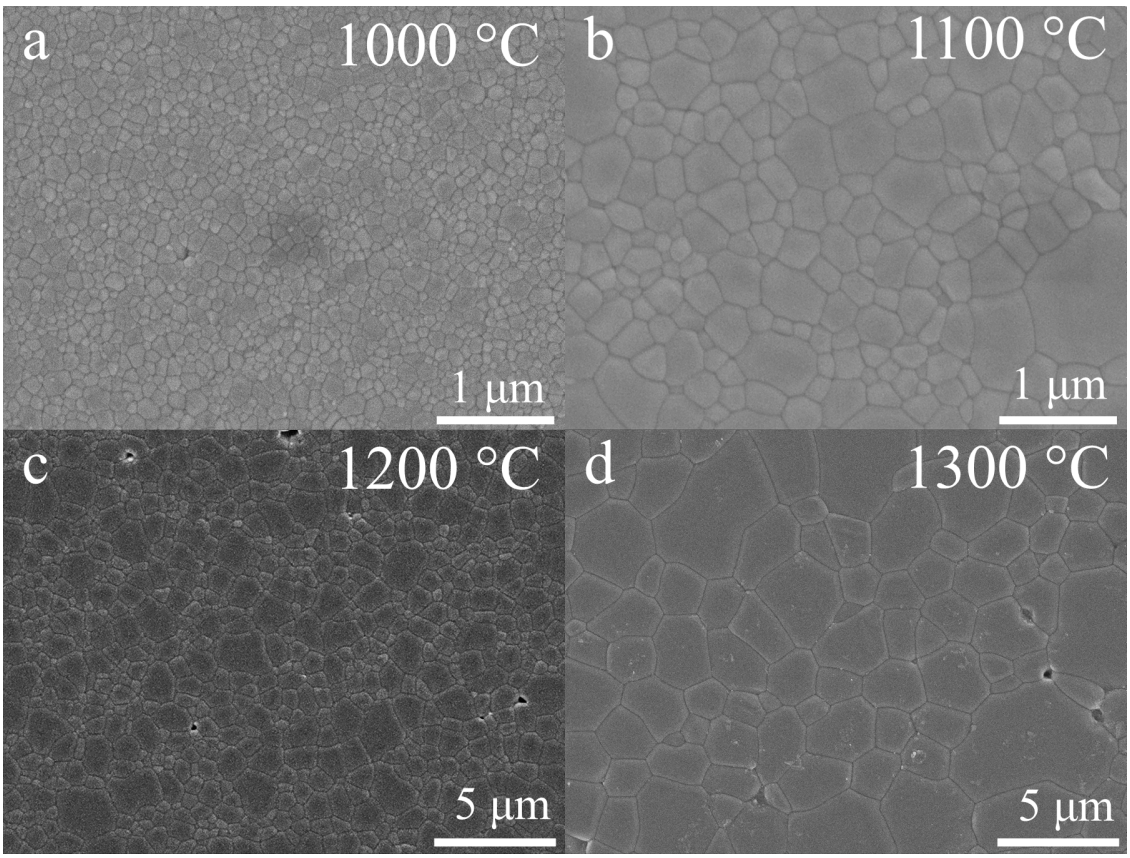

Figure 4.9: FESEM images of the etched surface of HA pellets sintered at 1000 °C (a), 1100 °C (b), 1200 °C (c), and 1300 °C (d). Note the differences in magnification. Micrographs (a) and (b) were taken at 25,000X. Micrographs c and d were taken at 5,000X.

The thermal stability of MnHA was investigated over the range of 400 to 1300 °C. A larger temperature range than HA was selected since manganese oxides have been shown to undergo phase transitions as low as 400 °C.[191] The as-synthesized MnHA powder diffraction pattern matches the observed pattern for the as-synthesized HA indicating successful substitution of Mn into the HA lattice. The phase purity of MnHA is maintained up to 800 °C where significant decomposition into β-TCP and Mn_3O_4 has occurred. Upon further heating, MnHA decomposes into α-TCP, β-TCP, and Mn_3O_4 at 1200 °C; these phases remain present at 1300 °C. The transformation of β-TCP to α-TCP is typically observed around 1125 °C.[192]

The microstructure of HA and MnHA were investigated with FESEM over the tempera-

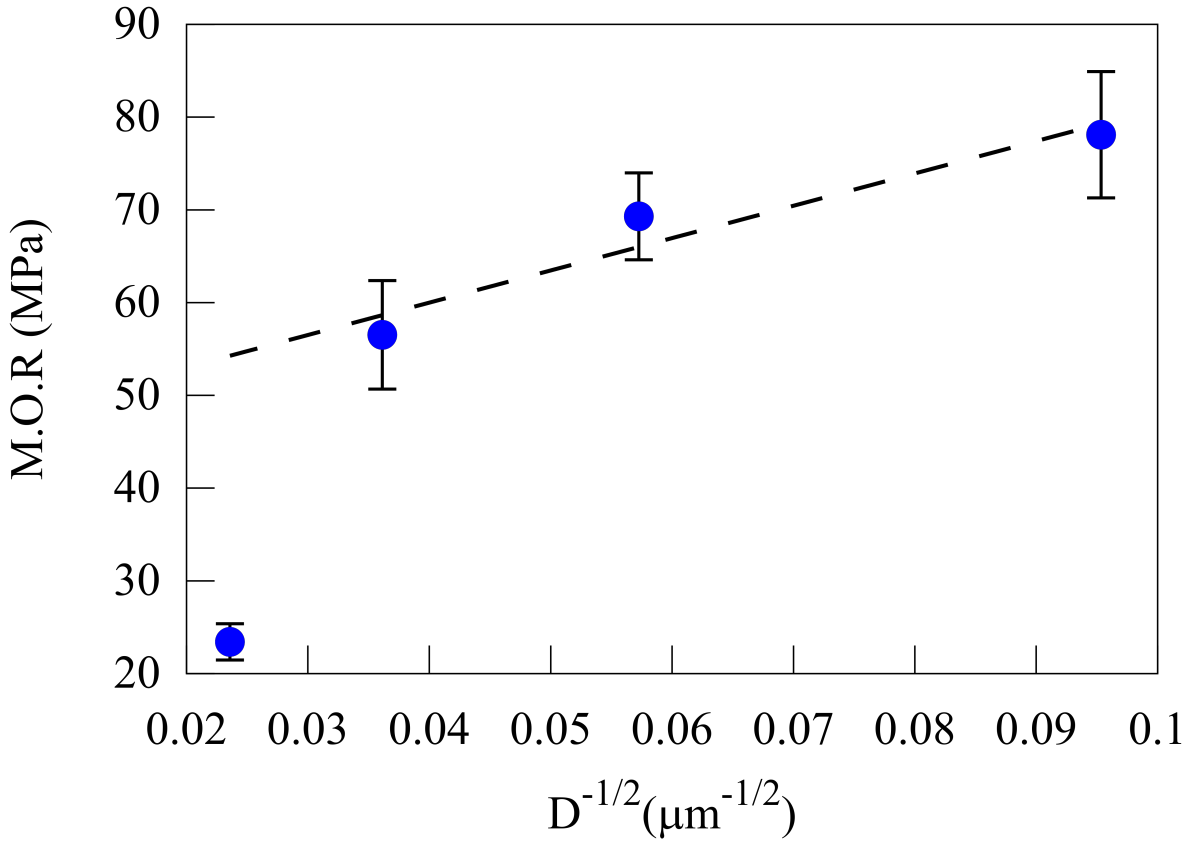

Figure 4.10: Modulus of rupture of HA as a function of the inverse square root of the grain size over the temperature range from 1000 °C to 1300 °C.

ture range studied for mechanical testing. Pure HA normally starts to sinter around 1000 °C [176], but in this study HA was observed to sinter at 900 °C. HA nanorods with similar reported aspect ratios around 2.4 and an average length around 55 nm have been shown to start to sinter as low as 850 °C.[193] The sintering behavior at low temperatures resulted from surface defects such as OH^- vacancies and vacancies created from the release of carbonate groups which lowers the activation energy for surface diffusion.[193] Proceeding from 900 to 1000 °C sintering has completed which is observed in the closure of the pores between particles and an increase in the sintered density which plateaus around 95 % of the theoretical density (3.156 g/cm^3) over the rest of the studied temperature range. The

grain size and pore size increase with the sintering temperature. The grains grow as part of the recrystallization and growth process, while the increase in pore size is a result of the dehydroxylation process of HA. At temperatures exceeding 800 °C HA starts to lose water; during this process pressure builds from water vapor and results in blowhole formation with larger blowholes at higher temperatures.

In the case of MnHA sintering occurred around 800 °C, which coincided with the onset of decomposition. The decomposition of MnHA over the temperature range of 800 to 1000 °C results in a highly porous and interconnected structure which may be attributed to the counteracting processes of both sintering and dehyrdoxylation of HA. The overall porosity slowly decreases over this temperature range. The porosity significantly decreases at 1100 °C, which is reflected in the increase in densification. The pores have become isolated and are lager in size. A similar microstructure was observed at 1200 and 1300 °C, but with less porosity and larger pores. The porosity over the range of 1100 to 1300 °C is related to the decomposition products of HA.

Interestingly over this temperature range the sintered densities increased slowly as seen in the percent densification, and the higher sintered density at 900 °C compared to 1000 °C is attributed to the greater initial green density of 900 °C specimens compared to 1000 °C. The differences between these green densities were a result of variation in batch to batch processing of MnHA where the degree of agglomeration influences the final green density after pressing.

HA and MnHA display different densification and mechanical behavior as a function of temperature. The difference in densification behavior is a result of their discrepancy in thermal stability which influences the microstructure as discussed above. Meanwhile, the mechanical behavior is closely related to the microstructure of the material. HA pellets achieved a maximum M.O.R around 78 MPa, which compares favorably with the values reported in literature of bulk HA which range from 45 to 150 MPa.[158, 194–201] The wide range of reported values results from differences in processing and impurities. Hot

isostatic pressing which results in a more homogenous microstructure and fewer defects was used by Boilet *et al.* and Raynaud *et al.* to achieve flexural strengths in excess of 100 MPa.[200, 201] Kana *et al.* observed that carbonated HA has a lower flexural strength, 45 MPa, when compared to pure HA, 75 MPa.[198] The literature values of flexural strength and the observed maximum M.O.R are also within the range of reported flexural moduli of natural bone which ranges from 35 to 283 MPa.[202]

The M.O.R shown in Figure 4.6 depicts that the M.O.R initially increases for HA peaking at 1000 °C and then decreases over the rest of the temperature range. The initial increase is a result of fewer pores from improved densification from 900 to 1000 °C. After 1000 °C the M.O.R continuously decreases with increasing temperature. Three mechanisms may be attributed to the decreased M.O.R: (1) larger grains, (2) higher porosity, and (3) more decomposition. Improved strength and hardness are observed in ceramics with smaller grains which provide more barriers to crack propagation compared to larger grains. Pores are sites of concentrated stress which reduces the stress need for crack initiation and propagation leading to premature failure. The decomposition process of HA results in pore formation and inhomogeneous microstructure which also reduce the overall strength. The main mechanism resulting in a decrease in the M.O.R is an increase in grain size from 1000 to 1200 °C which follows the classical Hall-Petch relation. A similar Hall-Petch relation was observed in the hardness of nanocrystalline HA sintered over the temperature range of 850 to 1200 °C with grain sizes ranging from 65 to 730 nm by Wang *et al.*[203] At 1300 °C the M.O.R deviates from the Hall-Petch relation as a result of HA decomposition to TCP. The reduction in M.O.R is a result of increased grain size, porosity and pore size.

The increase in the M.O.R as a function of temperature for MnHA is attributed to the sintering behavior of the material, as MnHA densifies the degree of porosity decreases. At sintering temperatures lower than 1100 °C, a highly porous and interconnected microstructure is observed. The large degree of porosity and the interconnectivity of the pores result in a fragile structure. The formation of a denser microstructure with isolated pores

observed from 1100 to 1300 °C results in an increase in the M.O.R attributed to a reduction in porosity. The maximum M.O.R observed for MnHA is around 64 MPa at 1300 °C which is lower than the maximum M.O.R observed for pure HA. Sintering at 1200 °C, the HA phase has almost completely decomposed with α-TCP, β-TCP, and Mn_3O_4 being the dominate phases. The flexural strength of β-TCP is weaker than natural bone and is often detrimental to the mechanical properties of HA when presents as an impurity.[197, 204] The maximum observed M.O.R of MnHA of 64 MPa compares favorably with literature values. Studies on the mechanical properties of metal substituted β-TCP and sintered laminate β-TCP have shown flexural strengths ranging from 20 to 160 MPa.[205, 206] Despite the decomposition of MnHA to TCP, the fast degradation rate of TCP sometimes is a desirable property in many biomedical applications. TCP has been mixed with HA to produce tissue engineering scaffolds with accelerated degradation rate compared to pure HA scaffolds.[207]

4.4 Conclusion

The sintering behavior of pure HA and MnHA was studied for the suitability of MnHA in load bearing applications. The maximum sintered density achieved for was 2.99 and 2.69 g/cm^3 for HA and MnHA, respectively. Decomposition of MnHA into TCP and Mn_3O_4 occurred at 800 °C, while HA pellets started to sinter at 900 °C with partial decomposition to β-TCP and CaO. The maximum M.O.R achieved for HA and MnHA were 78 and 64 MPa, respectively. The low thermal stability of MnHA suggests that a faster dissolution rate *in vivo* than pure HA is expected.

CHAPTER FIVE

In Vitro Evaluation of MnHA, FeHA, and CoHA

5.1 Introduction

Many transition metals are required in trace amounts for normal biological function. Manganese, iron, and cobalt are essential elements but normal dietary intake is generally less than 100 mg/day.[208] When the elemental concentration exceed what is necessary for biological function these elements can be toxic. At high concentrations, toxic effects can arise due to the redox ability which promotes the formation of damaging free radicals such as reactive oxygen species.[208–210] As such, the substitutions of manganese, iron, and cobalt into the HA lattice may alter the biocompatibility.

HA is well-known for its biocompatibility, biodegradation, and ability to accommodate a wide range of substituents. In natural bone a wide range of trace elements are found such as Na, Mg, K, Zn, Ba, Cu, Fe, Mn, F, and carbonate ions.[57, 58, 163] Many substitutions have been shown to alter the biocompatibility and bioactivity of pure HA such as are Mg^{2+}, Sr^{2+}, CO_3^{2-}, and SiO_4^{4-} rendering the substituted HA more biocompatible.[159] When substituted into the HA lattice manganese and iron have both been shown to have a positive influence on osteoblast behavior.[60, 168–172]

In vitro assays are powerful tools that aid in the assessment of a materials toxicity. Even though HA is a well know biocompatible and bioactive biomaterial, changes to its chemical formula may result in a change in biocompatibility. Using commonly used *in vitro* assays the biocompatibility of FeHA, CoHA, and MnHA are assessed and compared to pure HA in this chapter for the assessment of the use of transition metal substituted HA *in vivo*.

5.2 Materials and Methods

5.2.1 Cell Culture

Mouse calvaria 3T3-E1 (MC3T3-E1) cells were used to assess the biocompatibility of MnHA, FeHA, and CoHA powders compared to pure HA. Cells were grown in alpha modified eagles medium (MEM) supplemented with 10 % fetal bovine serum and 1 % penicillin-streptomycin at 37 °C under an atmosphere of 5 % CO_2 with the medium being changed every other day until 90 % confluence.

5.2.2 Cellular proliferation

Cellular proliferation was assessed using either an alamarBlue or 3-(4,5-dimethylthiazol-2-yl)-2,5-diphenyltetrazolium (MTT) assay. In principle, both assays assess the metabolic activity of living cells through the reduction of a dye. Cellular proliferation in the presence of FeHA compared to pure HA was assessed with alamarBlue, and as a cost saving measure cellular proliferation in the presence of MnHA and CoHA were assessed with the MTT assay.

5.2.2.1 Cellular proliferation in the presence of FeHA

Cellular proliferation was assessed at 1, 3 and 7 days via alamarBlue assay. Cells were seeded at a density of 20,000 cells per well in a 24-well plate ($n \geq 3$). Cells were allowed to adhere for four hours, after which the medium was changed to a medium containing FeHA or HA particles dispersed at concentrations of 20 μg/mL or 50 μg/mL. Powders were sterilized by immersion in 70 % ethanol for 30 minutes while under sonication. The powders were collected by centrifugation, rinsed with sterile filtered DIW three times, and re-dispersed in supplemented α-MEM. The medium was changed every other day. At the specified time points, cells were rinsed with a phosphate buffer saline solution and the medium was refreshed with 1 mL of 'powder-free' medium. AlamarBlue was added at $1/10^{th}$ the medium volume and incubated at 37 °C for 4 hours. Aliquots, 200 μL, were

taken from each specimen in triplicate and the absorbance was measured using a plate reader (μquant from Biotek) at 570 and 600 nm. The percent reduction in alamarBlue was calculated by:

$$PercentReduced = (A_{570} - R_o A_{600})100 \quad (1)$$

where R_o is a correction factor, A_{570} and A_{600} are the absorbance values at 570 and 600 nm, respectively. Data was represented as the mean $\pm$ the standard deviation. Statistical significance was tested with a student *t*-test with two tails, and differences were considered significant if $p < 0.05$.

5.2.2.2 Cellular proliferation in the presence of MnHA or CoHA

Cellular proliferation was assessed at 1, 3 and 7 days via MTT assay. Cells were seeded at a density of 20,000 cells per well in a 24-well plate ($n \geq 3$). Cells were allowed to adhere for four hours, after which the medium was changed to a medium containing either MnHA, CoHA, or HA particles dispersed at concentrations of 20 μg/mL or 50 μg/mL. Powders were sterilized the same as FeHA powder was in the previous section. At the specified time points, cells were rinsed with a phosphate buffer saline solution, and the medium was replaced the medium was refreshed with 1 mL of 'powder-free' medium. A 5 mg/mL MTT working solution was added equal to $1/10^{th}$ the medium volume. The treated cells were incubated for 4 hours at 37 °C. The medium was then removed and a solution of 0.04 N HCl in isopropanol was added to dissolve the formed crystals. Aliquots of 200 μL were measured using a plate reader (μquant from Biotek) at 560 nm and the background absorbance was measured at 680 nm. Data was represented as the mean the $\pm$ standard deviation. Statistical significance was tested with a student t-test with two tails, and differences were considered significant if $p < 0.05$.

5.2.3 Cytotoxicity of MnHA, FeHA, and CoHA powders

Lactate dehydrogenase (LDH) is an enzyme bound to the cell membrane and can be used to assess the integrity of the cell membrane. The activity of released LDH was used to quantify the cytotoxicity of MnHA, FeHA, and CoHA powders. LDH activity was evaluated with a LDH assay kit from Thermo Scientific. In brief, cells were seeded at 10,000 cells per well in a 96 well plate ($n \geq 3$) and allotted four hours for attachment. The medium was then removed and replaced with medium containing HA, MnHA, FeHA, or CoHA nanoparticles at 20, 50 or 100 μg/mL. Control cells were treated with 10 μL sterile DIW, which was used to determine the spontaneous LDH release, and 10 μL lysis solution, which was used to determine the maximum LDH release. After 24 hours of incubation, the release of LDH into the medium was determined by adding 50 μL working solution and incubated in the dark at room temperature for 30 min. Then the absorbance of the supernatant was measured at 480 nm, and a background measurement was performed at 680 nm. Data was represented as the mean $\pm$ the standard deviation. Statistical significance was tested with a student *t*-test with two tails, and differences were considered significant if $p < 0.05$.

5.3 Results and Discussion

5.3.1 Results

5.3.1.1 FeHA

Biological evaluations were performed on Fe^{2+3+}HA since it displayed superparamagnetism and had a higher magnetization compared to Fe^{2+}HA. FeHA and HA specimens did not demonstrate any significant difference in supporting cell proliferation at particluate concentrations of 20 and 50 μg/mL, see Figure 5.1 (a). However, cellular proliferation was affected in a dose dependant manner. At a dose of 50 μg/mL, cell proliferation for HA and FeHA particles was significantly less compared to a dose of 20 μg/mL, from day 1 to day 3, respectively. However, this initial effect on proliferation was ameloriated by day 7.

Compared to 20 μg/mL, a 50 μg/mL FeHA dose resulted in a lower degree of proliferation at day 7 than a 50 μg/mL dose HA, but the increase in proliferation from day 3 to day 7 is signigicant. The dose depedenant response was also observed in LDH activity as shown in Figure 5.1 (b). Higher powder concentrations resulted in higher LDH activity, but FeHA was observed to be less toxic compared to HA at the same dose. Cells treated with sterile DIW and a lysis solution were used as controls for LDH activity. The minimum release (min) corresponds to the spontaneous release of LDH from untreated cells, and the maximum release (max) corresponds to the LDH activity where untreated cells were lysed resulting in complete cell death.

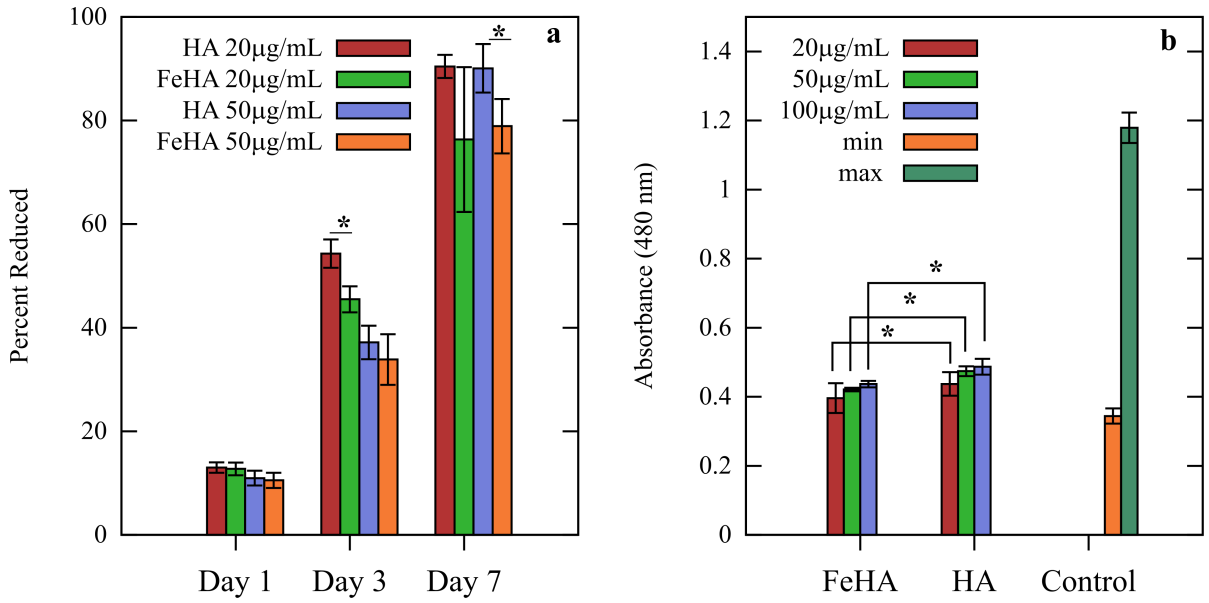

Figure 5.1: Proliferation of MC3T3-E1 cells in the presence of FeHA and pure HA (a). LDH activity from MC3T3-E1 cells treated with FeHA or pure HA compared to the spontaneous (min) and maximum (max) LDH released from untreated MC3T3-E1 cells (b). *$*p < 0.05$*

5.3.1.2 CoHA

The effect of CoHA on cellular proliferation was inhibitive, while HA supported cell proliferation, as seen in Figure 5.2 (a). The HA treated cells proliferated at the same rate

over the course of one week. In contrast the CoHA treated cells did not proliferate from day 1 to 3 with the optical density (O.D.) remaining the same while the cell number decreased from day 3 to 7 with a decrease in O.D..

The LDH assay results are presented in Figure 5.2 (b). There is no statistical difference (as determined by a 2-tailed *t*-test) between the spontaneous release of LDH in cells treated with medium alone and those treated with HA or CoHA.

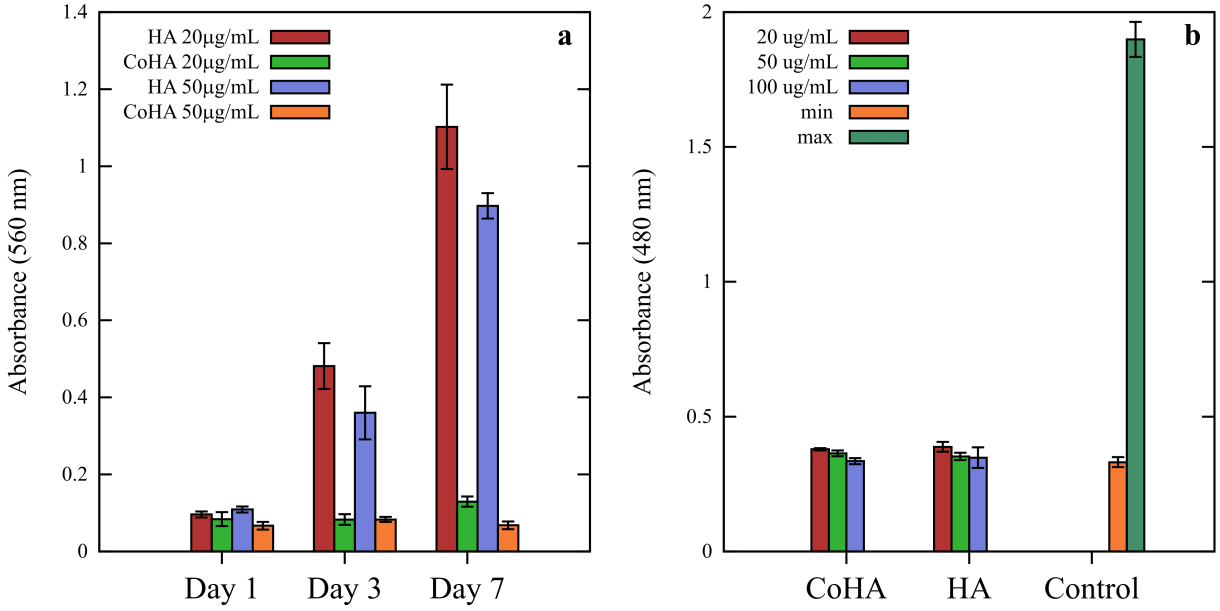

Figure 5.2: Proliferation of MC3T3-E1 cells in the presence of CoHA and pure HA (a). LDH activity from MC3T3-E1 cells treated with CoHA or pure HA compared to the spontaneous (min) and maximum (max) LDH released from untreated MC3T3-E1 cells (b).

5.3.1.3 MnHA

Both HA and MnHA supported cell proliferation as seen in Figure 5.3 (a) and there were no statistically significant differences between HA and MnHA treated cells of equal concentrations. Proliferation was affected in a dose dependent manner. The 50 μg/mL dose of HA and MnHA resulted in a statistically significant difference at day 3 compared to cells treated with 20 μg/mL HA. At day 7 where there is a statistically significant difference

between cells treated with 20 μg/mL and 50 μg/mL HA or MnHA. Overall, no statistically significant differences were observed when cells were treated with the same dose of HA or MnHA.

The LDH assay results are presented in Figure 5.3 (b). There is no statistically significant difference between the spontaneous release of LDH in cells treated in medium alone and those treated with HA particles or MnHA at 20 μg/mL. Interestingly a dose of 50 and 100 μg/mL MnHA resulted in a decrease in LDH activity that was a statistically significant difference compared to the spontaneous LDH release control.

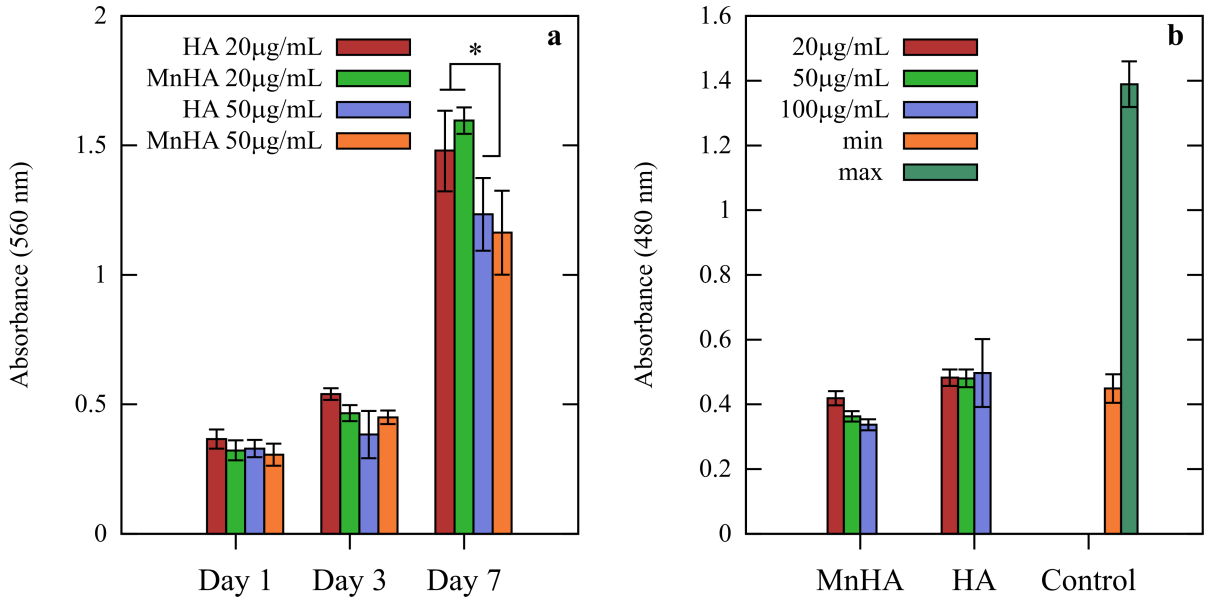

Figure 5.3: Proliferation of MC3T3-E1 cells in the presence of MnHA and pure HA (a). LDH activity from MC3T3-E1 cells treated with MnHA or pure HA compared to the spontaneous (min) and maximum (max) LDH released from untreated MC3T3-E1 cells (b). *$*p < 0.05$*

5.3.2 Discussion

5.3.2.1 FeHA

Further testing of Fe^{2+3+}HA was assessed *in vitro* due to the lucrative superparamagnetic property and larger magnetization than Fe^{2+}HA. Proliferation was assessed with

the alamarBlue assay. The active reagent in alamarBlue is reazurin, which is reduced by metabolically active cells resulting in a change in color from blue to red. Increased reduction in alamarBlue can be related to an increase in cell number. The proliferation of MC3T3-E1 cells showed no cytotoxicity when Fe^{2+3+}HA and HA were administered at the same dosage (20 μg/mL). A higher administered dosage (50 μg/mL) of Fe^{2+3+}HA showed an initial inhibition of cellular proliferation at day 3 and negligible inhibition by day 7.

A cytotoxicity assay was also performed to assess the damage to the cell membrane. LDH is a membrane bound protein that is released when the cell membrane is damaged. The amount of LDH released is representative of the toxicity of a material. A dose dependent response was observed similar to that in the proliferation assay. Still, FeHA was observed to be less cytotoxic than HA at the same dose. The observed toxicity of HA is not atypical for *in vitro* studies despite its *in vivo* compatibility. Many factors contribute to toxicity including particle size and shape, surface charge and chemical composition.[211–213] The toxicity of HA nanoparticles can be attributed to the release of Ca^{2+} disrupting the intracellular Ca^{2+} homeostasis as observed by Motskin *et al.*[211] The use of *in vitro* characterization is a valuable tool for screening the compatibility of biomaterials but the response is not indicative of the *in vivo* performance. As the case for HA, it is a widely accepted biomaterial with excellent *in vivo* performances, but its *in vitro* performances does not always reflect its *in vivo* biocompatability.[214] This may be true with FeHA too, future studies to examine the *in vivo* performance of FeHA will be conducted to confirm its biocompatibility as an implantable material.

5.3.2.2 CoHA

Prior to utilization in biomedical applications, the biocompatibility of CoHA needs to be evaluated. While the results from the proliferation experiment may initially suggest that CoHA is not biocompatible, the findings from the LDH assay, Figure 5.2 (b), suggest differently. The discrepancy between these results suggests that either a catalytic reaction

occurs between CoHA and the cell culture medium or the release of cobalt ions inhibits cell proliferation. The cell culture studies presented in this chapter are also limited in that a single cell line was used. Various cell lines may react differently to differing culture conditions. For example, Wu *et al.* established that low amounts of cobalt incorporation into a scaffold resulted in no cytotoxicity in human bone marrow stromal cells (BMSCs). Additionally, cobalt ion release from the scaffold induced VEGF protein secretion, HIF-1α expression, and bone-related gene expression in BMSCs, indicating that while cobalt ions result in a response that mimics hypoxic conditions, they did not induce toxicity or cell death.[215] Additionally, *in vitro* cell culture conditions are simple and static, as compared to *in vivo* conditions. *In vivo* response to cobalt release from CoHA may differ from that seen *in vitro*. The cell culture results obtained in this chapter are not sufficient to draw any strong conclusions, and the CoHA material needs to be further investigated for its biocompatibility.

5.3.2.3 MnHA

Overall, the results from proliferation suggest that MnHA is biocompatible, while the results from the LDH assay are inconclusive. The proliferation results suggest that MnHA does not affect the metabolic behavior of the cells as observed in the inhibitive effect of CoHA and is as biocompatible as pure HA. The increase in MnHA concentration resulted in a decrease in LDH activity. This may result from an interaction between MnHA particles and LDH or released manganese ions and LDH. Han *et al.* studied the effect of copper, silver, and titanium dioxide nanoparticles on their potential to inactivate LDH and observed copper nanoparticles interfered with LDH due to the interaction between LDH and copper ions as a result of copper dissolution.[216] Titanium dioxide particles adsorbed LDH but did not inactivate the enzyme.[216] In the case of titanium dioxide the LDH activity was observed to increase with nanoparticle concentration up to a critical concentration after which LDH activity decreased, which was attributed to adsorption of LDH to titanium

dioxide nanoparticles.[216] Interaction between particles and commonly used viability assays can make drawing strong conclusions on the toxicity of particles difficult even at low particle concentrations.[217] Overall, results from the MTT assay suggest that MnHA does not affect the metabolic activity of the cell and comparable to pure HA, while the results from LDH assay are inconclusive. While *in vitro* assays are good indicators of a materials biocompatibility it is not always indicative of *in vivo* performance. As with FeHA, future *in vivo* studies should be performed to confirm its biocompatibility as an implantable material.

5.4 Conclusion

The biocompatibility of FeHA, CoHA, and MnHA were assessed and compared to pure HA using a proliferation assay and cytotoxicity assay. The substitution of iron and manganese did not significantly affect cellular proliferation, while the substitution of cobalt resulted in inhibited cellular proliferation. Assessment of LDH activity indicate that FeHA and CoHA do not damage the integrity of the cell membrane and the cytotoxicity is comparable to pure HA, while results from MnHA are inconclusive due to interference between MnHA and LDH. These effects are due to either the release of ions from the powders or particle interactions with the cells. The inhibitive effects of CoHA on proliferation is most likely due to the release of cobalt ions, which can create a hypoxic environment through the stabilization of HIF-1α. This effect is not seen with iron or manganese ions. The release of ions and/or particle interactions may inhibit LDH activity, which was observed in MnHA but not FeHA or CoHA. Overall, iron- and manganese-substituted HA powders demonstrated good biocompatibility, which makes these powders suitable for potential magnetic applications and other biomaterial applications such as bone void filler. Cobalt-substituted HA is suitable for potential magnetic applications where material can be removed rapidly from the body. Further *in vivo* testing should be performed for all substituted HA powders.

CHAPTER SIX

Mineralization of Type I Collagen with Iron Oxide for the Synthesis of Magnetic Nanoworms

6.1 Introduction

In regards to tumor therapy applications, the particle properties, such as size and shape, are important factors.[70–73] In both passive and targeted delivery applications, the blood circulation time is an important factor in particle accumulation at the tumor site. There is increasing evidence that non-spherical/anisotropic particles are less readily taken up by macrophages, resulting in a slower clearance rate of the material, thereby prolonging circulation.[72, 73] Non-spherical shapes also demonstrate improved targeting efficiency, since the oblong shapes have more surface area compared to spherical particles more binding events between the targeting ligand and target site can occur.[73] While in circulation, non-spherical particles exhibit more lateral drift compared to spherical particles, which follow streamlines, resulting in an increased likely hood of accumulating at the tumor site.[73] Recently, the semi-flexible filomicelles as delivery vehicles have been shown to have increased circulation time and accumulation in tumors compared to spherical micelles.[76–78]

The rigid nature of the previously synthesized HA particles may result in short blood circulation times. The main organic component of bone is type I collagen that is a long and flexible filamentous protein. Biomimetic techniques have been successful at inducing mineralization inside the gap zone of collagen fibers (namely, intrafibrillar mineralization) with either calcium phosphate or silica.[218–220] The mineralization of a magnetic phase within the gap zone of collagen may yield a semi-flexible and magnetic material suitable for tumor therapy applications.

Typical biomineralization approaches utilize macromolecules with charged functional groups, such as carboxylates and amines.[218, 219] In the case of intrafibrillar mineralization with calcium phosphate, a negatively charged macromolecule mimicking acidic proteins is required to prevent premature precipitation of calcium phosphate while supporting the deposition of calcium phosphate within the collagen fibers.[218] Intrafibrillar mineralization with silica requires positively charged functional groups to attract negatively charged silica.[219]

Iron oxides are another class of materials that are classified as a biomineral. Excess iron ions within the body are stored as ferrihydrite within the globular protein ferritin.[221] The accumulation and release of iron within ferritin is mediated through interactions with the amino acids glutamate and aspartate. These amino acids have a carboxylate functional group that interacts with iron ions through electrostatic interactions. The structure of ferritin and its interactions with iron ions have been used to produce magnetic iron oxides and manganese oxide nanoparticles under basic and reducing conditions.[222, 223]

Utilizing the principles of biomineralization, collagen fibers are templated with macromolecules with either carboxylate or amine functional groups and incubated in an iron solution. Mineralization is induced by raising the pH of solution to induce precipitation of iron oxide within collagen.

6.2 Materials and Methods

6.2.1 Materials

Type I collagen was extracted from rat tails, solubilized, and purified based on a protocol reported by Rajan *et al.*[224] Poly-aspartic acid (Mw = 2000-11000 Da) and polyallylamine hydrochloride (Mw = 15000 Da) were purchased from Sigma-Aldrich. A 2 % aqueous solution of osmium tetroxide solution was purchased from Electron Microscopy Sciences. The following chemicals were purchased from Acros Organics: iron chloride tetrahydrate (99+%),

iron chloride hexahydrate (97+%), and 1-ethyl-3-(3-dimethylaminopropyl)carbodiimide hydrochloride (98 +%). Ammonium hydroxide (29.45 %) was purchased from Fisher Scientific.

6.2.2 Methods

6.2.2.1 Functionalization of collagen fibers

A two-step approach was employed to mineralize collagen fibers with iron oxide. First, collagen fibers were formed by mixing acid solubilized type I collagen (3 mg/mL) with a 0.2 M phosphate buffer (pH = 7.4) at a 1:1 (v:v) ratio for one hour. Collagen fibers were collected via centrifugation and washed three times with de-ionized water (DIW). Collagen fibers were incubated in a solution of 500 μg/mL polyallylamine hydrochloride (PAH) or poly-aspartic acid (PASP) at 37 °C for one hour. 1-ethyl-3-(3-dimethylaminopropyl)carbodiimide hydrochloride (EDC) was added at 0.02 g/mL to cross-link PAH or PASP to the collagen fibers. The solution was incubated at 4 °C overnight to allow for complete cross-linking. As a control, collagen fibers were cross-linked with EDC in the absence of PAH or PASP prior to mineralization.

For transmission electron microscopy (TEM) characterization, collagen fibers were grown on gold TEM grids by floating the TEM grid on top of the polymerizing collagen solution. Functionalization with PASP or PAH was performed as described above by immersing the TEM grid with collagen fibers in the respective solutions.

6.2.2.2 Mineralization of functionalizated collagen fibers

Functionalized collagen fibers (PAH or PASP templated) were immersed into a 40 mM solution of iron chloride with $FeCl_2$:$FeCl_3$ ratio of 2:1 at 37 °C under the protection of a nitrogen atmosphere. The fibers are incubated in the iron solution for one hour after which the pH is rapidly adjusted with concentrated ammonium hydroxide to a pH > 10. The fibers

are mineralized for one hour, collected, and rinsed through a combination of sonication and magnetic decantation.

After observing that PASP functionalization promoted mineralization, the $FeCl_2$:$FeCl_3$ ratio was varied from 1:0, 1:2, 1:1, and 2:1 using a 4 mM iron solution. The fibers were incubated in the iron solution at 37 °C with the protection of a nitrogen atmosphere for 1 hour. The pH was rapidly adjusted to a pH > 10, and the fibers were allowed to mineralize overnight. Fibers were collected and rinsed as described above.

6.2.2.3 Characterization

Mineralized collagen fibers were observed using TEM (JEOL JEM-2010) at an accelerating voltage of 80 kV. For the ideal mineralized collagen fibers characterized using attenuated total reflection-Fourier transform infrared spectroscopy (ATR-FTIR) and X-ray diffraction. A Nicolet Magna 560 FT-IR spectrometer with an ATR setup was used to collect infrared spectrum in the range of 4000-400 cm^{-1} at a 4 cm^{-1} resolution with 32 scans. A Bruker D2 Phaser X-ray diffractometer (XRD) with a copper target was used to acquire XRD patterns over 2-θ ranging from 10-70° with a step size of 0.02° and a scan rate of 1.25 seconds per step.

6.2.2.4 Synthesis of single collagen fibers

Single collagen fibers were synthesized by controlling the kinetics of collagen polymerization. Collagen polymerization was initiated by mixing a phosphate buffer (pH = 7.4) with acid soluble type I collagen at 1:1 (v:v) ratio on top of a TEM grid to induce self-assembly of collagen fibers on the TEM grid. The polymerization process was simultaneously monitored by measuring the turbidity of the polymerizing collagen solution at 313 nm using a microplate reader (μquant from Biotek). At selected time point, the polymerizing collagen solution was rinsed away with DIW. Collagen fibers were stained with osmium tetroxide for 30 minutes prior to TEM characterization.

6.3 Results and Discussion

6.3.1 Results

Initially collagen fibers templated with PASP, PAH, or cross-linked fibers were mineralized with a 40 mM iron chloride solution. After mineralization, the resultant fibers were black in appearance and were attracted to a permanent magnet. Figure 6.1 depicts the mineralized fibers for each of the aforementioned conditions. When the collagen fibers are templated with PASP, Figure 6.1 (a), the characteristic d-banding pattern of collagen is observed indicating successful mineralization within the gap zone. In contrast, the cross-linked collagen fibers, Figure 6.1 (b) display minor d-banding with minerals on the surface, while the PAH templated collagen fibers did not display any visible signs of d-banding only minerals deposited on the surface.

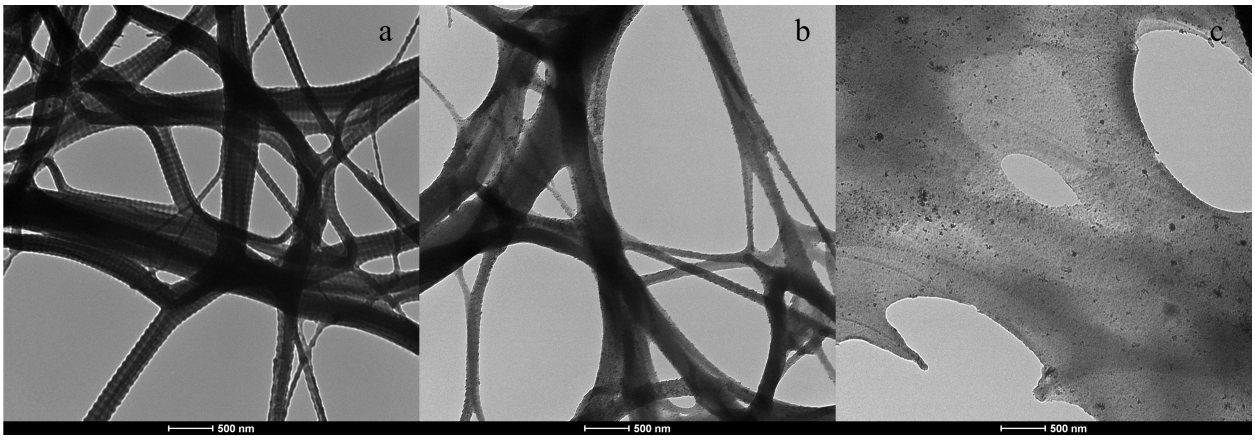

Figure 6.1: Iron oxide mineralization of collagen fibers. Fibers templated with PASP (a), control fibers cross-linked with EDC (b), and fibers templated with PAH (c).

The most prominent d-banding was observed in collagen fibers templated with PASP, so further investigation was conducted on the effect of the Fe^{2+}:Fe^{3+} ratio, which influences the pathway of iron oxide formation, on PASP-templated collagen fibers (Figure 6.2). Iron oxide particles were formed on the surface and within the gap zone of collagen fibers. The observed d-banding pattern in the collagen fibers is the most pronounced when the

Fe^{2+}:Fe^{3+} ratio was 2:1 or 1:1, suggesting the formation of iron oxide inside the gap zone of collagen fibers. When Fe^{2+}:Fe^{3+} ratio is 1:0, light d-banding is observed but large crystals are present on the surface of the fibers. For the case where Fe^{3+} is present and the concentration of Fe^{3+} is less than that of Fe^{2+}, the characteristic d-banding pattern is more evident with fewer large precipitates on the surface of the collagen fibers. As the concentration of Fe^{3+} increases, more small particles are present on the surface of collagen fibers.

Further characterization was performed on collagen fibers templated with PASP and mineralized with an iron Fe^{2+}:Fe^{3+} ratio of 2:1. The FTIR spectra and XRD pattern are depicted in Figure 6.3 and Figure 6.4, respectively. The FTIR spectra obtained from pure collagen and iron oxide mineralized collagen fibers display peaks around 1630 cm^{-1}, 1540 cm^{-1}, and 1200 cm^{-1}. These peaks arise from the different stretching and deformation modes of the amide bonds in collagen. The amide I peak around 1630 cm^{-1} results from C = O stretching; the amide II peak around 1540 cm^{-1} is due to N-H deformation. The amide III peak around 1200 cm^{-1} arises from C-N stretching. Also, for both pure collagen and mineralized collagen fibers peaks are observed in the 3000 - 2800 cm^{-1} range and a broad peak around 3300 cm^{-1} that arise from C-H and O-H stretches, respectively. Unlike the pure collagen spectra, collagen fibers mineralized with iron oxide display a small peak around 560 cm^{-1} which corresponds to Fe - O stretching. The XRD pattern displays broad peaks around 20° and 30° due to amorphous scattering of X-rays from collagen. Peaks are observed around 35.4°, 56.9°, and 62.5° which correspond to the (311), (511), and (440) reflections of Fe_3O_4 or γ-Fe_2O_3 respectively. The distinction between these two phases is difficult, since γ-Fe_2O_3 is Fe_3O_4 but with vacancies at the Fe^{2+} site. The similarity in crystal structure results in nearly identical XRD patterns for these materials.

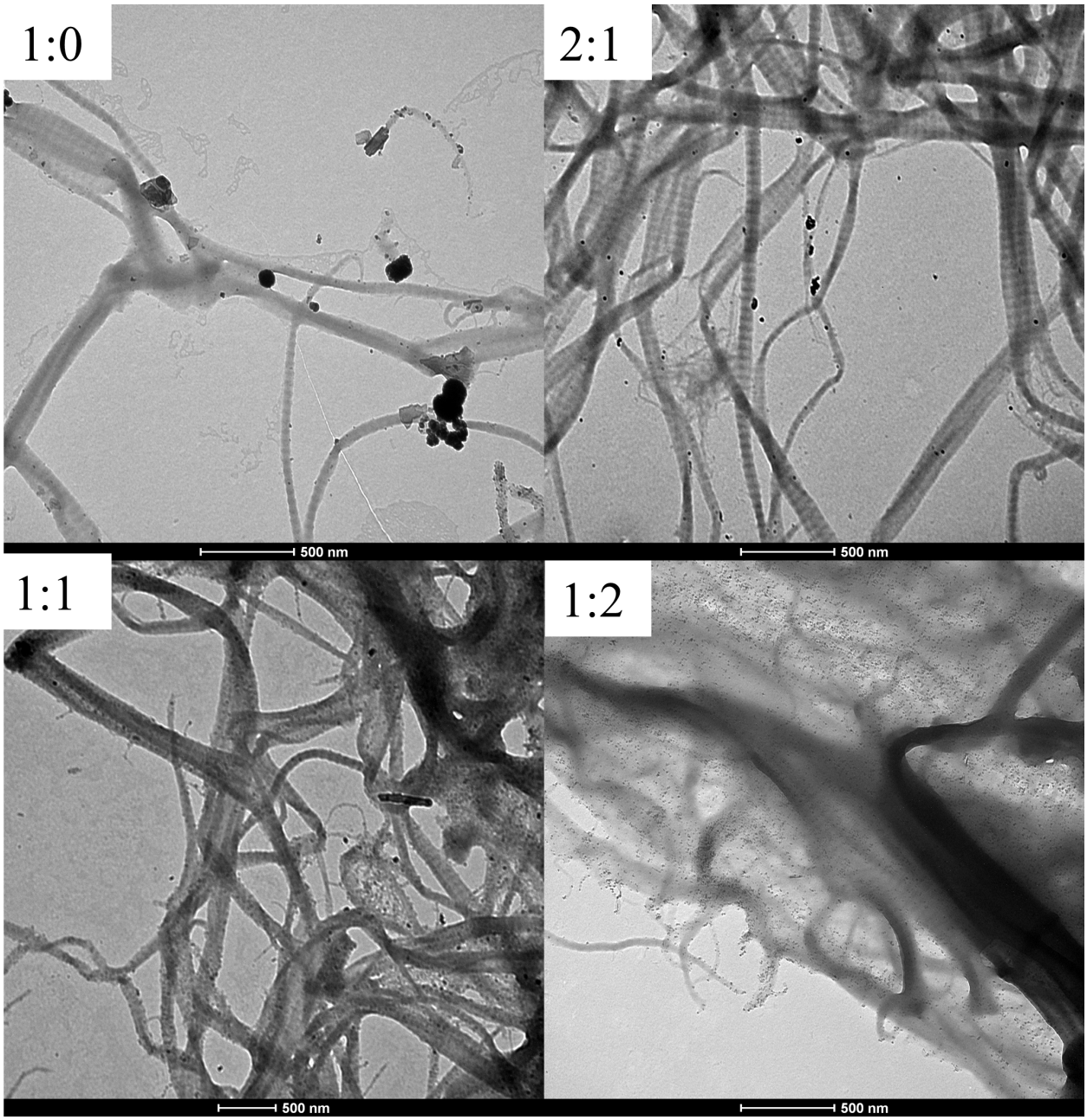

Figure 6.2: Poly-aspartic acid functionalized collagen fibers mineralized using 4 mM iron chloride solution with Fe^{2+}:Fe^{3+} ratios of 1:0 (a), 2:1 (b), 1:1 (c), and 1:2 (d).

6.3.1.1 Synthesis of single collagen fibers

Single collagen fibers were synthesized by controlling the kinetics of collagen polymerization. Collagen polymerization was initiated by mixing a phosphate buffer (pH=7.4) with acid soluble type I collagen to induce self-assembly of collagen fibers. By monitoring

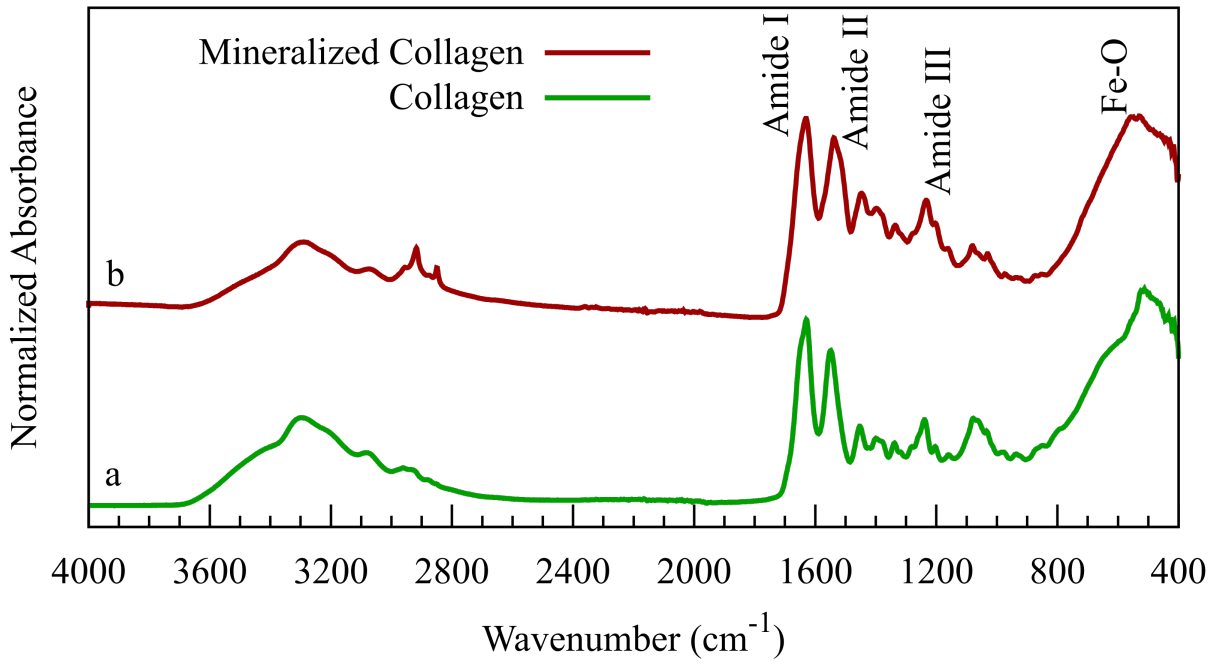

Figure 6.3: FTIR spectra of pure collagen (a) and collagen templated with PASP mineralized with iron oxide (b) the Fe^{2+}:Fe^{3+} ratio is 2:1

the turbidity at 313 nm of a polymerizing collagen solution, the morphology of collagen fibers at different time points within the polymerization process was observed, as shown in Figure 6.5. The typical kinetic profile is characterized by: (1) a lag phase (constant absorbance) where collagen monomers laterally aggregate together, (2) polymerization of collagen fibers characterized by and (3) a plateau indicating complete polymerization yielding a sigmoidal kinetic curve. The formation of collagen fibers are depicted at different times in Figure 6.5 (a-c). At the end of the lag phase (30 minutes, Figure 6.5 (a)) collagen monomers are aggregating together to form collagen fibers. Early in the polymerization phase (60 minutes, Figure 6.5 (b)) individual collagen fibers ranging from 1 to 10 μm in length are observed. At the end of the polymerization phase (120 minutes, Figure 6.5 (c)), a mesh of entangled collagen fibers is observed.

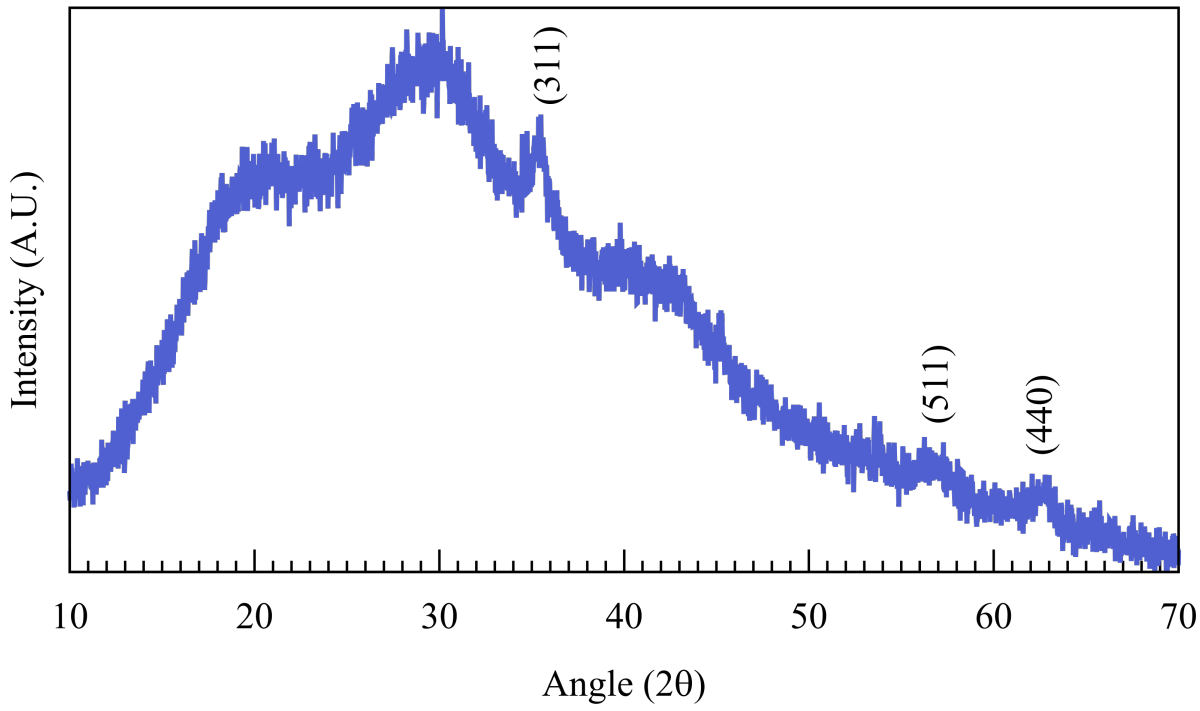

Figure 6.4: XRD pattern of collagen templated with PASP mineralized with iron oxide the Fe^{2+}:Fe^{3+} ratio of 2:1

6.3.2 Discussion

Mineralized type I collagen is the basic building block of bone and provides an organic framework for mineralization. Inspired by nature, biomimetic techniques were employed to mineralize collagen fibers with iron oxide. Poly-aspartic acid was used as a templating analog to mimic the acidic proteins in the body and to provide an excess of negative charges to attract positively charged iron ions into the gap zone. To test the hypothesis that electrostatic attraction between iron ions and negatively charged carboxylates promoted intrafibrillar mineralization, PAH was grafted to collagen to provide an excess of positive charges in an attempt to prevent intrafibrillar mineralization through electrostatic repulsion. As seen in Figure 6.1 (a) and (c), intrafibrillar mineralization was observed in PASP templated collagen and not in PAH templated collagen, suggesting that electrostatic interaction aids in intrafibrillar mineralization with iron oxide. The electrostatic interaction with PASP

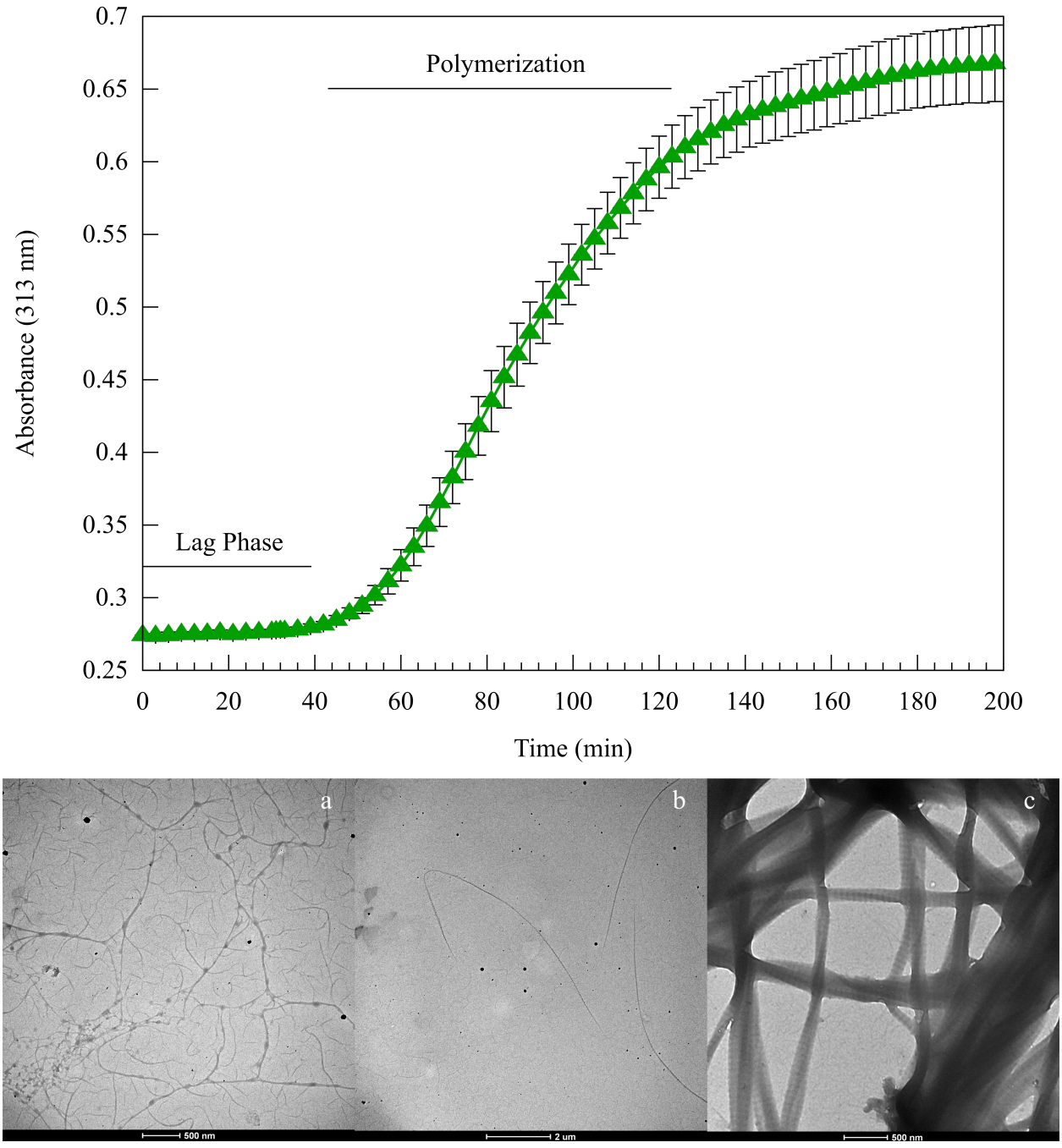

Figure 6.5: Top kinetic curve of collagen (0.5 mg/mL) polymerization at pH = 7.4. Below are TEM images of collagen fibers formed at 30 minutes (a), 60 minutes (b) and 120 minutes (c).

results in a larger concentration of iron ions within the gap zone that can precipitate into iron oxide when the pH is increased.

The Fe^{2+}:Fe^{3+} ratio is important in determining the mineralization pathway. Functionalized collagen fibers were incubated in a 4 mM iron chloride solution with varying Fe^{2+}:Fe^{3+} ratios to investigate the effect on mineralization. Iron oxide particles were formed on the surface and within the gap zone of collagen fibers. When Fe^{2+}:Fe^{3+} ratio is 1:0, light d-banding is observed but large crystals are present on the surface of the fibers. The formation of Fe_3O_4 or γ-Fe_2O_3 from a solution of Fe^{2+} occurs through a dissolution and re-precipitation process of a green rust precursor which tends to form large hexagonal shaped crystals in solution.[225] When Fe^{3+} is present and the concentration of Fe^{3+} is less than that of Fe^{2+}, the characteristic d-banding pattern is more evident with fewer large precipitates in solution. As the concentration of Fe^{3+} increases, more small particles are present on the surface of collagen fibers. The presence of Fe^{3+} promotes nanoparticle formation of ferrihdyrite in the size range of 2 to 6 nm. Ferrihydrite is more stable than green rust and precipitates first; these nanoparticles of ferrihydrite aggregate and mature into Fe_3O_4 or γ-Fe_2O_3 through dehydroxylation.[226]

The self-assembly of collagen-fibers is an entropy driven process, which makes difficult to precisely control fiber length. Through monitoring the kinetics during collagen polymerization, individual collagen fibers between 1 to 10 μm in length and around 100 to 200 nm in width are isolated. Fibers of this size are suitable for tumor targeting applications. The width of the fibers are small enough to penetrate the tumor, and the length allows the fibers to be flexible. The above mineralization strategy combined with collagen fibers that are synthesized through early termination polymerization can yield magnetic nanoworms for tumor therapy applications.

6.4 Conclusions

Intrafibrillar mineralization of collagen with iron oxide was achieved by templating collagen fibers with PASP, but templating with PAH resulted in visible intrafibrillar mineralization. The mineralized fibers were magnetically responsive with FTIR and XRD confirming

the formation of Fe_3O_4 or γ-Fe_2O_3. This approach to mineralizing collagen fibers can be applied to the single collagen fibers isolated during the early stage of polymerization to synthesis magnetic nanoworms.

CHAPTER SEVEN

Conlcusions and Future Work

7.1 Conclusions

Ion-exchange was used to synthesize manganese-, iron-, and cobalt-substituted hydroxyapatite powders. The synthesized powders were found to be phase-pure with no detectable second phases, and the incorporation of these ions were sufficient to induce a transition from diamagnetic behavior for pure HA to a paramagnetic one. DFT calculations of Mn^{2+}, Fe^{2+}, and Co^{2+} substitutions were in good agreement with the experimental data. The results from Chapter 2 underline the power of synergistic theoretical-experimental work in guiding the rational design of materials. Thus, the DFT calculation could be a useful tool for predicting physical and magnetic properties of different ion-substituted hydroxyapatite powders, and such a tool can be used to guide future studies on the synthesis of ion-substitute hydroxyapatite with desired properties.

In Chapter 2, Fe^{2+} had the highest degree of incorporation into HA compared Co^{2+} and Mn^{2+}, but Mn^{2+} contributed the most to the final magnetization due to its 5 unpaired electrons from its $[Ar]3d^5$ electron configuration. Iron displays multiple stable oxidation state with Fe^{3+} having a $[Ar]3d^5$ electron configuration. To increase magnetization, FeHA was synthesized using Fe^{3+} or a combination of Fe^{2+} and Fe^{3+}, and the magnetic properties of such samples are found to be dependent upon the oxidation state of iron and particle size. The presence of Fe^{3+} or a combination Fe^{2+} and Fe^{3+} resulted in a larger magnetization compared to Fe^{2+}HA. The combination of Fe^{2+} and Fe^{3+} displayed the most promising magnetic response with a coupled response at low fields, a paramagnetic response at high fields, and a magnetization comparable to Fe^{3+} which had the largest mass magnetization at high fields.

Transition metals are trace elements and are necessary for normal biological functions. The synthesized magnetic hydroxyapatite may be suitable for other biomedical applications where the bulk materials properties of interest. Previous sintering studies have shown that Fe- and Co-substituted HA is less thermally stable than pure HA, limiting them from being used in non-load bearing applications.[204, 227] As such, the sintering behavior of MnHA was compared to pure HA to assess the bulk properties and thermal stability of MnHA. Decomposition of MnHA into β-TCP and Mn_3O_4 occurred at 800 °C, while HA pellets started to sinter at 900 °C with partial decomposition to β-TCP and CaO. The maximum modulus of rupture achieved for HA and MnHA were 78 and 64 MPa, respectively. The low thermal stability of MnHA suggests that a faster dissolution rate *in vivo* than pure HA is expected.

The biocompatibility of FeHA, CoHA, and MnHA were assessed and compared to pure HA using a proliferation assay and a cytotoxicity assay. Overall, iron- and manganese-substituted HA powders demonstrated good biocompatibility, which makes them suitable for potential magnetic applications and other biomaterial applications, such as bone void fillers. Cobalt-substituted HA is suitable for short-term biomedical applications, such as serving as a magnetic contrast agent, where the material can be removed rapidly from the body. Further *in vivo* testing should be performed for all substituted HA powders.

The synthesized magnetic HAs are suitable for a wide range of magnetic applications but the rigid nature of these particles may not be well suited for tumor therapy applications. Magnetic nanoworms were developed by mineralizing type I collagen with iron oxide to yield semi-flexible and magnetic fibers. Intrafibrillar mineralization of collagen with iron oxide was achieved by templating collagen fibers with poly-aspartic acid. This approach to mineralizing collagen fibers can be applied to single collagen fibers isolated during the early-stage of collagen polymerization to synthesis magnetic nanoworms.

7.2 Future Work

7.2.1 Application Drivern Testing of Magnetic Hydroxyapatite

MnHA, FeHA, and CoHA have been synthesized and fully characterized. The predominately paramagnetic response at high magnetic fields indicates that these materials would be best suited as MRI contrast agents. *In vitro* determination of T_1 and T_2 relaxation times on nanoparticle solutions should be conducted with a clinical MRI machine or nuclear magnetic resonance spectrometer. After initial measurements, the magnetic HA should be surface functionalized for specific targeting applications such as bone micro-cracks. MRI is widely used for the diagnosis of stress fractures since the water molecules in the cracks provide better contrast compared to conventional X-rays. Thus adding a targeting agent to aid in the accumulation of magnetic HA within miro-cracks can provide better contrast for accurate diagnosis, and the excellent bioactivity of the materials may help promote faster bone healing. MnHA would be of the highest interest for such an application.

7.2.2 Application Driven Testing of Magnetic Nanoworms

A method of mineralizing collagen fibers with iron oxide has been developed, and thus should be subjected to application-driven testing. This will allow for further evaluation of the material for tumor therapy or as an MRI contrast agent. Preliminary *in vivo* testing for biodistribution and tumor accumulation should be assessed to verify the hypothesis the semi-flexible nature of the nanoworms can prolong circulation and tumor-site accumulation. In order to evaluate magnetic nanoworms *in vivo*, the nanoworms need to be functionalized with a fluorescent dye, such as Cy5.5, to allow for *in vivo* tracking.

The high magnetization values of iron oxides have made them popular contrast agents for MRI when using transverse relaxivity, R_2, to provide image contrast. The R_2 value can be measured *in vitro* using a clinical MRI machine or using an NMR spectrometer. Magnetic nanoworms are suspended at varying concentrations in solution and a spin echo

sequence is applied to measure the transverse relaxation time, T_2. The R_2 value is obtained by plotting the inverse of T_2 versus the iron concentration and fitting the data with a linear regression where the slope of the regression is R_2. The obtained R_2 value can be compared to a commercially available contrast agent, Feridex, which composed of superparamagnetic iron oxide coating with dextran, for assessing the potential as a T_2 contrast agent.

Superparamagnetic iron oxide materials are used capable of increasing the temperature of a solution via: Brownian relaxation, Néel relaxation, or hysteretic losses. As such, these materials are widely used for hyperthermia treatment. An alternating magnetic field with a field strength ranging from 4 to 10 kA m^{-1} and frequency ranging from 0.2 to 30 MHz is applied to induce heating. For assessing magnetic nanoworms, the aforementioned magnetic field and frequency ranges will be used to induce heating of magnetic nanoworms suspended in a physiological buffer, while recording temperature versus time. From this data the applicability of nanoworms for hyperthermia can be assessed by calculating the specific absorption rate (SAR):

$$SAR = \frac{C_p}{m}\frac{dT}{dt} \tag{1}$$

where: C_p is the specific heat of the medium, m is the total mass of suspended nanoworms, and $\frac{dT}{dt}$ is the rate of change of the temperature. The SAR will be determined for different field and frequency combinations, and the effect of nanoworm size on SAR will also be investigated. Again, the obtained SAR will be compared to literature values as a method to screen the material for hyperthermia.

The high shape anisotropy of magnetic nanoworms may make the material capable of acting as a nanobot. Magnetic rods/helices/filaments are capable of acting as a nanobot by applying a uniform rotating magnetic field that allows the user to directly control the 'swimming' motion of the nanobot. The swimming motion may be monitored with fluorescent microscopy by conjugating a fluorescent dye to the nanoworm. This effect is desirable for potentially targeting tumors that are in the intraperitoneal cavity. Current

magnetic targeting techniques rely on the application of static magnetic field gradients that are easily applied externally, which results in the magnetic material being pulled towards the surface. The ability of non-invasive magnetic fields to externally manipulate the 'swimming' motion may be advantageous at improving penetration of magnetic nanoworms into tumors and can be used in conjunction with other magnetic therapy techniques i.e. hyperthermia.

References

[1] G. F. Goya, V. Grazu, and M. R. Ibarra. Magnetic nanoparticles for cancer therapy. *Current Nanoscience*, 4(1):1–16, 2008.

[2] Ajay Kumar Gupta and Mona Gupta. Synthesis and surface engineering of iron oxide nanoparticles for biomedical applications. *Biomaterials*, 26(18):3995 – 4021, 2005.

[3] Amanda K. A. Silva, Jelena Kolosnjaj-Tabi, Stephanie Bonneau, Iris Marangon, Nicole Boggetto, Kelly Aubertin, Olivier Clément, Michel Francis Bureau, Nathalie Luciani, Florence Gazeau, and Claire Wilhelm. Magnetic and photoresponsive theranosomes: Translating cell-released vesicles into smart nanovectors for cancer therapy. *ACS Nano*, 7(6):4954–4966, 2013.

[4] Anna Tampieri, Simone Sprio, Monica Sandri, and Federica Valentini. Mimicking natural bio-mineralization processes: A new tool for osteochondral scaffold development. *Trends in Biotechnology*, 29(10):526 – 535, 2011.

[5] Courtney R. Thomas, Daniel P. Ferris, Jae-Hyun Lee, Eunjoo Choi, Mi Hyeon Cho, Eun Sook Kim, J. Fraser Stoddart, Jeon-Soo Shin, Jinwoo Cheon, and Jeffrey I. Zink. Noninvasive remote-controlled release of drug molecules in vitro using magnetic actuation of mechanized nanoparticles. *Journal of the American Chemical Society*, 132(31):10623–10625, 2010.

[6] Jon Dobson. Magnetic nanoparticles for drug delivery. *Drug Development Research*, 67(1):55–60, 2006.

[7] Stephane Mornet, Sebastien Vasseur, Fabien Grasset, and Etienne Duguet. Magnetic nanoparticle design for medical diagnosis and therapy. *J. Mater. Chem.*, 14:2161–2175, 2004.

[8] Steven Hughes, Jon Dobson, and Alicia J. El Haj. Magnetic targeting of mechanosensors in bone cells for tissue engineering applications. *Journal of Biomechanics*, 40(1):S96–S104, 2007.

[9] Steven Hughes, Alicia J. El Haj, and Jon Dobson. Magnetic micro- and nanoparticle mediated activation of mechanosensitive ion channels. *Medical Engineering & Physics*, 27(9):754 – 762, 2005.

[10] Chun-Han Hou, Sheng-Mou Hou, Yu-Sheng Hsueh, Jinn Lin, Hsi-Chin Wu, and Feng-Huei Lin. The in vivo performance of biomagnetic hydroxyapatite nanoparticles in cancer hyperthermia therapy. *Biomaterials*, 30(23-24):3956 – 3960, 2009.

[11] Ivo Šafařík and Mirka Šafaříková. Use of magnetic techniques for the isolation of cells. *Journal of Chromatography B: Biomedical Sciences and Applications*, 722(1-2):33 – 53, 1999.

[12] Sophie Laurent, Delphine Forge, Marc Port, Alain Roch, Caroline Robic, Luce Vander Elst, and Robert N. Muller. Magnetic iron oxide nanoparticles: Synthesis, stabilization, vectorization, physicochemical characterizations, and biological applications. *Chemical Reviews*, 108(6):2064–2110, 2008.

[13] Zhen Fan, Dulal Senapati, Anant Kumar Singh, and Paresh Chandra Ray. Theranostic magnetic core-plasmonic shell star shape nanoparticle for the isolation of targeted rare tumor cells from whole blood, fluorescence imaging, and photothermal destruction of cancer. *Molecular Pharmaceutics*, 10(3):857–866, 2013.

[14] Sang Jun Son, Jonathan Reichel, Bo He, Mattan Schuchman, and Sang Bok Lee. Magnetic nanotubes for magnetic-field-assisted bioseparation, biointeraction, and drug delivery. *Journal of the American Chemical Society*, 127(20):7316–7317, 2005.

[15] Takayuki Asahara, Toyoaki Murohara, Alison Sullivan, Marcy Silver, Rien van der Zee, Tong Li, Bernhard Witzenbichler, Gina Schatteman, and Jeffrey M. Isner. Isolation of

putative progenitor endothelial cells for angiogenesis. *Science*, 275(5302):964–966, 1997.

[16] Jiahua Zhou, Liang Hu, Zeqian Yu, Jie Zheng, Detong Yang, Michael Bouvet, and Robert M. Hoffman. Marker expression in circulating cancer cells of pancreatic cancer patients. *Journal of Surgical Research*, 171(2):631 – 636, 2011.

[17] Q. A. Pankhurst, N. T. K. Thanh, S. K. Jones, and J. Dobson. Progress in applications of magnetic nanoparticles in biomedicine. *Journal of Physics D: Applied Physics*, 42(22):224001, 2009.

[18] Jon Dobson. Remote control of cellular behaviour with magnetic nanoparticles. *Nature Nanotechnology*, 3(3):139–143, 2008.

[19] Nathan J. Sniadecki. Minireview: A tiny touch: Activation of cell signaling pathways with magnetic nanoparticles. *Endocrinology*, 151(2):451–457, 2010.

[20] Andreas R. Bausch, Ulrike Hellerer, Markus Essler, Martin Aepfelbacher, and Erich Sackmann. Rapid stiffening of integrin receptor-actin linkages in endothelial cells stimulated with thrombin: A magnetic bead microrheology study. *Biophysical Journal*, 80(6):2649 – 2657, 2001.

[21] Janos M. Kanczler, Harpul S. Sura, Julia Magnay, David Green, Richard O.C. Oreffo, Jon P. Dobson, and Alicia J. El Haj. Controlled differentiation of human bone marrow stromal cells using magnetic nanoparticle technology. *Tissue Engineering Part A*, 16(10):3241–3250, 2010.

[22] Gaurav Tiwari, Ruchi Tiwari, Birendra Sriwastawa, L Bhati, S Pandey, P Pandey, and Saurabh K Bannerjee. Drug delivery systems: An updated review. *International Journal of Pharmaceutical Investigation*, 2:2–11, 2012.

[23] Conroy Sun, Jerry S.H. Lee, and Miqin Zhang. Magnetic nanoparticles in MR imaging and drug delivery. *Advanced Drug Delivery Reviews*, 60(11):1252 – 1265, 2008.

[24] Rainer Tietze, Jan Zaloga, Harald Unterweger, Stefan Lyer, Ralf P. Friedrich, Christina Janko, Marina Pöttler, Stephan Dürr, and Christoph Alexiou. Magnetic nanoparticle-based drug delivery for cancer therapy. *Biochemical and Biophysical Research Communications*, 468(3):463 – 470, 2015.

[25] Challa S.S.R. Kumar and Faruq Mohammad. Magnetic nanomaterials for hyperthermia-based therapy and controlled drug delivery. *Advanced Drug Delivery Reviews*, 63(9):789 – 808, 2011.

[26] AS Lubbe, C Bergemann, W Huhnt, T Fricke, H Riess, JW Brock, and D Huhn. Preclinical experiences with magnetic drug targeting: tolerance and efficacy. *Cancer Research*, 56(20):4694–701, 1996.

[27] Nathalie Schleich, Chrystelle Po, Damien Jacobs, Bernard Ucakar, Bernard Gallez, Fabienne Danhier, and Véronique Préat. Comparison of active, passive and magnetic targeting to tumors of multifunctional paclitaxel/spio-loaded nanoparticles for tumor imaging and therapy. *Journal of Controlled Release*, 194:82 – 91, 2014.

[28] Adam J. Cole, Allan E. David, Jianxin Wang, Craig J. Galbán, and Victor C. Yang. Magnetic brain tumor targeting and biodistribution of long-circulating peg-modified, cross-linked starch-coated iron oxide nanoparticles. *Biomaterials*, 32(26):6291 – 6301, 2011.

[29] Christoph Alexiou, Wolfgang Arnold, Roswitha J. Klein, Fritz G. Park, Peter Hulin, Christian Bergemann, Wolfgang Erhardt, Stefan Wagenpfeil, and Adreas S. Lubbe. Locoregional cancer treatment with magnetic drug targeting. *Cancer Research*, 60:6641–6648, 2000.

[30] Greg J. Stanisz, Ewa E. Odrobina, Joseph Pun, Michael Escaravage, Simon J. Graham, Michael J. Bronskill, and R. Mark Henkelman. T_1, T_2 relaxation and magnetization transfer in tissue at 3T. *Magnetic Resonance in Medicine*, 54(3):507–512, 2005.

[31] Hyon Bin Na, In Chan Song, and Taeghwan Hyeon. Inorganic nanoparticles for MRI contrast agents. *Advanced Materials*, 21(21):2133–2148, 2009.

[32] Hyon Bin Na, Jung Hee Lee, Kwangjin An, Yong Il Park, Mihyun Park, In Su Lee, Do-Hyun Nam, Sung Tae Kim, Seung-Hoon Kim, Sang-Wook Kim, Keun-Ho Lim, Ki-Soo Kim, Sun-Ok Kim, and Taeghwan Hyeon. Development of a T_1 contrast agent for magnetic resonance imaging using MnO nanoparticles. *Angewandte Chemie*, 119(28):5493–5497, 2007.

[33] Xia Wang, Dechao Niu, Qing Wu, Song Bao, Teng Su, Xiaohang Liu, Shengjian Zhang, and Qigang Wang. Iron oxide/manganese oxide co-loaded hybrid nanogels as pH-responsive magnetic resonance contrast agents. *Biomaterials*, 53:349 – 357, 2015.

[34] Guannan Wang, Xuanjun Zhang, Andreas Skallberg, Yaxu Liu, Zhangjun Hu, Xifan Mei, and Kajsa Uvdal. One-step synthesis of water-dispersible ultra-small Fe_3O_4 nanoparticles as contrast agents for T_1 and T_2 magnetic resonance imaging. *Nanoscale*, 6:2953–2963, 2014.

[35] Ulrich I. Tromsdorf, Nadja C. Bigall, Michael G. Kaul, Oliver T. Bruns, Marija S. Nikolic, Birgit Mollwitz, Ralph A. Sperling, Rudolph Reimer, Heinz Hohenberg, Wolfgang J. Parak, Stephan Förster, Ulrike Beisiegel, Gerhard Adam, and Horst Weller. Size and surface effects on the MRI relaxivity of manganese ferrite nanoparticle contrast agents. *Nano Letters*, 7(8):2422–2427, 2007.

[36] Ja Young Park, Myung Ju Baek, Eun Sook Choi, Seungtae Woo, Joo Hyun Kim, Tae Jeong Kim, Jae Chang Jung, Kwon Seok Chae, Yongmin Chang, and Gang Ho

Lee. Paramagnetic ultrasmall gadolinium oxide nanoparticles as advanced T_1 MRI contrast agent: Account for large longitudinal relaxivity, optimal particle diameter, and in vivo T_1 MR images. *ACS Nano*, 3(11):3663–3669, 2009.

[37] Wenlong Xu, Krishna Kattel, Ja Young Park, Yongmin Chang, Tae Jeong Kim, and Gang Ho Lee. Paramagnetic nanoparticle T_1 and T_2 MRI contrast agents. *Phys. Chem. Chem. Phys.*, 14:12687–12700, 2012.

[38] P Wust, B Hildebrandt, G Sreenivasa, B Rau, J Gellermann, H Riess, R Felix, and PM Schlag. Hyperthermia in combined treatment of cancer. *The Lancet Oncology*, 3(8):487 – 497, 2002.

[39] F. Kristian Storm, William H. Harrison, Robert S. Elliot, and Donald L. Morton. Normal tissue and solid tumor effects of hyperthermia in animal models and clinical trials. *Cancer Research*, 39:2245–2251, 1979.

[40] Rudolf Hergt, Silvio Dutz, Robert Müller, and Matthias Zeisberger. Magnetic particle hyperthermia: nanoparticle magnetism and materials development for cancer therapy. *Journal of Physics: Condensed Matter*, 18(38):S2919, 2006.

[41] Pablo Guardia, Riccardo Di Corato, Lenaic Lartigue, Claire Wilhelm, Ana Espinosa, Mar Garcia-Hernandez, Florence Gazeau, Liberato Manna, and Teresa Pellegrino. Water-soluble iron oxide nanocubes with high values of specific absorption rate for cancer cell hyperthermia treatment. *ACS Nano*, 6(4):3080–3091, 2012.

[42] Jean-Paul Fortin, Claire Wilhelm, Jacques Servais, Christine Ménager, Jean-Claude Bacr, , and Florence Gazeau. Size-sorted anionic iron oxide nanomagnets as colloidal mediators for magnetic hyperthermia. *Journal of the American Chemical Society*, 129(9):2628–2635, 2007.

[43] Garheng Kong, Rod D. Braun, and Mark W. Dewhirst. Characterization of the effect

of hyperthermia on nanoparticle extravasation from tumor vasculature. *Cancer Research*, 61:3027–3032, 2001.

[44] Garheng Kong, Rod D. Braun, and Mark W. Dewhirst. Hyperthermia enables tumor-specific nanoparticle delivery: Effect of particle size. *Cancer Research*, 60:4440–4445, 2000.

[45] Chang W. Song. Effect of local hyperthermia on blood flow and microenvironment: A review. *Cancer Research*, 44:4721s–4730s, 1984.

[46] Morteza Mahmoudi, Heinrich Hofmann, Barbara Rothen-Rutishauser, and Alke Petri-Fink. Assessing the in vitro and in vivo toxicity of superparamagnetic iron oxide nanoparticles. *Chemical Reviews*, 112(4):2323–2338, 2012.

[47] Stefaan J.H. Soenen, Uwe Himmelreich, Nele Nuytten, and Marcel De Cuyper. Cytotoxic effects of iron oxide nanoparticles and implications for safety in cell labelling. *Biomaterials*, 32(1):195 – 205, 2011.

[48] Veronica I. Shubayev, Thomas R. Pisanic II, and Sungho Jin. Magnetic nanoparticles for theranostics. *Advanced Drug Delivery Reviews*, 61(6):467 – 477, 2009.

[49] Hamed Arami, Amit Khandhar, Denny Liggitt, and Kannan M. Krishnan. In vivo delivery, pharmacokinetics, biodistribution and toxicity of iron oxide nanoparticles. *Chem. Soc. Rev.*, 44:8576–8607, 2015.

[50] Morteza Mahmoudi, Sophie Laurent, Mohammad A. Shokrgozar, and Mohsen Hosseinkhani. Toxicity evaluations of superparamagnetic iron oxide nanoparticles: Cell "vision" versus physicochemical properties of nanoparticles. *ACS Nano*, 5(9):7263–7276, 2011.

[51] Thomas R. Pisanic II, Jennifer D. Blackwell, Veronica I. Shubayev, Rita R. Fiñones,

and Sungho Jin. Nanotoxicity of iron oxide nanoparticle internalization in growing neurons. *Biomaterials*, 28(16):2572 – 2581, 2007.

[52] Neenu Singh, Gareth J.S. Jenkins, Romisa Asadi, and Shareen H. Doaka. Potential toxicity of superparamagnetic iron oxide nanoparticles (spion). *Nano Reviews*, 1:5358, 2010.

[53] H. Markides, M. Rotherham, and A. J. El Haj. Biocompatibility and toxicity of magnetic nanoparticles in regenerative medicine. *Journal of Nanomaterials*, 2012:614094, 2012.

[54] Bettina Kozissnik and Jon Dobson. Biomedical applications of mesoscale magnetic particles. *MRS Bulletin*, 38(11):927–932, 2013.

[55] Wojciech Suchanek and Masahiro Yoshimura. Processing and properties of hydroxyapatite-based biomaterials for use as hard tissue replacement implants. *Journal of Materials Research*, 13(01):94–117, 1998.

[56] M. P. Ferraz, F. J. Monteiro, and C. M. Manuel. Hydroxyapatite nanoparticles: A review of preparation methodologies. *Journal of Applied Biomaterials & Biomechanics*, 2:74–80, 2004.

[57] A. Vladescu, I. Birlik, V. Braic, M. Toparli, E. Celik, and F. Ak Azem. Enhancement of the mechanical properties of hydroxyapatite by SiC addition. *Journal of the Mechanical Behavior of Biomedical Materials*, 40:362 – 368, 2014.

[58] Adriana Bigi, Elisa Boanini, Chiara Capuccini, and Massimo Gazzano. Strontium-substituted hydroxyapatite nanocrystals. *Inorganica Chimica Acta*, 360(3):1009 – 1016, 2007.

[59] L. Medvecký, R. Łtulajterová, L. Parilák, J. Trpcevská, J. DuriŽin, and S.M. Barinov. Influence of manganese on stability and particle growth of hydroxyapatite in simu-

lated body fluid. *Colloids and Surfaces A: Physicochemical and Engineering Aspects*, 281(1 - 3):221 – 229, 2006.

[60] Silvia Panseri, Carla Cunha, Teresa D'Alessandro, Monica Sandri, Gianluca Giavaresi, Maurilio Marcacci, Clark T Hung, and Anna Tampieri. Intrinsically superparamagnetic Fe-hydroxyapatite nanoparticles positively influence osteoblast-like cell behaviour. *Journal of Nanobiotechnology*, 10(1):1–10, 2012.

[61] Hsi-Chin Wu, Tzu-Wei Wang, Jui-Sheng Sun, Wen-Hsi Wang, and Feng-Huei Lin. A novel biomagnetic nanoparticle based on hydroxyapatite. *Nanotechnology*, 18(16):165601, 2007.

[62] Yan Li, Jasmine Widodo, Sierin Lim, and Chui Ping Ooi. Synthesis and cytocompatibility of manganese (ii) and iron (iii) substituted hydroxyapatite nanoparticles. *Journal of Materials Science*, 47(2):754–763, 2011.

[63] Erica R. Kramer, Aimee M. Morey, Margo Staruch, Steven L. Suib, Menka Jain, Joseph I. Budnick, and Mei Wei. Synthesis and characterization of iron-substituted hydroxyapatite via a simple ion-exchange procedure. *Journal of Materials Science*, 48(2):665–673, 2012.

[64] V. Sarath Chandra, Ganga Baskar, R. V. Suganthi, K. Elayaraja, M. I. Ahymah Joshy, W. Sofi Beaula, R. Mythili, Ganesh Venkatraman, and S. Narayana Kalkura. Blood compatibility of iron-doped nanosize hydroxyapatite and its drug release. *ACS Applied Materials & Interfaces*, 4(3):1200–1210, 2012.

[65] M. E. Zilm, M. Staruch, M. Jain, and Mei Wei. An intrinsically magnetic biomaterial with tunable magnetic properties. *Journal of Materials Chemistry B*, 2(41):7176–7185, 2014.

[66] D. E. Ellis, Joice Terra, O. Warschkow, M. Jiang, Gabriela B. Gonzalez, J. S. Okasinski, M. J. Bedzyk, Alexandre M. Rossi, and Jean-Guillaume Eon. A theoretical and

experimental study of lead substitution in calcium hydroxyapatite. *Phys. Chem. Chem. Phys.*, 8:967–976, 2006.

[67] S. Hirano and K.T. Suzuki. Exposure, metabolism, and toxicity of rare earths and related compounds. *Environmental Health Perspectives*, 104:85–95, 1996.

[68] Simon P. Fricker. The therapeutic application of lanthanides. *Chem. Soc. Rev.*, 35(6):524–533, 2006.

[69] Kenneth N. Raymond and Valérie C. Pierre. Next generation, high relaxivity gadolinium MRI agents. *Bioconjugate Chemistry*, 16(1):3–8, 2005.

[70] Sutapa Barua, Jin-Wook Yoo, Poornima Kolhar, Aditya Wakankar, Yatin R. Gokarn, and Samir Mitragotri. Particle shape enhances specificity of antibody-displaying nanoparticles. *Proceedings of the National Academy of Sciences*, 110(9):3270–3275, 2013.

[71] Robby A. Petros and Joseph M. DeSimone. Strategies in the design of nanoparticles for therapeutic applications. *Nature Reviews Drug Discovery*, 9(8):615–627, 2010.

[72] Dong Hyun Jo, Jin Hyoung Kim, Tae Geol Lee, and Jeong Hun Kim. Size, surface charge, and shape determine therapeutic effects of nanoparticles on brain and retinal diseases. *Nanomedicine: Nanotechnology, Biology and Medicine*, 11(7):1603–1611, 2015.

[73] Randall Toy, Pubudu M Peiris, Ketan B Ghaghada, and Efstathios Karathanasis. Shaping cancer nanomedicine: the effect of particle shape on the in vivo journey of nanoparticles. *Nanomedicine*, 9(1):121–134, 2013.

[74] P. Decuzzi, B. Godin, T. Tanaka, S.-Y. Lee, C. Chiappini, X. Liu, and M. Ferrari. Size and shape effects in the biodistribution of intravascularly injected particles. *Journal of Controlled Release*, 141(3):320 – 327, 2010.

[75] Markus Müllner, Sarah J. Dodds, Tri-Hung Nguyen, Danielle Senyschyn, Christopher J. H. Porter, Ben J. Boyd, and Frank Caruso. Size and rigidity of cylindrical polymer brushes dictate long circulating properties in vivo. *ACS Nano*, 9(2):1294–1304, 2015.

[76] Yan Geng, Paul Dalhaimer, Shenshen Cai, Richard Tsai, Manorama Tewari, Tamara Minko, and Dennis E. Discher. Shape effects of filaments versus spherical particles in flow and drug delivery. *Nature Nanotechnology*, 2(4):249–355, 2007.

[77] Sharon M. Loverde, Michael L. Klein, and Dennis E. Discher. Nanoparticle shape improves delivery: Rational coarse grain molecular dynamics (rcg-md) of taxol in worm-like peg-pcl micelles. *Advanced Materials*, 24(28):3823–3830, 2012.

[78] David A. Christian, Shenshen Cai, Olga B. Garbuzenko, Takamasa Harada, Allison L. Zajac, Tamara Minko, and Dennis E. Discher. Flexible filaments for in vivo imaging and delivery: Persistent circulation of filomicelles opens the dosage window for sustained tumor shrinkage. *Molecular Pharmaceutics*, 6(5):1343–1352, 2009.

[79] Ji-Ho Park, Geoffrey von Maltzahn, Lianglin Zhang, Michael P. Schwartz, Erkki Ruoslahti, Sangeeta N. Bhatia, and Michael J. Sailor. Magnetic iron oxide nanoworms for tumor targeting and imaging. *Advanced Materials*, 20(9):1630–1635, 2008.

[80] Ji-Ho Park, Geoffrey von Maltzahn, Lianglin Zhang, Austin M. Derfus, Dmitri Simberg, Todd J. Harris, Erkki Ruoslahti, Sangeeta N. Bhatia, and Michael J. Sailor. Systematic surface engineering of magnetic nanoworms for in vivo tumor targeting. *Small*, 5(6):694–700, 2009.

[81] Guankui Wang, Swetha Inturi, Natalie J. Serkova, Sergey Merkulov, Keith McCrae, Stephen E. Russek, Nirmal K. Banda, and Dmitri Simberg. High-relaxivity superparamagnetic iron oxide nanoworms with decreased immune recognition and long-circulating properties. *ACS Nano*, 8(12):12437–12449, 2014.

[82] Douglas E. Rodriguez, Taili Thula-Mata, Edgardo J. Toro, Ya-Wen Yeh, Carl Holt, L. Shannon Holliday, and Laurie B. Gower. Multifunctional role of osteopontin in directing intrafibrillar mineralization of collagen and activation of osteoclasts. *Acta Biomaterialia*, 10(1):494 – 507, 2014.

[83] Yan Liu, Nan Li, Yi-pin Qi, Lin Dai, Thomas E. Bryan, Jing Mao, David H. Pashley, and Franklin R. Tay. Intrafibrillar collagen mineralization produced by biomimetic hierarchical nanoapatite assembly. *Advanced Materials*, 23(8):975–980, 2011.

[84] Yan Liu, Young-Kyung Kim, Lin Dai, Nan Li, Sara O. Khan, David H. Pashley, and Franklin R. Tay. Hierarchical and non-hierarchical mineralisation of collagen. *Biomaterials*, 32(5):1291 – 1300, 2011.

[85] Hongjian Zhou and Jaebeom Lee. Nanoscale hydroxyapatite particles for bone tissue engineering. *Acta Biomaterialia*, 7(7):2769 – 2781, 2011.

[86] Thomas J. Webster, Elizabeth A. Massa-Schlueter, Jennifer L. Smith, and Elliot B. Slamovich. Osteoblast response to hydroxyapatite doped with divalent and trivalent cations. *Biomaterials*, 25(11):2111 – 2121, 2004.

[87] Weichang Xue, Jessica L. Moore, Howard L. Hosick, Susmita Bose, Amit Bandyopadhyay, W.W. Lu, Kenneth M.C. Cheung, and Keith D.K. Luk. Osteoprecursor cell response to strontium-containing hydroxyapatite ceramics. *Journal of Biomedical Materials Research Part A*, 79A(4):804–814, 2006.

[88] E. Landi, G. Celotti, G. Logroscino, and A. Tampieri. Carbonated hydroxyapatite as bone substitute. *Journal of the European Ceramic Society*, 23(15):2931 – 2937, 2003.

[89] N. Patel, S. M. Best, W. Bonfield, I. R. Gibson, K. A. Hing, E. Damien, and P. A. Revell. A comparative study on the in vivo behavior of hydroxyapatite and silicon substituted hydroxyapatite granules. *Journal of Materials Science: Materials in Medicine*, 13(12):1199–1206.

[90] E. Boanini, M. Gazzano, and A. Bigi. Ionic substitutions in calcium phosphates synthesized at low temperature. *Acta Biomaterialia*, 6(6):1882 – 1894, 2010.

[91] Susmita Bose, Gary Fielding, Solaiman Tarafder, and Amit Bandyopadhyay. Understanding of dopant-induced osteogenesis and angiogenesis in calcium phosphate ceramics. *Trends in Biotechnology*, 31(10):594 – 605, 2013.

[92] R. J. P. Williams. Role of transition metal ions in biological processes. *R. Inst. Chem., Rev.*, 1:13–38, 1968.

[93] Hengyi Xu, Zoraida P. Aguilar, Lily Yang, Min Kuang, Hongwei Duan, Yonghua Xiong, Hua Wei, and Andrew Wang. Antibody conjugated magnetic iron oxide nanoparticles for cancer cell separation in fresh whole blood. *Biomaterials*, 32(36):9758 – 9765, 2011.

[94] Q A Pankhurst, J Connolly, S K Jones, and J Dobson. Applications of magnetic nanoparticles in biomedicine. *Journal of Physics D: Applied Physics*, 36(13):R167.

[95] Omid Veiseh, Jonathan W. Gunn, and Miqin Zhang. Design and fabrication of magnetic nanoparticles for targeted drug delivery and imaging. *Advanced Drug Delivery Reviews*, 62(3):284 – 304, 2010.

[96] Erica Kramer, Emily Itzkowitz, and Mei Wei. Synthesis and characterization of cobalt-substituted hydroxyapatite powders. *Ceramics International*, 40(8, Part B):13471 – 13480, 2014.

[97] David Lindsay and William Kerr. Cobalt close. *Nature Chemistry*, 3(6):494, 2011.

[98] Yun-Jung Bae and Mi-Hyun Kim. Manganese supplementation improves mineral density of the spine and femur and serum osteocalcin in rats. *Biological Trace Element Research*, 124(1):28–34, 2008.

[99] H Rico, N Gómez-Raso, M Revilla, ER Hernández, C Seco, E Páez, and E Crespo. Effects on bone loss of manganese alone or with copper supplement in ovariectomized rats. a morphometric and densitomeric study. *European journal of obstetrics, gynecology, and reproductive biology*, 90(1):97 – 101, 2000.

[100] J. Terra, G. B. Gonzalez, A. M. Rossi, J. G. Eon, and D. E. Ellis. Theoretical and experimental studies of substitution of cadmium into hydroxyapatite. *Phys. Chem. Chem. Phys.*, 12:15490–15500, 2010.

[101] Joice Terra, Erico Rodrigues Dourado, Jean-Guillaume Eon, Donald E. Ellis, Gabriela Gonzalez, and Alexandre Malta Rossi. The structure of strontium-doped hydroxyapatite: an experimental and theoretical study. *Phys. Chem. Chem. Phys.*, 11:568–577, 2009.

[102] Jacek Zeglinski, Michael Nolan, Michael Bredol, Andrea Schatte, and Syed A. M. Tofail. Unravelling the specific site preference in doping of calcium hydroxyapatite with strontium from ab initio investigations and rietveld analyses. *Phys. Chem. Chem. Phys.*, 14:3435–3443, 2012.

[103] Shuxia Yin and Donald E. Ellis. First-principles investigations of Ti-substituted hydroxyapatite electronic structure. *Phys. Chem. Chem. Phys.*, 12:156–163, 2010.

[104] Danielle Laurencin, Neyvis Almora-Barrios, Nora H. de Leeuw, Christel Gervais, Christian Bonhomme, Francesco Mauri, Wojciech Chrzanowski, Jonathan C. Knowles, Robert J. Newport, Alan Wong, Zhehong Gan, and Mark E. Smith. Magnesium incorporation into hydroxyapatite. *Biomaterials*, 32(7):1826 – 1837, 2011.

[105] Xiaoyan Ma and Donald E. Ellis. Initial stages of hydration and Zn substitution/occupation on hydroxyapatite (0 0 0 1) surfaces. *Biomaterials*, 29(3):257 – 265, 2008.

[106] R. Astala, L. Calderín, X. Yin, , and M. J. Stott. Ab initio simulation of Si-doped hydroxyapatite. *Chemistry of Materials*, 18(2):413 – 422, 2006.

[107] H. F. Chappell and P. D. Bristowe. Density functional calculations of the properties of silicon-substituted hydroxyapatite. *Journal of Materials Science: Materials in Medicine*, 18(5):829–837, 2006.

[108] R. Astala, , and M. J. Stott. First principles investigation of mineral component of bone: Co_3 substitutions in hydroxyapatite. *Chemistry of Materials*, 17(16):4125–4133, 2005.

[109] N. H. de Leeuw. Density functional theory calculations of local ordering of hydroxy groups and fluoride ions in hydroxyapatite. *Phys. Chem. Chem. Phys.*, 4:3865–3871, 2002.

[110] Soumya S. Bhat, Umesh V. Waghmare, and Upadrasta Ramamurty. First-principles study of structure, vibrational, and elastic properties of stoichiometric and calcium-deficient hydroxyapatite. *Crystal Growth & Design*, 14(6):3131–3141, 2014.

[111] Paul Rulis, Lizhi Ouyang, and W. Y. Ching. Electronic structure and bonding in calcium apatite crystals: Hydroxyapatite, fluorapatite, chlorapatite, and bromapatite. *Phys. Rev. B*, 70(15):155104, 2004.

[112] Ming Jiang, J. Terra, A. M. Rossi, M. A. Morales, E. M. Baggio Saitovitch, and D. E. Ellis. Fe^{2+}/Fe^{3+} substitution in hydroxyapatite: Theory and experiment. *Phys. Rev. B*, 66(22):224107, 2002.

[113] Marat Gafurov, Timur Biktagirov, Georgy Mamin, Elena Klimashina, Valery Putlayev, L. Kuznetsova, and Sergei Orlinskii. The interplay of manganese and nitrate in hydroxyapatite nanoparticles as revealed by pulsed EPR and DFT. *Phys. Chem. Chem. Phys.*, 17:20331–20337, 2015.

[114] Marat Gafurov, Timur Biktagirov, Georgy Mamin, and Sergei Orlinskii. A DFT, X- and W-band EPR and ENDOR study of nitrogen-centered species in (nano)hydroxyapatite. *Applied Magnetic Resonance*, 45(11):1189–1203, 2014.

[115] Timur Biktagirov, Marat Gafurov, Georgy Mamin, Elena Klimashina, Valery Putlayev, and Sergei Orlinskii. Combination of EPR measurements and DFT calculations to study nitrate impurities in the carbonated nanohydroxyapatite. *The Journal of Physical Chemistry A*, 118(8):1519–1526, 2014.

[116] A. C. Larson and R.B. Von Dreele. General structure analysis system (GSAS). *Los Alamos National Laboratory Report LAUR*, pages 86–748, 2000.

[117] Brian H. Toby. *EXPGUI*, a graphical user interface for *GSAS*. *Journal of Applied Crystallography*, 34(2):210–213, 2001.

[118] G. Kresse and J. Furthmüller. Efficient iterative schemes for *ab initio* total-energy calculations using a plane-wave basis set. *Phys. Rev. B*, 54(16):11169–11186, 1996.

[119] John P. Perdew, Kieron Burke, and Matthias Ernzerhof. Generalized gradient approximation made simple. *Phys. Rev. Lett.*, 77(18):3865–3868, 1996.

[120] Hendrik J. Monkhorst and James D. Pack. Special points for brillouin-zone integrations. *Phys. Rev. B*, 13(12):5188–5192, 1976.

[121] A. S. Posner, A. Perloff, and A. F. Diorio. Refinement of the hydroxyapatite structure. *Acta Crystallographica*, 11(4):308–309, 1958.

[122] Vincenzo Fiorentini and M Methfessel. Extracting convergent surface energies from slab calculations. *Journal of Physics: Condensed Matter*, 8(36):6525, 1996.

[123] Weihua Zhu and Ping Wu. Surface energetics of hydroxyapatite: a DFT study. *Chemical Physics Letters*, 396(1 - 3):38 – 42, 2004.

[124] Ljiljana Veselinović, Ljiljana Karanović, Zoran Stojanović, Ines Bračko, Smilja Marković, Nenad Ignjatović, and Dragan Uskoković. Crystal structure of cobalt-substituted calcium hydroxyapatite nanopowders prepared by hydrothermal processing. *Journal of Applied Crystallography*, 43(2):320–327, 2010.

[125] David Briggs and Martin P. Seah. *Practical surface analysis: by auger and x-ray photoelectron spectroscopy*. Wiley & Sons, Chichester, 1983.

[126] I. Mayer, G. Peto, A. Karacs, G. Molnár, and I. Popov. Divalent Mn in calcium hydroxyapatite by pulse laser deposition. *Journal of Inorganic Biochemistry*, 104(10):1107 – 1111, 2010.

[127] Yu.G. Borod'ko, S.I. Vetchinkin, S.L. Zimont, I.N. Ivleva, and Yu.M. Shul'ga. Nature of satellites in X-ray photoelectron spectra XPS of paramagnetic cobalt (ii) compounds. *Chemical Physics Letters*, 42(2):264 – 267, 1976.

[128] Mariam Khachani, Mohamed Kacimi, Alain Ensuque, Jean-Yves Piquemal, Carole Connan, François Bozon-Verduraz, and Mahfoud Ziyad. Iron-calcium-hydroxyapatite catalysts: Iron speciation and comparative performances in butan-2-ol conversion and propane oxidative dehydrogenation. *Applied Catalysis A: General*, 388(1 - 2):113 – 123, 2010.

[129] Katsuyuki Matsunaga and Akihide Kuwabara. First-principles study of vacancy formation in hydroxyapatite. *Phys. Rev. B*, 75(1):014102, 2007.

[130] Bashar Issa, Ihab M. Obaidat, Borhan A. Albiss, and Yousef Haik. Magnetic nanoparticles: Surface effects and properties related to biomedicine applications. *International Journal of Molecular Sciences*, 14(11):21266, 2013.

[131] Y. Lee, J. Lee, C.-J. Bae, J.-G. Park, H.-J. Noh, J.-H. Park, and T. Hyeon. Large-scale synthesis of uniform and crystalline magnetite nanoparticles using reverse micelles as

nanoreactors under reflux conditions. *Advanced Functional Materials*, 15(3):503–509, 2005.

[132] Z.L. Liu, H.B. Wang, Q.H. Lu, G.H. Du, L. Peng, Y.Q. Du, S.M. Zhang, and K.L. Yao. Synthesis and characterization of ultrafine well-dispersed magnetic nanoparticles. *Journal of Magnetism and Magnetic Materials*, 283(2 - 3):258 – 262, 2004.

[133] Jinwoo Lee, Youjin Lee, Jong Kyu Youn, Hyon Bin Na, Taekyung Yu, Hwan Kim, Sang-Mok Lee, Yoon-Mo Koo, Ja Hun Kwak, Hyun Gyu Park, Ho Nam Chang, Misun Hwang, Je-Geun Park, Jungbae Kim, and Taeghwan Hyeon. Simple synthesis of functionalized superparamagnetic magnetite/silica core/shell nanoparticles and their application as magnetically separable high-performance biocatalysts. *Small*, 4(1):143–152, 2008.

[134] Mark J. Ernsting, Mami Murakami, Aniruddha Roy, and Shyh-Dar Li. Factors controlling the pharmacokinetics, biodistribution and intratumoral penetration of nanoparticles. *Journal of Controlled Release*, 172(3):782 – 794, 2013.

[135] Hsi-Chin Wu, Tzu-Wei Wang, Martha C. Bohn, Feng-Huei Lin, and Myron Spector. Novel magnetic hydroxyapatite nanoparticles as non-viral vectors for the glial cell line-derived neurotrophic factor gene. *Advanced Functional Materials*, 20(1):67–77, 2010.

[136] Jing Huang, Lihong Bu, Jin Xie, Kai Chen, Zhen Cheng, Xingguo Li, and Xiaoyuan Chen. Effects of nanoparticle size on cellular uptake and liver MRI with polyvinylpyrrolidone-coated iron oxide nanoparticles. *ACS Nano*, 4(12):7151–7160, 2010. PMID: 21043459.

[137] Do Kyung Kim, Maria Mikhaylova, Yu Zhang, and Mamoun Muhammed. Protective coating of superparamagnetic iron oxide nanoparticles. *Chemistry of Materials*, 15(8):1617–1627, 2003.

[138] Sudip Nath, Charalambos Kaittanis, Vasanth Ramachandran, Naresh S. Dalal, and J. Manuel Perez. Synthesis, magnetic characterization, and sensing applications of novel dextran-coated iron oxide nanorods. *Chemistry of Materials*, 21(8):1761–1767, 2009.

[139] K. A. Gross, R. Jackson, J. D. Cashion, and L. M. Rodrigues-Lorenzo. Iron substituted apatites: A resorbable biomaterial with potential magnetic properties. *European Cells and Materials*, 3:114–117, 2002.

[140] C. Capuccini, P. Torricelli, F. Sima, E. Boanini, C. Ristoscu, B. Bracci, G. Socol, M. Fini, I.N. Mihailescu, and A. Bigi. Strontium-substituted hydroxyapatite coatings synthesized by pulsed-laser deposition: In vitro osteoblast and osteoclast response. *Acta Biomaterialia*, 4(6):1885 – 1893, 2008.

[141] M. Wei, J. H. Evans, T. Bostrom, and L. Grøndahl. Synthesis and characterization of hydroxyapatite, fluoride-substituted hydroxyapatite and fluorapatite. *Journal of Materials Science: Materials in Medicine*, 14(4):311–320.

[142] W. B. Fortune and M. G. Mellon. Determination of iron with o-phenanthroline: A spectrophotometric study. *Industrial & Engineering Chemistry Analytical Edition*, 10(2):60–64, 1938.

[143] Cristina Castro Ribeiro, Iain Gibson, and Mário Adolfo Barbosa. The uptake of titanium ions by hydroxyapatite particles-structural changes and possible mechanisms. *Biomaterials*, 27(9):1749 – 1761, 2006.

[144] Yoshiaki Tanizawa, Kunio Sawamura, and Takashi Suzuki. Reaction characteristics of dental and synthetic apatites with Fe^{2+} and Fe^{3+} ions. *J. Chem. Soc., Faraday Trans.*, 86:1071–1075, 1990.

[145] Dinghua Yu, Cheng Wu, Yan Kong, Nianhua Xue, Xuefeng Guo, and Weiping Ding.

Structural and catalytic investigation of mesoporous iron phosphate. *The Journal of Physical Chemistry C*, 111(39):14394–14399, 2007.

[146] M.A. Salim, G.D. Khattak, P.S. Fodor, and L.E. Wenger. X-ray photoelectron spectroscopy (XPS) and magnetization studies of iron-vanadium phosphate glasses. *Journal of Non-Crystalline Solids*, 289(1 - 3):185 – 195, 2001.

[147] Xiaoyan Yu, Delbert E. Day, Gary J. Long, and Richard K. Brow. Properties and structure of sodium-iron phosphate glasses. *Journal of Non-Crystalline Solids*, 215(1):21 – 31, 1997.

[148] G.K. Marasinghe, M. Karabulut, C.S. Ray, D.E. Day, M.G. Shumsky, W.B. Yelon, C.H. Booth, P.G. Allen, and D.K. Shuh. Structural features of iron phosphate glasses. *Journal of Non-Crystalline Solids*, 222:144 – 152, 1997.

[149] Yanning Song, Peter Y. Zavalij, Masatsugu Suzuki, and M. Stanley Whittingham. New iron(iii) phosphate phases: Crystal structure and electrochemical and magnetic properties. *Inorganic Chemistry*, 41(22):5778–5786, 2002.

[150] Michael B. Korzenski, Joseph W. Kolis, and Gary J. Long. Hydrothermal synthesis, structural characterization, and physical properties of a new mixed valence iron phosphate, $SrFe_3(PO_4)_3$. *Journal of Solid State Chemistry*, 147(1):390 – 398, 1999.

[151] Arati G. Kolhatkar, Andrew C. Jamison, Dmitri Litvinov, Richard C. Willson, and T. Randall Lee. Tuning the magnetic properties of nanoparticles. *International Journal of Molecular Sciences*, 14(8):15977, 2013.

[152] D.U. Silverthorn. *Human Physiology: An Integrated Approach 5th ed*. Pearson Benjamin Cummings, San Francisco, 2010.

[153] Susmita Bose, Mangal Roy, and Amit Bandyopadhyay. Recent advances in bone tissue engineering scaffolds. *Trends in Biotechnology*, 30(10):546 – 554, 2012.

[154] R. Murugan and S. Ramakrishna. Bioresorbable composite bone paste using polysaccharide based nano hydroxyapatite. *Biomaterials*, 25(17):3829 – 3835, 2004.

[155] J. Chevalier and L. Gremillard. Ceramics for medical applications: A picture for the next 20 years. *Journal of the European Ceramic Society*, 29(7):1245 – 1255, 2009.

[156] Joseph R. Woodard, Amanda J. Hilldore, Sheeny K. Lan, C.J. Park, Abby W. Morgan, Jo Ann C. Eurell, Sherrie G. Clark, Matthew B. Wheeler, Russell D. Jamison, and Amy J. Wagoner Johnson. The mechanical properties and osteoconductivity of hydroxyapatite bone scaffolds with multi-scale porosity. *Biomaterials*, 28(1):45 – 54, 2007.

[157] Li-Hong He, Owen C. Standard, Tiffany T.Y. Huang, Bruno A. Latella, and Michael V. Swain. Mechanical behaviour of porous hydroxyapatite. *Acta Biomaterialia*, 4(3):577 – 586, 2008.

[158] A.J. Ruys, M. Wei, C.C. Sorrell, M.R. Dickson, A. Brandwood, and B.K. Milthorpe. Sintering effects on the strength of hydroxyapatite. *Biomaterials*, 16(5):409 – 415, 1995.

[159] Gurbinder Kaur, O.P. Pandey, K. Singh, Dan Homa, Brian Scott, and Gary Pickrell. A review of bioactive glasses: Their structure, properties, fabrication and apatite formation. *Journal of Biomedical Materials Research Part A*, 102(1):254–274, 2014.

[160] Nasser Y. Mostafa. Characterization, thermal stability and sintering of hydroxyapatite powders prepared by different routes. *Materials Chemistry and Physics*, 94(2 - 3):333 – 341, 2005.

[161] Linghong Guo, Mei Huang, and Xingdong Zhang. Effects of sintering temperature on structure of hydroxyapatite studied with rietveld method. *Journal of Materials Science: Materials in Medicine*, 14(9):817–822, 2003.

[162] Isaac Mayer, Orit Jacobsohn, Tamara Niazov, Jacques Werckmann, Monica Iliescu, Mireille Richard-Plouet, Olaf Burghaus, and Dirk Reinen. Manganese in precipitated hydroxyapatites. *European Journal of Inorganic Chemistry*, 2003(7):1445–1451, 2003.

[163] M. Aminzare, A. Eskandari, M.H. Baroonian, A. Berenov, Z. Razavi Hesabi, M. Taheri, and S.K. Sadrnezhaad. Hydroxyapatite nanocomposites: Synthesis, sintering and mechanical properties. *Ceramics International*, 39(3):2197 – 2206, 2013.

[164] Y. Oshida. *Hydroxyapatite Synthesis and Applications*. Momentum Press, New York, 2015.

[165] Solaiman Tarafder, Vamsi Krishna Balla, Neal M Davies, Amit Bandyopadhyay, and Susmita Bose. Microwave-sintered 3d printed tricalcium phosphate scaffolds for bone tissue engineering. *Journal of Tissue Engineering and Regenerative Medicine*, 7(8):631–641, 2013.

[166] Th. Leventouri. Synthetic and biological hydroxyapatites: Crystal structure questions. *Biomaterials*, 27(18):3339 – 3342, 2006.

[167] E. S. Place, N. D. Evans, and M. M. Stevens. Complexity in biomaterials for tissue engineering. *Nature Materials*, 8:457–470, 2009.

[168] Fardad T. Afshari, Jessica C. Kwok, Melissa R. Andrews, Bas Blits, Keith R. Martin, Andreas Faissner, Charles Ffrench-Constant, and James W. Fawcett. Integrin activation or $\alpha 9$ expression allows retinal pigmented epithelial cell adhesion on bruch's membrane in wet age-related macular degeneration. *Brain*, 133(2):448–464, 2010.

[169] Michel Rabinovitch and Mary Jo de Stefano. Manganese stimulates adhesion and spreading of mouse sarcoma I ascites cells. *The Journal of Cell Biology*, 59(1):165–176, 1973.

[170] Zhenxiang Zhang, Beibei Gu, Wei Zhu, and Lixian Zhu. Integrin-mediated osteoblastic adhesion on a porous manganese-incorporated TiO_2 coating prepared by plasma electrolytic oxidation. *Experimental and Therapeutic Medicine*, 6:707–714, 2013.

[171] Wataru Fujitani, Yoshinosuke Hamada, Naomasa Kawaguchi, Seiji Mori, Kiyoshi Daito, Ayako Uchinaka, Takuya Matsumoto, Yoshihisa Kojima, Michiharu Daito, Takayoshi Nakano, and Nariaki Matsuura. Synthesis of hydroxyapatite contining manganese and its evaluation of biocompatibility. *Nano Biomedicine*, 2(1):37–46, 2010.

[172] A. Bigi, B. Bracci, F. Cuisinier, R. Elkaim, M. Fini, I. Mayer, I.N. Mihailescu, G. Socol, L. Sturba, and P. Torricelli. Human osteoblast response to pulsed laser deposited calcium phosphate coatings. *Biomaterials*, 26(15):2381 – 2389, 2005.

[173] Keith M. Erikson, Tore Syversen, Judy L. Aschner, and Michael Aschner. Interactions between excessive manganese exposures and dietary iron-deficiency in neurodegeneration. *Environmental Toxicology and Pharmacology*, 19(3):415 – 421, 2005.

[174] Deborah L. Baly, Carl L. Keen, and Lucille S. Hurley. Effects of manganese deficiency on pyruvate carboxylase and phosphoenolpyruvate carboxykinase activity and carbohydrate homeostasis in adult rats. *Biological Trace Element Research*, 11(1):201–212, 1986.

[175] Annika Armulik, Gunbjørg Svineng, Krister Wennerberg, Reinhard Fässler, and Staffan Johansson. Expression of integrin subunit β1B in integrin β1-deficient GD25 cells does not interfere with aVβ3 functions. *Experimental Cell Research*, 254(1):55 – 63, 2000.

[176] G Muralithran and S Ramesh. The effects of sintering temperature on the properties of hydroxyapatite. *Ceramics International*, 26(2):221 – 230, 2000.

[177] D. C. Golden and D. W. Ming. Nutrient substituted hydroxyapatites: synthesis and characterization. *Soil Science Society of America Journal*, 63:657–664, 1999.

[178] B. Sutter, T. Wasowicz, T. Howard, L. R. Hossner, and D. W. Ming. Characterization of iron, manganese, and copper synthetic hydroxyapatites by electron paramagnetic resonance spectroscopy. *Soil Science Society of America Journal*, 66:1359–1366, 2002.

[179] B. Sutter, L. R. Hossner, and D. W. Ming. Dissolution kinetics of iron-, manganese-, and copper-containing synthetic hydroxyapatites. *Soil Science Society of America Journal*, 69:362–370, 2005.

[180] B. Sutter, D. W. Ming, A. Clearfield, and L. R. Hossner. Mineralogical and chemical characterization of iron-, manganese-, and copper-containing synthetic hydroxyapatites. *Soil Science Society of America Journal*, 67:1935–1942, 2003.

[181] B. Sutter, R. E. Taylor, L. R. Hossner, and D. W. Ming. Solid state 31 phosphorous nuclear magnetic resonance of iron-, manganese-, and copper-containing synthetic hydroxyapatites. *Soil Science Society of America Journal*, 66:455–463, 2002.

[182] Isaac Mayer, Frederic J. G. Cuisinier, Ina Popov, Yechezkel Schleich, Sarit Gdalya, Olaf Burghaus, and Dirk Reinen. Phase relations between β-tricalcium phosphate and hydroxyapatite with manganese(ii): Structural and spectroscopic properties. *European Journal of Inorganic Chemistry*, 2006(7):1460–1465, 2006.

[183] Czeslawa Paluszkiewicz, Anna Slósarczyk, Dawid Pijocha, Maciej Sitarz, Miroslaw Bucko, Aneta Zima, Anna Chróscicka, and Malgorzata Lewandowska-Szumiel. Synthesis, structural properties and thermal stability of Mn-doped hydroxyapatite. *Journal of Molecular Structure*, 976(1Ű3):301 – 309, 2010.

[184] Yan Li, Chai Teck Nam, and Chui Ping Ooi. Iron(iii) and manganese(ii) substituted hydroxyapatite nanoparticles: Characterization and cytotoxicity analysis. *Journal of Physics: Conference Series*, 187(1):012024, 2009.

[185] Yan Li, Jasmine Widodo, Sierin Lim, and Chui Ping Ooi. Synthesis and cytocompatibility of manganese (ii) and iron (iii) substituted hydroxyapatite nanoparticles. *Journal of Materials Science*, 47(2):754–763, 2012.

[186] B. Bracci, P. Torricelli, S. Panzavolta, E. Boanini, R. Giardino, and A. Bigi. Effect of Mg^{2+}, Sr^{2+}, and Mn^{2+} on the chemico-physical and in vitro biological properties of calcium phosphate biomimetic coatings. *Journal of Inorganic Biochemistry*, 103(12):1666 – 1674, 2009.

[187] I. Mayer, F. J. G. Cuisinier, S. Gdalya, and I. Popov. TEM study of the morphology of Mn^{2+}-doped calcium hydroxyapatite and β-tricalcium phosphate. *Journal of Inorganic Biochemistry*, 102(2):311 – 317, 2008.

[188] S. Ramesh, C.Y. Tan, C.L. Peralta, and W.D. Teng. The effect of manganese oxide on the sinterability of hydroxyapatite. *Science and Technology of Advanced Materials*, 8(4):257 – 263, 2007.

[189] ASTM F 394. Test method for biaxial flexure strength (modulus of rupture) of ceramic substrates. Technical report, ASTM, 1996.

[190] S. M. Barinov, J. V. Rau, S. Nunziante Cesaro, J. Ďurišin, I. V. Fadeeva, D. Ferro, L. Medvecky, and G. Trionfetti. Carbonate release from carbonated hydroxyapatite in the wide temperature rage. *Journal of Materials Science: Materials in Medicine*, 17(7):597–604, 2006.

[191] B. Gillot, M. El Guendouzi, and M. Laarj. Particle size effects on the oxidation-reduction behavior of Mn_3O_4 hausmannite. *Materials Chemistry and Physics*, 70(1):54 – 60, 2001.

[192] R.G. Carrodeguas and S. De Aza. α-tricalcium phosphate: Synthesis, properties and biomedical applications. *Acta Biomaterialia*, 7(10):3536 – 3546, 2011.

[193] J. Wang and L. Shaw. Morphology-enhanced low-temperature sintering of nanocrystalline hydroxyapatite. *Advanced Materials*, 19(17):2364–2369, 2007.

[194] Deepak K. Pattanayak, Rajalaxmi Dash, R.C. Prasad, B.T. Rao, and T.R. Rama Mohan. Synthesis and sintered properties evaluation of calcium phosphate ceramics. *Materials Science and Engineering: C*, 27(4):684 – 690, 2007.

[195] M. Akao, H. Aoki, and K. Kato. Mechanical properties of sintered hydroxyapatite for prosthetic applications. *Journal of Materials Science*, 16(3):809–812, 1981.

[196] Sumit Pramanik, Avinash Kumar Agarwal, K.N. Rai, and Ashish Garg. Development of high strength hydroxyapatite by solid-state-sintering process. *Ceramics International*, 33(3):419 – 426, 2007.

[197] S. Sureshbabu, Manoj Komath, and H. K. Varma. In situ formation of hydroxyapatite - alpha tricalcium phosphate biphasic ceramics with higher strength and bioactivity. *Journal of the American Ceramic Society*, 95(3):915–924, 2012.

[198] S. Kannan, S.I. Vieira, S.M. Olhero, P.M.C. Torres, S. Pina, O.A.B. da Cruz e Silva, and J.M.F. Ferreira. Synthesis, mechanical and biological characterization of ionic doped carbonated hydroxyapatite/beta-tricalcium phosphate mixtures. *Acta Biomaterialia*, 7(4):1835 – 1843, 2011.

[199] H.S. Liu, T.S. Chin, L.S. Lai, S.Y. Chiu, K.H. Chung, C.S. Chang, and M.T. Lui. Hydroxyapatite synthesized by a simplified hydrothermal method. *Ceramics International*, 23(1):19 – 25, 1997.

[200] Laurent Boilet, Michel Descamps, Emmanuelle Rguiti, Arnaud Tricoteaux, Jianxi Lu, Fabrice Petit, Véronique Lardot, Francis Cambier, and Anne Leriche. Processing and properties of transparent hydroxyapatite and β tricalcium phosphate obtained by HIP process. *Ceramics International*, 39(1):283 – 288, 2013.

[201] S. Raynaud, E. Champion, J.P. Lafon, and D. Bernache-Assollant. Calcium phosphate apatites with variable Ca/P atomic ratio III. mechanical properties and degradation in solution of hot pressed ceramics. *Biomaterials*, 23(4):1081 – 1089, 2002.

[202] Y. H. An and R. A. Draugh. *Mechanical Testing of Bone and the Bone-Implant Interface*. CRC Press, Boca Raton, 2000.

[203] Jiwen Wang and Leon L. Shaw. Nanocrystalline hydroxyapatite with simultaneous enhancements in hardness and toughness. *Biomaterials*, 30(34):6565 – 6572, 2009.

[204] E. Kramer, M. Zilm, and M. Wei. A comparative study of the sintering behavior of pure and iron-substituted hydroxyapatite. *Bioceramics Development and Applications*, 3:067, 2013.

[205] Katsumi Yoshida, Naoki Kondo, Hideki Kita, Masanori Mitamura, Kazuaki Hashimoto, and Yoshitomo Toda. Effect of substitutional monovalent and divalent metal ions on mechanical properties of β-tricalcium phosphate. *Journal of the American Ceramic Society*, 88(8):2315–2318, 2005.

[206] Yasuhiro Tanimoto and Norihiro Nishiyama. Preparation and physical properties of tricalcium phosphate laminates for bone-tissue engineering. *Journal of Biomedical Materials Research Part A*, 85A(2):427–433, 2008.

[207] Y.J. Seol, J.Y. Park, J.W. Jung, J. Jang, R. Girdhari, S.W. Kim, and D.W. Cho. Improvement of bone regeneration capability of ceramic scaffolds by accelerated release of their calcium ions. *Tissue Engineering: Part A*, 20:2840–2849, 2014.

[208] Cesar G. Fraga. Relevance, essentiality and toxicity of trace elements in human health. *Molecular Aspects of Medicine*, 26(4 - 5):235 – 244, 2005.

[209] Syed F Ali, Helen M Duhart, Glenn D Newport, George W Lipe, and William Slikker

Jr. Manganese-induced reactive oxygen species: Comparison between Mn^{+2} and Mn^{+3}. *Neurodegeneration*, 4(3):329 – 334, 1995.

[210] Elena Papis, Federica Rossi, Mario Raspanti, Isabella Dalle-Donne, Graziano Colombo, Aldo Milzani, Giovanni Bernardini, and Rosalba Gornati. Engineered cobalt oxide nanoparticles readily enter cells. *Toxicology Letters*, 189(3):253 – 259, 2009.

[211] M. Motskin, D.M. Wright, K. Muller, N. Kyle, T.G. Gard, A.E. Porter, and J.N. Skepper. Hydroxyapatite nano and microparticles: Correlation of particle properties with cytotoxicity and biostability. *Biomaterials*, 30(19):3307 – 3317, 2009.

[212] X. Yu and M. Wei. Cellular performance comparison of biomimetic calcium phosphate coating and alkaline-treated titanium surface. *Biomed Res. Int.*, 2013:1–9, 2013.

[213] Yuan Yuan, Changsheng Liu, Jiangchao Qian, Jing Wang, and Yuan Zhang. Size-mediated cytotoxicity and apoptosis of hydroxyapatite nanoparticles in human hepatoma HepG2 cells. *Biomaterials*, 31(4):730 – 740, 2010.

[214] S.M. Zakaria, S.H.S. Zein, M.R. Othman, F. Yang, and J.A. Jansen. Nanophase hydroxyapatite as a biomaterial in advanced hard tissue engineering: a review. *Tissue Eng. Pt. B-Rev*, 19:431–441, 2013.

[215] Chengtie Wu, Yinghong Zhou, Wei Fan, Pingping Han, Jiang Chang, Jones Yuen, Meili Zhang, and Yin Xiao. Hypoxia-mimicking mesoporous bioactive glass scaffolds with controllable cobalt ion release for bone tissue engineering. *Biomaterials*, 33(7):2076 – 2085, 2012.

[216] Xianglu Han, Robert Gelein, Nancy Corson, Pamela Wade-Mercer, Jingkun Jiang, Pratim Biswas, Jacob N. Finkelstein, Alison Elder, and Günter Oberdörster. Validation of an LDH assay for assessing nanoparticle toxicity. *Toxicology*, 287(1 - 3):99 – 104, 2011.

[217] Amara L. Holder, Regine Goth-Goldstein, Donald Lucas, and Catherine P. Koshland. Particle-induced artifacts in the MTT and LDH viability assays. *Chemical Research in Toxicology*, 25(9):1885–1892, 2012.

[218] Changmin Hu, Lichun Zhang, and Mei Wei. Development of biomimetic scaffolds with both intrafibrillar and extrafibrillar mineralization. *ACS Biomaterials Science & Engineering*, 1(8):669–676, 2015.

[219] Li-na Niu, Kai Jiao, Yi-pin Qi, Cynthia K. Y. Yiu, Heonjune Ryou, Dwayne D. Arola, Ji-hua Chen, Lorenzo Breschi, David H. Pashley, and Franklin R. Tay. Infiltration of silica inside fibrillar collagen. *Angewandte Chemie International Edition*, 50(49):11688–11691, 2011.

[220] Li-na Niu, Kai Jiao, Heonjune Ryou, Cynthia K. Y. Yiu, Ji-hua Chen, Lorenzo Breschi, Dwayne D. Arola, David H. Pashley, and Franklin R. Tay. Multiphase intrafibrillar mineralization of collagen. *Angewandte Chemie International Edition*, 52(22):5762–5766, 2013.

[221] Stephen Mann, Douglas D. Archibald, Jon M. Didymus, Trevor Douglas, Brigid R. Heywood, Fiona C. Meldrum, and Nicholas J. Reeves. Crystallization at inorganic-organic interfaces: Biominerals and biomimetic synthesis. *Science*, 261:1286–1292, 1993.

[222] Jeff W. M. Bulte, Trevor Douglas, Stephen Mann, Richard B. Frankel, Bruce M. Moskowitz, Rodney A. Brooks, Charles D. Baumgarner, Josef Vymazal, Marie-Paule Strub, and Joseph A. Frank. Magnetoferritin: Characterization of a novel superparamagnetic MR contrast agent. *Journal of Magnetic Resonance Imaging*, 4(3):497–505, 1994.

[223] Fiona C. Meldrum, Trevor Douglas, Sonia Levi, Paolo Arosio, and Stephen Mann.

Reconstitution of manganese oxide cores in horse spleen and recombinant ferritins. *Journal of Inorganic Biochemistry*, 58(1):59 – 68, 1995.

[224] N. Rajan, J. Habermehl, M. F. Cote, C. J. Doillon, and D. Mantovani. Preparation of ready-to-use storable and reconstituted type I collagen from rat tail tendon for tissue engineering applications. *Nature Protocols*, 1:2753–2758, 2006.

[225] Archan Dey, Jos J. M. Lenders, and Nico A. J. M. Sommerdijk. Bioinspired magnetite formation from a disordered ferrihydrite-derived precursor. *Faraday Discuss.*, 179:215–225, 2015.

[226] Jos J. M. Lenders, Harshal R. Zope, Ayana Yamagishi, Paul H. H. Bomans, Atsushi Arakaki, Alexander Kros, Gijsbertus de With, and Nico A. J. M. Sommerdijk. Bioinspired magnetite crystallization directed by random copolypeptides. *Advanced Functional Materials*, 25(5):711–719, 2015.

[227] Erica Kramer, Matthew Conklin, Michael Zilm, Emily Itzowitz, and Mei Wei. A comparative study of the sintering and cell behavior of pure and cobalt substituted hydroxyapatite. *Bioceramics Development and Applications*, 4:077, 2014.